



Synthetic Aperture Radar : Algorithms and Applications in Forests and Urban Areas

Ibrahim El Moussawi

► To cite this version:

Ibrahim El Moussawi. Synthetic Aperture Radar : Algorithms and Applications in Forests and Urban Areas. Earth Sciences. Université Montpellier; Lebanese international university, 2019. English. NNT : 2019MONTG078 . tel-02579180

HAL Id: tel-02579180

<https://theses.hal.science/tel-02579180>

Submitted on 14 May 2020

HAL is a multi-disciplinary open access archive for the deposit and dissemination of scientific research documents, whether they are published or not. The documents may come from teaching and research institutions in France or abroad, or from public or private research centers.

L'archive ouverte pluridisciplinaire **HAL**, est destinée au dépôt et à la diffusion de documents scientifiques de niveau recherche, publiés ou non, émanant des établissements d'enseignement et de recherche français ou étrangers, des laboratoires publics ou privés.

THÈSE POUR OBTENIR LE GRADE DE DOCTEUR DE L'UNIVERSITÉ DE MONTPELLIER

En GEOMATIQUE

École doctorale GAIA

Unité de recherche TETIS

En partenariat international avec Université Libanaise, Liban

Titre de la thèse

Synthetic Aperture Radar: Algorithms and Applications in Forests and Urban Areas

Présentée par Ibrahim El Moussawi

Le 12 Décembre 2019

Sous la direction de Nicolas Baghdadi
Et Jalal Jomaah

Devant le jury composé de

M. Elias RACHID, Professeur, USJ

M. Daniel RAUCOULES, Docteur, BRGM DRP/IGT Orléans

M. Husam AYAD, maître de conférences, Université Libanaise

Mme. Thuy LE TOAN, Ingénieur de Recherche, CESBIO

M. Nicolas BAGHDADI, Directeur de Recherche, TETIS, IRSTEA

M. Jalal JOMAAH, Professeur, Université Libanaise

M. Dinh HO TONG MINH, Chargé de Recherche (HDR), TETIS, IRSTEA

M. Chadi ABDALLAH, Directeur de Recherche, CNRS-L

M. Ghaleb FAOUR, Directeur de Recherche, CNRS-L

M. Olivier STRAUSS, maître de conférences, LIRMM, Université de Montpellier

Président, Rapporteur

Rapporteur

Examineur

Examineur

Directeur de Thèse

Directeur de Thèse

Co-encadrant de Thèse

Co-encadrant de Thèse

Invité

Invité



UNIVERSITÉ
DE MONTPELLIER



Contents

Contents	i
List of Figures	1
List of Tables	7
Publications	9
Abstract	11
Résumé	13
Acknowledgements	17
Résumé Francais	19
Contexte général	19
Missions ROS	21
Questions de recherche et objectifs de la Thèse	23
Contributions à la these	24
Résumé de la thèse	25

Conclusion générale	27
I Introduction and Synthetic Aperture Radar algorithms and applications	31
1 Introduction	33
1.1 General context	33
1.2 SAR missions	35
1.3 Research problem and Objectives	37
1.4 Thesis contributions	38
1.5 Thesis outline	39
2 Synthetic Aperture Radar algorithms and applications	41
2.1 Synthetic Aperture Radar basics	41
2.1.1 Single look complex data	43
2.1.2 SAR resolution	43
2.1.3 Speckle in SAR images	43
2.1.4 SAR data characteristics	44
2.1.5 Sentinel-1 data	44
2.1.6 Airborne data	45
2.1.7 SAR applications	47
2.2 Interferometry SAR	48
2.3 Permanent scatterer interferometry	49
2.4 Tomography SAR background	50
2.5 phase calibration	52
2.5.1 Phase Calibration algorithms	53
2.5.2 Phase Calibration by Permanent Scatterer Interferometry (PS-InSAR)	53
2.5.3 Phase Calibration by Algebraic Synthesis (AS)	55
2.5.4 Phase Calibration by Distributed Targets (DS-InSAR)	57

II	Tomography SAR for forested areas	59
3	L-band UAVSAR tomographic imaging in dense forests, Gabon forests	61
3.1	Introduction	61
3.2	Materials and Methods	64
3.2.1	Study area	64
3.2.2	Data-sets	65
3.2.3	TomoSAR background	68
3.2.4	TomoSAR Phase Calibration	69
3.2.5	TomoSAR inversion	71
3.2.6	Estimate forests top height	72
3.3	Results	75
3.4	Discussion	78
3.5	Conclusion	82
4	Monitoring tropical forest structure using SAR tomography at L and P-band	85
4.1	Introduction	85
4.2	Materials and Methods	88
4.2.1	Study Area	88
4.2.2	Data-Set	89
4.2.3	Tomography SAR	93
4.2.4	Tomography Inversion	94
4.2.5	TomoSAR Phase Calibration	94
4.2.6	Forest structure indices	95
4.2.7	Forest Structure Parameters	97
4.3	Results	99
4.3.1	Limitation of L-Band TomoSAR in Tropical Forest (TropiSAR Data)	99
4.3.2	TomoSAR Profiles at L- and P-Band (AfriSAR Data)	99
4.3.3	TomoSAR Multi-Layers	103
4.3.4	Forest Top Height Estimation from L- and P-Band	104
4.4	Discussion	105

4.4.1	Limitation of L-Band TomoSAR in Tropical Forest (TropiSAR Data)	107
4.4.2	TomoSAR Profiles at L- and P-Band (AfriSAR Data)	107
4.4.3	TomoSAR Multi-Layers	108
4.4.4	Forest Top Height Estimation from L- and P-Band	108
4.4.5	Forest Structure Indices and Parameters	109
4.5	Conclusions	110
III Land-subsidence monitoring using PS/DSInSAR technique		113
5	Comparison of multi temporal radar interferometry techniques using Sentinel-1: Lebanon case study	115
5.1	Introduction	115
5.2	Materials and Methods	118
5.2.1	Interferometry	118
5.2.2	PSI	121
5.2.3	PS/DS	123
5.2.4	Detail processing from step 6 stamps	125
5.3	Results	127
5.3.1	Lebanon site	127
5.3.2	PS results	130
5.3.3	PS/DS results	130
5.4	Discussion	132
5.4.1	Sentinel-1	132
5.4.2	Deformation velocity	133
5.4.3	Phase calibration via phase center double localization	133
5.5	Conclusion	134
General Conclusion		139
	TomoSAR perspectives	140
	InSAR perspectives	141

Bibliography	143
Appendices	167
A L-band UAVSAR tomographic imaging in dense forests: Gabon forests	167
B Monitoring tropical forest structure using SAR tomography at L- and P-band	169
C Comparison of multi temporal radar interferometry techniques using Sentinel-1: Lebanon case study	171
D Estimation of Rice Height and Biomass Using Multitemporal SAR Sentinel-1 for Camargue, Southern France.	173
E Measuring Ground Subsidence in Ha Noi Through the Radar Interferometry Technique Using TerraSAR-X and Cosmos SkyMed Data	175



List of Figures

2.1	SAR imaging.	42
2.2	Phase calibration of MB SAR data using PS-InSAR approach	53
2.3	Phase calibration of MB SAR data using AS approach	55
2.4	Phase calibration of MB SAR data using DS approach	58
3.1	Study area, Gabon Lopé Park. The black polygon represents where UAVSAR acquired L-band TomoSAR data. The background is derived from the Africa Copernicus Land Cover of 100 m x 100 m spatial resolution [Tsendbazar et al., 2018]. The land cover shows different vegetation features of the Lopé National Park.	64
3.2	Left, Schematic representation of the TomoSAR acquisition. Azimuth axis is orthogonal to the picture. Right, schematic view of TomoSAR imaging, where each layer represent scattering contributions associated with certain height.	69
3.3	The schematic view of the vertical backscatter distribution (TomoSAR Capon profile at certain cell).	73

3.4	(a) Schematic view of Lidar LVIS waveform divided into four zones. Zone 1: ground contribution, zone 2: Canopy contribution, zone3 : Noise and unwanted reflected signal. (b) Extraction of Lidar level 2 data from LVIS waveform. RH100 is the elevation of the highest detected return (forest top height). RH25 is the elevation where 25% of the waveform energy is occurs, it denotes the ground layer associated with LVIS data.	74
3.5	(a,b) The 2-D intensity of the TomoSAR image; the red lines correspond to the slant range positions where the cut was chosen. (c,d) The Lidar cut at two slant range positions 200 and 590, respectively. (e,f) HH Capon spectra. The black and white lines in (e,f) correspond to the digital terrain model (DTM) and canopy height model (CHM) from small-footprint Lidar (SFL), respectively. Capon power was normalized between 0 and 1 to enhance visualization of the scatterers.	76
3.6	Regions of interest (ROIs) named (a) COL1, (b) OKO1, and (c) OKO2 in the Gabon Lopé Park. HH(in red), HV(in green) Capon profiles. Capon power and LVIS waveform power are normalized between 0 and 1. The histograms of SFL canopy and ground elevations are presented respectively in blue and in brown. The blue curve corresponding to LVIS waveform Level 1B.	77
3.7	(a) original SAR image. HH power intensities associated with SAR image with three layers produced by TomoSAR, (b) 0 m, (c) 15 m, (d) 30 m.	77
3.8	Lidar LVIS Level2 different layers (a) RH25, (b) RH50 and (c) RH75 corresponds to the Lidar LVIS layers. RH25% represents the elevation where 25% of waveform energy occurs(ground layer). RH50% represents the elevation where 50% of waveform energy occurs, and RH75% represents the elevation where 75% of waveform energy occurs.	78
3.9	(a) forests top height RMSE and (b) bias versus penetration loss with respect to Noise floor elevation.	78
3.10	(a): Tree top height from L-band TomoSAR. (b): CHM from SFL data. (c): Relative difference between Lidar and TomoSAR tree top height, height difference = $(H_{\text{Tomo}} - H_{\text{Lidar}})$	79

3.11	Histogram of the height difference (L_band - SFL Lidar data).	80
4.1	TropiSAR, BioSAR , and AfriSAR Campaigns. Study area main site (Gabon Lopé National park). The red polygon denotes the footprint of L-band UAVSAR platform. The Digital elevation model of the Lopé is displayed.	90
4.2	TomoSAR acquisition.	93
4.3	Phase calibration problem formulation.	95
4.4	Horizontal/vertical structure plane proposed for forest structure classification. .	96
4.5	Definition of top layer for the horizontal structure index and the threshold to remove peaks introduced by the ground scattering contributions.	98
4.6	(a) L-band Tomogram (HH channel) at Tropical Paracou forest; (b) P-band Tomogram (HH channel) at Tropical Paracou forest; (c) L-band Tomogram (HH channel) at Boreal Krycklan forest; (d) P-band Tomogram (HH channel) at Boreal Krycklan forest. The algorithm used to get the tomography profiles is the Capon beamforming power estimator.	100
4.7	(a) 2D intensity of SLC P-band image. The red line denotes the cut where the Capon beamforming estimator was applied; (b) P-band Tomogram (HH channel) before applying phase screen correction; (c) P-band Tomogram (HH channel) after applying phase screen correction.	101
4.8	(a) and (f) SFL CHM LiDAR cuts at slant range equal to 300 m and 650 m; (b) and (g) 2D intensity L-band SLC image. The red line denotes the cut where we had chosen to estimate the vertical structure along with slant range; (c) and (h) L-band HH channel Tomographic profile at the two cuts (300 m and 650 m); (d) and (i) P-band HH channel Tomographic profile at the two cuts (300 m and 650 m); (e) and (j) LVIS data layers from LiDAR LVIS Canopy Height Model (CHM), which is obtained from a Small Footprint LiDAR (SFL) it is defined before as land vegetation and ice sensor Level 1B at the two cut, defined before (300 m and 650 m). The white line in all tomograms denote the RH75 height from LiDAR LVIS Level2 data.	102

4.9	(a) canopy peak height estimated from LiDAR waveform (RH75); (b) canopy peak height estimated from L-band data; (c) canopy peak height estimated from P-band data.	103
4.10	(a) histogram of the difference between canopy peak height estimated from P-band data and canopy peak height estimated from L-band data; (b) histogram of the difference between canopy peak height estimated from L-band data and canopy peak height estimated from LiDAR LVIS Level1B data (or RH75 from LiDAR LVIS Level2 data); (c) histogram of the difference between canopy peak height estimated from P-band data and canopy peak height estimated from LiDAR LVIS Level1B data.	103
4.11	(a) region of interest (ROI) named OKO2 in Gabon Lopé Park. P-band HH (in red) and L-band HH (in green) Capon profiles. Capon power and LVIS waveform power were normalized between 0 and 1. The histograms of SFL canopy and ground elevations are presented respectively in blue and brown. The blue curve corresponds to LVIS waveform Level 1B; (b) P-band Capon HV profile in red. L-band Capon HV profile in green.	104
4.12	(a) original SAR image. HH power intensities associated with an L-band SAR with three layers produced by TomoSAR: 0 m, 15 m, 30 m; (b) original SAR image. HH power intensities associated with a P-band SAR with three layers produced by TomoSAR: 0 m, 15 m, 30 m; (c) power intensities associated with LVIS data layers produced from LiDAR LVIS Level 1B data: 0 m, 15 m, 30 m.	105
4.13	(a) CHM from SFL data; (b) forest top height estimated from L-band TomoSAR data; (c) relative difference between LiDAR and L-band TomoSAR tree top height, height difference = $(HTomo - HLiDAR)/HLiDAR$; (d) histogram of the difference between the estimated height from L-band and CHM from SFL data; (e) forest top height estimated from P-band TomoSAR data; (f) relative difference between LiDAR and P-band TomoSAR tree top height, height difference = $(HTomo - HLiDAR)/HLiDAR$; (g) histogram of the difference between the estimated height from P-band and CHM from SFL data.	106
5.1	InSAR basics.	119

5.2	PS processing chain.	122
5.3	PS/DS processing chain	124
5.4	Study area. The red polygon related to the area where Sentinel-1 data stack was processed.	128
5.5	Interferograms generated by PS/DS processing chain at different dates.	131
5.6	Gacos model for atmospheric phase at different dates.	132
5.7	(a) Deformation velocity map using PS/DS processing chain. (b) Deformation velocity map using PS processing chain. (c) Difference velocity histogram between PS velocity and PS/DS velocity.	135



List of Tables

2.1	Sentinel-1 data configuration.	44
2.2	L-band UAVSAR acquisition parameters.	46
2.3	Description of the SETHI system configuration of P-band acquisition parameters. The superscript * indicates the parameters that are identical between the SETHI and F-SAR systems.	46
3.1	Region of interests at Lopé Park.	65
3.2	L-band UAVSAR acquisition parameters.	67
3.3	Baseline configuration of Multi-baseline UAVSAR acquisitions.	67
4.1	L-band UAVSAR acquisition parameters.	92
4.2	Description of the SETHI system configuration of P-band acquisition parameters. The superscript * indicates the parameters that are identical between the SETHI and F-SAR systems.	92
5.1	PS results statistics.	136
5.2	DS results statistics.	137
5.3	Geological classes.	138



Publications

International Journals

[1] **El Moussawi, I.**; Ho Tong Minh, D.; Baghdadi, N.; Abdallah, C.; Jomaah, J.; Strauss, O.; Lavalley, M.; Ngo, Y.-N. Monitoring Tropical Forest Structure Using SAR Tomography at L- and P-Band. Remote Sens. 2019, 11, 1934

[2] Minh, Dinh Ho Tong, Quoc Cuong Tran, Quy Nhan Pham, Tran Trung Dang, Duc Anh Nguyen, **Ibrahim El-Moussawi**, and Thuy Le Toan. "Measuring Ground Subsidence in Ha Noi Through the Radar Interferometry Technique Using TerraSAR-X and Cosmos SkyMed Data."

[3] **El Moussawi, I.**; Ho Tong Minh, D.; Baghdadi, N.; Abdallah, C.; Jomaah, J.; Strauss, O.; Lavalley, M. L-Band UAVSAR Tomographic Imaging in Dense Forests: Gabon Forests. Remote Sens. 2019, 11, 475.

[4] Ndikumana, E., Ho Tong Minh, D., Dang Nguyen, H., Baghdadi, N., Courault, D., Hossard, L., and **El Moussawi, I.** (2018). Estimation of rice height and biomass using multitemporal SAR Sentinel-1 for Camargue, Southern France. Remote Sensing, 10(9), 1394.

[5] **Draft: El Moussawi, I.**; Ho Tong Minh, D.; Baghdadi, N.; Abdallah, C.; Jomaah,

J.; Strauss, O.; Laval, M., Y-N.N Comparison multi temporal radar interferometry techniques using Sentinel-1 : Lebanon case study

International Conferences

[1] **El Moussawi, I.**, MINH, Dinh Ho Tong, BAGHDADI, Nicolas, et al. L-Band Uavsar Tomographic Imaging in Dense Forest: Afrisar Results. In : IGARSS 2018-2018 IEEE International Geoscience and Remote Sensing Symposium. IEEE, 2018. p. 6723-6726.

[2] **El Moussawi, I.**, MINH, Dinh Ho Tong, BAGHDADI, Nicolas, et al. L-Band and P-band Tomographic Imaging in Dense Forest: Afrisar Results. In : PolINSAR 2019, ESA, 2019, Rome, Frascati, Italy.

[3] NGO, Y.-N., MINH, D. Ho Tong, **El Moussawi, I.**, et al. Afrisar-Tropisar: Forest Biomass Retrieval by P-Band Sar Tomography. In : IGARSS 2018-2018 IEEE International Geoscience and Remote Sensing Symposium. IEEE, 2018. p. 8675-8678.

[4] Minh, D. H. T., Ndikumana, E., Thu, D. N. H., Baghdadi, N., Courault, D., Hossard, L., and **El Moussawi, I.** (2018, October). Rice height and biomass estimations using multi temporal SAR Sentinel 1: Camargue case study. In Remote Sensing for Agriculture, Ecosystems, and Hydrology XX (Vol. 10783, p. 107830U). International Society for Optics and Photonics.



Abstract

The objective of this thesis is to exploit Multi-baseline Synthetic Aperture Radar (SAR) for studying the remote sensing of natural scenarios, such as forest structure characterization and land subsidence monitoring. In the case of forested areas, tropical forest structure parameters are derived by Tomography SAR (TomoSAR) technique. For urban areas, Land subsidence is investigated through Interferometry SAR (InSAR) techniques. TomoSAR and InSAR will be treated by using Multi-baseline SAR images over different sites. Prior to tomographic analysis, a phase calibration algorithm is needed to compensate for phase residuals that corrupt the data and influence the focusing of Multi-baseline data. First, a tomographic study has carried out in tropical forest, where the forest characterization was assessed by using SAR tomography at L and P-band. Second, different InSAR techniques have been compared with respect to their performance in monitoring earth's surface deformation, taking Lebanon as a case study.

The first part of the thesis presents the TomoSAR analysis in the tropical forest. A review of phase calibration techniques employed on TomoSAR data is shown. The problem formulation starts with the phase calibration of the data stack that is considered as the main gate to begin with SAR processing algorithms. Thus, the main phase calibration algorithms proposed in the literature are discussed. Two of the most important phase cal-

ibration approaches are then described and discussed in detail. The potential of L-band TomoSAR data to characterize tropical forest structure is evaluated. The challenge here is the short wavelength of L-band data, and whether can penetrate tropical forests down to the ground. Tomographic analysis is carried out using L-band UAVSAR data from the AfriSAR campaign conducted over Gabon Lopé Park in February 2016. It was found that L-band TomoSAR was able to penetrate into and through the canopy down to the ground, and thus the canopy and ground layers were detected correctly. Then, monitoring tropical forest structure using SAR tomography at L- and P-band are treated. For this, a comparison of the P- and L-band TomoSAR profiles, Land Vegetation and Ice Sensor (LVIS), and discrete return LiDAR is provided in order to assess the ability for TomoSAR to monitoring and estimating the tropical forest structure parameters for enhanced forest management and to support biomass missions. The L- and P-band's performances for canopy penetration are assessed to determine the underlying ground locations. Additionally, the 3D records for each configuration are compared regarding their ability to derive forest vertical structure.

The second part of the thesis tackle the utilization of InSAR techniques in land subsidence monitoring. The idea is to split the estimation of earth's surface deformations into two steps. The first step is to use Maximum Likelihood technique to jointly process Permanent scatterers and Distributed scatterers in order to yield the best estimates of interferometric phases. Then, the second step is to separate the contributions to the interferometric phases due to the scene topography and deformation field from those caused by decorrelation noise and atmospheric disturbances. As a case study, an extensive InSAR analysis of Lebanon site is shown, relying on a data-set of 117 Sentinel-1 satellite data acquired over Lebanon between 2015 and 2019, with high temporal resolution (i.e. 6 days).

Keywords: BIOMASS, Subsidence, Sentinel-1, forest vertical structure, Synthetic Aperture Radar (SAR), TomoSAR, InSAR, L-band, P-band, Gabon, Lebanon.



Résumé

L'objectif de cette thèse est d'exploiter le radar à ouverture synthétique (ROS) multi-lignes de base pour la caractérisation de la structure forestière et la surveillance de l'affaissement des sols. Dans le cas des zones forestières, les paramètres de la structure de la forêt tropicale sont dérivés par la tomographie SAR (TomoSAR). Pour les zones urbaines, la subsidence des sols est étudiée à l'aide des techniques d'interférométrie SAR (InSAR). TomoSAR et InSAR seront en utilisant des images SAR multi-lignes de base sur différents sites. Avant l'analyse tomographique, un algorithme d'étalonnage de phase est nécessaire pour compenser les résidus de phase qui altèrent les données et influent sur la mise au point des données multi-lignes de base. D'abord, une étude tomographique a été réalisée dans les forêts tropicales, où la caractérisation de la forêt a été évaluée à l'aide de la tomographie SAR en bandes L et P. Deuxièmement, différentes techniques InSAR ont été comparées en ce qui concerne leurs performances en matière de surveillance de la déformation de la surface de la Terre, en prenant le Liban comme étude de cas.

La première partie de la thèse présente l'analyse TomoSAR dans la forêt tropicale du Gabon. Un examen des techniques d'étalonnage de phase utilisées sur les données TomoSAR est présenté. La formulation du problème commence par l'étalonnage de phase de la pile de données considérée comme l'entrée principale pour commencer l'application

des algorithmes de traitement des données SAR. Ainsi, les algorithmes d'étalonnage de phase proposés dans la littérature sont discutés. Deux des approches d'étalonnage de phase les plus importantes sont ensuite décrites et discutées en détail. Le potentiel des données TomoSAR en bande L pour caractériser la structure de la forêt tropicale est évalué. Le défi ici est la courte longueur d'onde des données en bande L (en comparaison à la bande P), et la possibilité de pénétrer dans la forêt tropicale jusqu'au sol. L'analyse tomographique est réalisée à partir des données UAVSAR de la bande L en campagne AfriSAR menée sur le parc Gabonais Lopé en Février 2016. Il a été constaté que TomoSAR en bande L est capable de pénétrer dans et à travers la canopée jusqu'au sol, ce qui a permis de détecter correctement les couches de la canopée et du sol. Ensuite, le suivi de la structure de la forêt tropicale est traité à l'aide de la tomographie ROS en bandes L et P. Pour cela, une comparaison des profils TomoSAR en bandes L et P avec des données lidar du capteur (LVIS) est effectuée afin d'évaluer la capacité de TomoSAR à surveiller et à estimer les paramètres de la structure de la forêt tropicale pour une bonne gestion forestière et pour soutenir les missions spatiales sur la biomasse forestière. Les performances des bandes L et P pour la pénétration de la canopée sont évaluées pour déterminer l'emplacement du sol sous-jacent. En outre, les enregistrements 3D pour chaque configuration sont comparés en ce qui concerne leur capacité à dériver la structure verticale de la forêt.

La deuxième partie de la thèse aborde l'utilisation des techniques InSAR dans la surveillance de la subsidence. L'idée est de diviser l'estimation des déformations de surface de la terre en deux étapes. La première étape consiste à utiliser la technique du maximum de vraisemblance pour traiter conjointement les diffuseurs permanents et les diffuseurs distribués afin d'obtenir les meilleures estimations possibles des phases interférométriques. Ensuite, la deuxième étape consiste à séparer les contributions aux phases interférométriques dues à la topographie de la scène et au champ de déformation causées par le bruit de décorrélation et les perturbations atmosphériques. Comme cas d'étude, une analyse approfondie des données INSAR est présentée sur le site Libanais. En s'appuyant sur un ensemble de données de 117 données satellitaires Sentinel-1 acquises entre 2015 et 2019, avec une résolution temporelle élevée (6 jours).

Mots-clés: Biomasse, Subsidence, Sentinel-1, radar à synthèse d'ouverture (ROS), TomoSAR, InSAR, bande L, bande P, Gabon, Liban.



Acknowledgements

First I would like to thank the members of my PhD committee: reporters, Prof Elias RACHID and D. Daniel RAUCOULES, examiners: Dr. Thuy LE TOAN and Prof Husam AYAD who accepted to evaluate my thesis work; invited: Prof Ghaleb FAOUR.

There are no proper words to convey my deep gratitude and respect for my thesis and research supervisors. I would like to thank Prof. Nicolas Baghdadi for giving me the opportunity to do research and be a member of his team, for the continuous support of my PhD study and related research. I would like to thank him from my deep for every support he did during the 3 years and for supporting me in all difficulties that I faced.

I would like to thank Dr. Dinh Ho Tong Minh for his motivation, patience, and immense knowledge. His guidance helped me all the time and it was a great privilege and honor to be under his guidance. I am extremely grateful for what he had offered me.

I would also like to send special thanks to my director at the Lebanese university Prof. Jalal Jomaah for all his help throughout this three years journey. For his guidance, supporting in all situations. I'm grateful for what he provided me during my PhD study and during my Master and BS studies in the Lebanese University.

My deep and sincere gratitude goes to Prof. Chadi Abdallah, for all what he provided

me with, for his continuous supporting and for giving me the opportunity to do research in his team. I sincerely thank him from the bottom of my heart for all his supportive words, for his help in everything I was asking him about and for his continuous follow up. I will be truly indebted to him throughout my life time.

Also I would like to thank Dr. Olivier Strauss, for his support during three years of research and thanks for his helpful advises.

My earnest thanks to the National Council for Scientific Research (Lebanon), university of Montpellier, and Agence universitaire de la Francophonie (AUF) for providing me the funding which allowed me to undertake this research.

I am extremely grateful to my parents for their love, prayers, caring and sacrifices for educating and preparing me for my future. Many thanks to my father who assisted me in all my stages and who was always encouraging me - too pity he cannot see me graduate but his soul will be always beside me and his memory will be eternal. Grateful thanks to my mother for her patience and sacrifices. My brother and my sisters, many thanks for all your help and support in everything. Last, but not least, I'm thankful to all my friends for all the moral support they provided. Hussein Saied, Ali Nsarallah, Hassan Bazi, special thanks for them for the beautiful days that we spent together and for being beside me in my worst situations.



Résumé Français

Contents

Contexte général	19
Missions ROS	21
Questions de recherche et objectifs de la Thèse	23
Contributions à la these	24
Résumé de la thèse	25
Conclusion générale	27

Contexte général

L'augmentation continue de la population entraîne la consommation de ressources naturelles tels que l'eau des puits et le bois forestier. Les prélèvements excessifs d'eau dans les puits souterrains dans des zones connues pour leur forte densité d'urbanisation et leur forte inflation démographique peuvent entraîner des déformations entraînant des catastrophes telles que des affaissements de terrain. Les forêts, en revanche, constituent le principal apport de bois pour les constructions dans les villes et les villages et sont donc soumises à une consommation considérable. Les incendies fréquents sur des grandes

zones, principalement dus à l'intensification des activités humaines, affectent de nombreuses forêts du monde, comme les forêts tropicales. Les gouvernements ont de plus en plus besoin d'avoir des systèmes d'alerte précoce qui fournissent des informations essentielles avant l'apparition de catastrophes. Ces dernières années, les données de télédétection sont largement utilisées pour générer des cartes de subsidence et des activités de gestion forestière. Depuis la fin des années 1970, la télédétection radar (radar à synthèse d'ouverture, ROS) est considéré comme un outil puissant pour l'observation de la surface de la Terre. Plusieurs facteurs sont impliqués dans la détermination du succès des outils de télédétection dans les applications. L'utilisation de techniques de traitement du signal numérique revêt une grande importance. C'est le cas de la compression des impulsions et de la synthèse d'antennes, ainsi que des ROS aéroportés et spatiaux capables de donner des images de vastes parties de la surface de la Terre, allant de quelques kilomètres à plusieurs centaines de kilomètres, avec une résolution spatiale allant de dizaines de mètres à des dizaines de centimètres [Rocca, 1987; Curlander and McDonough, 1991; Franceschetti and Lanari, 2018]. De plus, les systèmes ROS utilisent des capteurs actifs fonctionnant dans les hyperfréquences, généralement dans les bandes X, C, L et P. Une telle utilisation permet l'acquisition de données quelles que soient les conditions météorologiques et indépendamment de l'éclairage du soleil. Ceci constitue donc un avantage important par rapport aux techniques d'imagerie optique. Les ROS spatiaux ont fourni, au cours des trente dernières années, une couverture continue de presque toute la surface de la Terre, où les données ont été acquises indifféremment sur les montagnes, les glaciers, les milieux urbains, et les zones marines et forestières. De plus, les capacités des systèmes ROS permettent également d'obtenir des informations relatives à la phase et à la polarisation, en plus de l'amplitude des formes d'onde reçues. Celles-ci nous fourniront une caractérisation, en termes de propriétés géométriques et électromagnétiques, de la scène imagée. Pour comparer deux ou plusieurs images ROS de la même scène, il est possible d'effectuer une analyse interférométrique basée sur la préservation des informations de phase. L'interférométrie ROS (InSAR) a montré, en utilisant la diversité temporelle et ou spatiale parmi les acquisitions, qu'il s'agissait d'un outil majeur pour la déduction d'informations précises sur la topographie de la scène photographiée

et son champ de déformation, ainsi que sur la distribution spatiale des champs atmosphériques. Par conséquent, il concerne plusieurs secteurs, dont la sismologie, la cartographie topographique, la volcanologie, la subsidence du sol et les soulèvements dus au pompage de fluides, les dynamiques atmosphériques et la glaciologie [Bamler and Hartl, 1998; Rosen et al., 2000; Rodriguez and Martin, 1992]. La polarimétrie ROS (PolSAR) utilise la diversité polarimétrique pour caractériser les cibles en fonction de leurs propriétés électromagnétiques. Les applications résultantes comprennent: la détermination de la forme et de l'orientation d'une cible, l'estimation de l'humidité du sol et de la rugosité de surface, la classification et la décomposition des mécanismes de diffusion [Inglada et al., 2006; Freeman, 2007; Cloude and Pottier, 1997, 1996]. D'autres techniques de traitement, telles que l'interférométrie ROS polarimétrique (PolInSAR) combinant des informations polarimétriques et interférométriques, jouent un rôle essentiel dans l'analyse de scénarios complexes. Ce dernier avait prouvé sa capacité à fournir une caractérisation significative des zones forestières. Cela fait de l'acquisition SAR une ressource importante pour la surveillance et l'évaluation de la biomasse en milieux forestiers [Cloude and Papathanassiou, 1998; Papathanassiou and Cloude, 2001; Treuhaft and Siqueira, 2000].

Missions ROS

En 1978, la NASA a lancé le premier capteur ROS spatial à bord du satellite SEASAT-A, dédié aux applications civiles. Le système a été conçu pour fonctionner en bande L (longueur d'onde de 23 cm). L'expérience SEASAT-A s'est surtout orientée vers les études océanographiques et, bien qu'elle ait été limitée dans le temps à environ 80 jours en raison des graves pannes, elle a fourni aux scientifiques des données qui ont débouché sur des études intéressantes dans plusieurs domaines (géologie, glaciologie, etc.). Cela avait prouvé que le ROS spatial était très efficace pour les applications terrestres. SIR-A et SIR-B sont deux capteurs ROS similaires qui ont succédé à SEASAT-A et ont été lancés respectivement en 1981 et 1984, à bord de la navette spatiale de la NASA. Cependant, pour ce qui est de l'InSAR spatial, les premiers résultats importants n'ont été atteints que dans la seconde moitié des années 1980 [Gabriel et al., 1989; Gabriel and Goldstein, 1988; Zebker and

[Goldstein, 1986; Prati et al., 1989], surtout parce qu'à cette époque, les données représentées par une petite sélection d'images SEASAT-A étaient les seules données disponibles pour les applications interférométriques. En 1991, après le lancement du satellite ERS-1 de l'Agence spatiale européenne (ESA), la communauté scientifique a commencé à disposer d'un grand nombre de données adaptées au traitement interférométrique. Le satellite lancé affichait des performances exceptionnelles en termes d'étalonnage des images, de stabilité du matériel et de précision du traçage de son orbite au niveau de dm et de cm. En 1995, ERS-2 a été lancé. C'était le jumeau identique d'ERS-1. ERS-1 et ERS-2 ont fonctionné en mode parallèle au cours de la mission TANDEM, dans laquelle ils réalisaient les images de la même région [Perissin and Wang, 2011]. Le capteur ROS européen suivant était le système ASAR lancé en 2002 à bord du satellite ENVISAT. Comparé aux systèmes ERS, le système ASAR était doté de fonctionnalités avancées, telles que la double polarisation et le guidage du faisceau. Il a été conçu pour offrir une compatibilité totale des données avec les précédents ROS [Guarnieri et al., 2003; Colesanti et al., 2003; Guarnieri and Prati, 2000]. Il est très important de mentionner les autres ROS spatiaux en raison de leurs capacités interférométriques. Il s'agit de RADARSAT-1 en bande C piloté par l'Agence spatiale canadienne (CSA, lancé en 2006), JERS et ALOS-1/PALSAR en bande L pilotés par l'Agence spatiale japonaise (JAXA, lancés respectivement en 1992 et 2006), SIR-C/X-SAR lancé par la NASA en avril et octobre 1994 à bord d'une navette spatiale, un capteur similaire auquel a été ajoutée une autre antenne de réception lancé en 2000 à bord de la navette spatiale dans le but de disposer d'une carte topographique couvrant presque toute la surface de la Terre. Cette dernière mission s'appelait SRTM (Shuttle Radar Topography Mission) et donnait naissance à un modèle numérique de terrain largement utilisé par la communauté scientifique [Rabus et al., 2003]. De plus, nous ne devrions jamais oublier de mentionner les trois nouvelles missions lancées en 2007. Il s'agit de la constellation COSMO-SkyMed (bande X) pilotée par l'Agence spatiale italienne (ASI), la constellation TERRASAR-X (bande X) pilotée par l'agence spatiale allemande (DLR) et le satellite canadien RADARSAT-2 (bande C). En raison du contrôle orbital amélioré de ces systèmes et de leur faible temps de revisite, ils étaient supposés offrir de meilleures capacités interférométriques par rapport au passé. Le radar ALOS-2/PALSAR (ROS japon-

ais) lancé en 2014 constitue une mise à niveau importante du radar PALSAR-1, permettant des meilleures résolutions spatiales (3m). L'Agence spatiale européenne (ESA) a récemment lancé les deux satellites Copernicus Sentinel-1A/1B (S1A lancé en 2014 et S1B en 2016). Enfin, bien que les systèmes ROS aéroportés ne puissent pas rivaliser avec les systèmes spatiaux dans les capacités de couverture, on peut dire qu'ils ont prouvé, en raison de leur capacité de charger du matériel lourd et de leur souplesse d'utilisation, leur importance à être utilisés soit dans la réalisation de vols sur des zones spécifiées ou dans le développement de nouvelles modalités d'imagerie ROS. Il existe plusieurs exemples de ROS aéroportés, comme le capteur américain AIRSAR, piloté par le Jet Propulsion Laboratory (JPL) et pouvant acquérir des données polarimétriques dans les bandes C, L et P, les capteurs français RAMSES et SETHI pilotés par l'ONERA et pouvant fonctionner également en mode polarimétrique dans les bandes C, Ka, Ku, L, P, S, W, le radar E-SAR du DLR pouvant acquérir des données en mode polarimétrique dans les bandes L, P, S et des données en une seule polarisation dans les bandes C et X, le ROS suédois CARABAS piloté par l'agence suédoise de recherche pour la défense (FOI) et qui opère dans la bande VHF. Le ROS UAVSAR JPL/NASA a récemment volé pour acquérir des données polarimétriques en bande L sur les forêts du Gabon dans le cadre de la campagne AfriSAR de 2016.

Questions de recherche et objectifs de la Thèse

La thèse se concentre sur les applications multi-lignes de base ROS telles que la Tomographie SAR (TomoSAR) et l'Interférométrie SAR (InSAR) pour détecter à distance la surface de la Terre, telle que les forêts et les zones urbaines. Dans les zones forestières, les capacités de la TomoSAR en bande P à pénétrer à travers le couvert forestier tropical jusqu'au sol sont évaluées dans différents écosystèmes. Bien que caractériser les structures de la forêt en utilisant la TomoSAR en bande L semble être limité [[Ho Tong Minh et al., 2015a](#)]. Minh et al. (2015) ont utilisé les données acquises sur les forêts tropicales de Guyane française dans le cadre de la campagne TropiSAR. Notre étude tomographique conduit à répondre aux questions suivantes: les signaux en bande L sont-ils capables de pénétrer dans la structure de la forêt tropicale? Quel est l'impact de l'étalonnage de phase sur l'analyse tomographique?

Peut-on utiliser les données TomoSAR pour dériver des paramètres de structure forestière qui permettront d'améliorer les estimateurs de biomasse? La deuxième étude réalisée ici est l'exploitation de différentes techniques InSAR appliquées aux données ROS acquises en bande C afin de surveiller les déformations de la surface de la Terre et de générer une carte de subsidence avec une précision millimétrique, en prenant le Liban comme étude de cas. L'objectif général de la thèse est de fournir une meilleure compréhension des différentes applications ROS multi-lignes de base pour la télédétection de scénarios naturels. L'analyse TomoSAR en bandes L et P a été appliquée et comparée aux possibilités de dériver les paramètres de structure de la forêt tropicale. Un autre objectif était de surveiller et de générer une carte de subsidence des terres pour le Liban à l'aide de différentes techniques InSAR.

Contributions à la these

Premièrement, nous avons développé une stratégie pour caractériser la structure de la forêt tropicale en bande L. Une comparaison des données TomoSAR en bandes L et P est effectuée en utilisant les données AfriSAR de la campagne menée dans les forêts Gabonaises. Avant de poursuivre l'analyse tomographique, différentes méthodologies d'étalonnage de phase ont été mises en œuvre. Les méthodes d'étalonnage de phase utilisées ici sont l'étalonnage de phase à l'aide de la somme du produit Kronecker (SKP) et l'étalonnage de phase par double localisation de centre de phase. Nous avons mis en œuvre un étalonnage de phase des données tomographiques aéroportées via une double localisation de centre de phase d'une manière appropriée et dont les étapes diffèrent de celles proposées par [Tebaldini et al., 2016]. La capacité de la tomographie ROS en bandes L et P à surveiller et à estimer les paramètres de structure de la forêt tropicale pour une meilleure gestion forestière mais aussi pour soutenir les missions satellitaires biomasse à venir a été évalué. Les paramètres et les indices de la structure forestière peuvent être estimés à partir des profils de réflectivité radar 3D parfaits générés par inversion TomoSAR. Nos résultats dans cette partie ouvrent des perspectives d'utilisation des données TomoSAR afin de classer les forêts en catégories structurelles. En utilisant cette classification structurelle, nous exam-

inerons si nous pourrions estimer plus précisément la biomasse forestière et la productivité du bois aérienne, au cas où nous aurions inclus les informations structurelles.

Deuxièmement, la technique de série chronologique InSAR PS/DS (diffuseur persistants (Persistent Scatter, PS) ou diffuseurs distribués (Distributed Scatterers, DS) a été appliquée aux données Sentinel-1 ROS en bande C. Une carte de la subsidence des terres a été générée pour le Liban. Une comparaison des techniques d'interférométrie radar multi-temporelles utilisant les données Sentinel-1 est implémentée. Notre objectif pour cette partie est d'importer l'étalonnage en phase des données ROS dans la chaîne de traitement des techniques InSAR. L'étalonnage de phase des données InSAR doit éliminer les erreurs orbitales et améliorer les résultats InSAR.

Résumé de la thèse

Cette thèse comprend six chapitres consécutifs. Le chapitre 1 présente le contexte, l'historique des missions ROS, les objectifs de recherche, la formulation des problèmes, les contributions de la thèse et les grandes lignes des résultats obtenus.

Le chapitre 2 donne un aperçu des applications du radar à synthèse d'ouverture dans les forêts et les zones urbaines. Il fournit les bases et la géométrie du ROS et présente les techniques multi-lignes de base ROS allant de l'interférométrie à la tomographie, ainsi qu'une revue de l'étalonnage de phase tomographique. Les trois derniers chapitres représentent des travaux publiés dans des revues scientifiques à comité de lecture.

En conséquence, le chapitre 3 présente l'évaluation des données TomoSAR en bande L pour l'estimation de la structure verticale des forêts tropicales. Ce chapitre a présenté les résultats tomographiques de la bande L UAVSAR dans le parc national de La Lopé au Gabon. Dans ce chapitre, il est prouvé que l'imagerie TomoSAR en bande L peut être réalisable même dans les forêts tropicales. Une étude tomographique a été mise en oeuvre en utilisant les données UAVSAR en bande L de la NASA/JPL recueillies lors de la campagne AfriSAR de 2016. Nous montrons des tomogrammes dans différentes sections de la Lopé et nous les avons validés avec les données SFL (Space Flight Laboratory). Une

comparaison qualitative est faite entre les profils de Capon et les formes d'onde Lidar LVIS (Laser Vegetation Imaging Sensor) dans différentes régions d'intérêt du parc de la Lopé au Gabon. Enfin, la hauteur du couvert forestier a été estimée. Ces résultats peuvent donc confirmer nos attentes concernant la capacité de la TomoSAR bande L à caractériser avec précision la structure tridimensionnelle des forêts tropicales. Afin d'analyser les résultats de la TomoSAR, une bonne connaissance des principaux facteurs permettant de contrôler efficacement la bonne mise au point des marqueurs au-dessus du sol est nécessaire. Ces facteurs incluent: la qualité des données tomographiques, les méthodes d'estimation de la puissance utilisées dans l'inversion tomographique, la fréquence de fonctionnement du signal TomoSAR et la résolution verticale de TomoSAR. L'article de ce chapitre a été publié dans la revue *Remote Sensing* en février 2019.

Le chapitre 4 présente la surveillance de la structure des forêts tropicales à l'aide de la tomographie ROS en bandes L et P. Ce chapitre propose une meilleure compréhension des capacités des bandes L et P à dériver des paramètres de structure de la forêt qui améliorent les performances des estimateurs de biomasse et facilitent les activités de gestion forestière. Dans le cadre de ce travail, le potentiel de l'imagerie TomoSAR en bande L à estimer les paramètres de structure de la forêt tropicale a été évaluée. Une étude tomographique a été réalisée à l'aide des données UAVSAR en bande L de la NASA/JPL et des données SETHI en bande P de l'ONERA collectées au cours de la campagne AfriSAR en 2015 et 2016. Nous avons montré des tomogrammes en bande L et en bande P dans différentes sections de la Lopé et nous les avons validés avec un modèle de hauteur de la canopée (Canopy Height Model, CHM) en utilisant les données SFL. Nous avons ensuite démontré que l'analyse s'améliorait considérablement lorsque les données en vol étaient corrigées des phases résiduelles liées aux perturbations dues aux incertitudes liées à l'allocation des trajectoires de vol lors des acquisitions de données. L'impact de la correction de phase dans l'inversion tomographique apparaît dans le tomogramme à la distance oblique (slant range) découpée avant et après l'étalonnage de phase. Une comparaison qualitative est faite entre les profils de Capon en bandes L et P et les longueurs d'onde LVIS dans une zone d'intérêt appelée OKO2 dans le parc Gabonais de la Lopé. Enfin, la hauteur maximale de la forêt à partir des données UAVSAR et SETHI a été estimée. Ensemble, ces

résultats confirment nos attentes concernant la capacité de TomoSAR à caractériser avec précision la structure 3D des forêts tropicales. Le document de ce chapitre a été publié dans *Remote Sensing* en juillet 2019.

Le chapitre 5 montre la comparaison des techniques d'interférométrie radar multi-temporelles utilisant les données Copernicus Sentinel-1 et prenant le Liban comme étude de cas. Dans ce travail, les cibles PS et DS ont été traitées conjointement et utilisées pour générer une carte de subsidence pour le Liban. Les nouveaux satellites Sentinel-1 lancés par l'Agence spatiale européenne fournissent des données à haute précision et avec une résolution temporelle très fine. La constellation Sentinel-1 est le seul système satellitaire offrant gratuitement des séries chronologiques denses avec une couverture mondiale de 6 jours. Le but de ce chapitre est de comprendre les performances de deux nouvelles techniques, PSI (Persistent Scatterer Interferometry) et PS/DS, utilisant Sentinel-1 basé sur l'observation du terrain par balayage progressif (based on the Terrain Observation by Progressive Scans mode, TOPS). Nous étudions la capacité du ROS en bande C à déterminer les phénomènes de subsidence au sol au Liban sur la base des données Sentinel-1 de 2015 à 2019. Pour estimer la subsidence au sol, nous appliquons deux méthodes. La première méthode est la technique PSI standard. Deuxièmement, une approche basée sur l'estimateur maximum de vraisemblance [Ho Tong Minh et al., 2015b], qui exploite non seulement les points stables comme les diffuseurs PS mais également les DS. L'augmentation du nombre de points de mesure PS/DS identifiés au sol résultant de cette approche renforce la confiance dans les mesures du mouvement et du déplacement du sol, par rapport à l'algorithme précédent reposant sur PS seulement [Ferretti et al., 2001; Hooper et al., 2004]. Enfin, le chapitre 6 résume les résultats de la thèse en soulignant les conclusions des chapitres précédents, la contribution scientifique principale, ainsi que des suggestions et des perspectives supplémentaires.

Conclusion générale

Cette thèse a examiné l'utilisation de la télédétection de scénarios naturels à travers plusieurs acquisitions multi-lignes de base ROS. L'objectif général de la thèse est

d'exploiter les algorithmes et applications multi-lignes de base ROS en forêts et en zones urbaines. Nos recherches ont nécessité différents ensembles de données spatiales et aéroportées acquises sur différents sites. Les réalisations accomplies dans la première partie de la thèse montrent que la technique TomoSAR est capable de dériver la structure de la forêt dense. Même si, il a été démontré que les écrans de phase dus aux perturbations de propagation constituaient un problème crucial dans les applications multi-lignes de base, aussi bien interférométriques que tomographiques. Ainsi, différentes techniques d'étalonnage de phase ont été appliquées et validées. Cependant, un inconvénient de ces techniques est que, en utilisant SKP, nous avons évalué la capacité des données en bande L à pénétrer dans la forêt tropicale de la canopée à la couche de sol, de manière à pouvoir extraire le modèle numérique de terrain sous la forêt. Lors de l'utilisation de la technique PCDL, seul l'étalonnage de phase est effectué après élimination des résidus de phase du SLC d'origine, sans extraction de la phase de terrain. Des techniques de formation de faisceaux à super-résolution ont été mises en œuvre pour obtenir des profils tomographiques parfaits. Pour les données TomoSAR en bande L et P, nous avons identifié les différentes couches de forêt (canopée et couche de sol) de manière à obtenir des indices de structure de la forêt qui améliorent les performances des estimateurs de biomasse. En ce qui concerne la seconde partie, différentes techniques InSAR appliquées sur des séries temporelles ROS ont été évaluées. Une carte de la subsidence des terres est générée en prenant le Liban comme étude de cas. La faisabilité des données Sentinel-1 en bande C pour estimer l'affaissement du sol est démontrée. La technique PS/DS semble être une technique prometteuse pour surveiller les risques liés à la surface du sol. Nous devons à l'avenir combiner la technique InSAR avec des mesures in situ de manière utile pour surveiller et suivre l'affaissement du sol au Liban. Il existe de nombreuses stations GPS différentielles situées au Liban sur différents sites du pays. Notre travail dans cette partie consiste donc à générer l'historique des déplacements verticaux et horizontaux du GPS. Ensuite, la corrélation entre les mesures InSAR et les mesures GPS peut être effectuée. Pour améliorer la qualité des résultats InSAR, nous proposons de mettre en œuvre l'étalonnage de phase des données Sentinel-1 multi-lignes de base à l'aide de PCDL appliqué sur DS

(Distributed Scatterers), de manière à éliminer les erreurs orbitales et les perturbations de phase générées par les données InSAR.

Perspectives de tomographie SAR

En ce qui concerne la première partie, notre objectif est d'estimer les indices de structure de la forêt, tels que les indices horizontaux et verticaux, qui jouent un rôle dans les algorithmes d'estimation de la biomasse et dans l'amélioration des activités de gestion forestière. Cependant, la structure de la forêt est considérée comme un facteur important de son écologie en raison de sa corrélation avec divers processus écologiques [Pretzsch et al., 2010; Shugart et al., 2010; Mundell et al., 2010]. En outre, elle est également utilisée comme indicateur pour détecter la biodiversité, où les forêts à structure verticale favorisent la biodiversité de plusieurs taxons [Boncina, 2000; Ishii et al., 2004; Schall et al., 2018]. De plus, l'hétérogénéité structurelle verticale ou horizontale peut améliorer la résistance des écosystèmes forestiers aux perturbations [Dobbertin, 2005; Pretzsch et al., 2016]. Cependant, il est très important de connaître la structure de la forêt pour pouvoir en comprendre la dynamique. Il est vraiment très difficile de trouver une définition appropriée et claire de la structure forestière. En outre, les paramètres de structure de la forêt varient en fonction de la méthode de leurs estimations (mesures in situ ou estimation par télédétection). Les descripteurs terrain de la structure forestière sont souvent dérivés des mesures de la taille de chaque arbre individuellement. Cependant, les descripteurs de télédétection dépendent de l'hétérogénéité de la structure du couvert forestier d'une zone donnée. Notre intérêt pour les études futures est d'utiliser la modélisation forestière, la télédétection Lidar et la TomoSAR aéroportée afin de pouvoir répondre à la question: «Comment pouvons-nous estimer la structure d'une forêt à l'aide de la télédétection? Et qu'est le rôle joué par la structure forestière dans l'estimation de la biomasse forestière et de la productivité du bois aérien? Notre objectif est d'utiliser les descripteurs verticaux et horizontaux pouvant être mesurés par télédétection afin de classer les forêts en catégories structurelles. En utilisant cette classification structurelle, nous examinerons si nous serons en mesure d'estimer plus précisément la biomasse forestière et la productivité du bois aérien dans le cas où nous incluons les informations structurelles.

Perspectives de interférométrie SAR

En règle générale, les systèmes ROS spatiaux sont équipés de systèmes de vecteurs d'état qui donnent au capteur une position de précision en centimètres. Les informations sur les produits orbitaux sont obtenues après traitement de diverses données auxiliaires, telles que les informations d'attitude des capteurs satellites, les éphémérides du système de positionnement global et les paramètres d'un modèle physical [Wermuth et al., 2009]. Obtenir des informations sur les produits orbitaux est indispensable pour la formation d'images ROS et donc pour le traitement par interférométrie. Toute perturbation survenant sur l'orbite provoquera des résidus qui altéreront le traitement des images ROS. Notre objectif pour ce travail est de mettre en œuvre l'étalonnage de phase des données ROS spatiales afin de compenser les erreurs orbitales et les erreurs des lignes de base afin de de corriger les données ROS. Cela aidera à améliorer les résultats d'InSAR.

Part I

Introduction and Synthetic Aperture Radar algorithms and applications

Introduction

Contents

1.1	General context	33
1.2	SAR missions	35
1.3	Research problem and Objectives	37
1.4	Thesis contributions	38
1.5	Thesis outline	39

1.1 General context

The continuous increase in population leads to the consumption of natural resources which is reflected in several variables. Such natural resources are ground well water and Forest wood. The excessive water withdrawal from groundwater wells in areas known with their vitality, high population inflation, and a crowded number of buildings can lead to deformations that can cause disasters. Forests, on the other hand, are the main supplement of wood for construction and fabrics in cities and villages, and accordingly, are subjected to huge consumption. Frequent and large-scale fires, mainly caused by increased human activity, affect many forests around the world like tropical forests. A significant need for

governments emerges aiming to have early warning systems that provide critical information before disasters occurrence. In recent years, remote sensing has played a major role in carrying out analytical analysis in natural resources and in observing the earth's surface. Nowadays, Remote sensing data are widely used in generating land subsidence maps and forest management activities.

Since late 1970, the remote sensing imaging tool, Synthetic Aperture Radar (SAR), has considered as a powerful one in the observation of the earth's surface. Several factors are implicated in determining the success of such remote sensing tools in the applications. The utilization of techniques with digital signal processing is of high importance. These are such as pulse compression and antenna synthesis and also airborne and spaceborne SAR which are able to give images of wide parts of the earth's surface ranging from few kilometers up to hundreds of them and with a spatial resolution ranging from tens of meters to tens of centimeters [Rocca, 1987; Curlander and McDonough, 1991; Franceschetti and Lanari, 2018]. Moreover, SAR systems use active sensors that operate in the microwave regimes, typically in C, L, P, and X bands. Such utilization permits the acquisition of data regardless of the weather conditions and independently on the illumination of the sun. This, therefore, constitutes an important advantage over the optical imaging techniques. Spaceborne SARs has provided, in the last thirty years, continuous coverage of almost the entire Earth's surface, where data was acquired indifferently over the mountain, ice, urban, sea, and forest areas. In addition, the capabilities of SAR systems allows also getting information related to the phase and polarization, besides the amplitude of received waveforms. These will provide us with a characterization, in terms of the geometric and electromagnetic properties, of the imaged scene. To compare two or more SAR images of the same scene, it is possible to do an interferometric analysis based on preserving phase information. SAR Interferometry (InSAR) has shown, by using temporal and/or spatial diversity among acquisitions, that it is a major tool in inferring accurate information concerning the topography of the imaged scene and also its deformation field, in addition to the spatial distribution of atmospheric fields. Therefore, it involves several sectors including seismology, topographic mapping, volcanology, ground subsidence, and uplifts because of fluid injection, atmospheric dynamics, and glaciology [Bamler and Hartl, 1998; Rosen

et al., 2000; Rodriguez and Martin, 1992]. SAR polarimetry (PolSAR) uses the polarimetric diversity to characterize targets depending on their electromagnetic properties. Resulting applications include: determining the shape of a target and its orientation, estimating the moisture of soil and the roughness of a surface, classifying and decomposing scattering mechanisms [Inglada et al., 2006; Freeman, 2007; Cloude and Pottier, 1997, 1996]. Other processing techniques like Polarimetric SAR Interferometry (PolInSAR) that combines between polarimetric and interferometric information plays a vital role in analyzing complex scenarios. The latter had proved its ability to provide a significant characterization of forested areas. This makes SAR acquisition an important resource for both monitoring and biomass assessment in forested environments [Cloude and Papathanassiou, 1998; Papathanassiou and Cloude, 2001; Treuhaft and Siqueira, 2000].

Recently, the SAR community is considering the exploitation of SAR data to conduct tomographic analyses as an important object of growing interest. SAR Tomography (TomoSAR) techniques are today considered as attractive tools for characterizing the complex urban scenarios and also the forested areas [Gini et al., 2002b; Sauer et al., 2007; Cloude, 2007; Fornaro and Serafino, 2006].

1.2 SAR missions

In 1978, NASA launched the first space-borne SAR sensor aboard the satellite SEASAT-A which was dedicated to civilian applications. The system was designed to function on the L-band (23 cm wavelength). Though the orientation of SEASA-A experiment was mainly towards oceanographic studies, and though it was limited in time to around 80 days because of the hard failures, it provided scientists with data that has resulted in interesting studies in several fields as land analysis, geology, and glaciology. This had proved that the spaceborne SAR is highly effective in land applications. SIR-A and SIR-B, are two similar SAR sensors that came after SEASAT-A and were launched in 1981 and 1984, respectively aboard NASA space shuttle. As long as spaceborne InSAR is concerned, however, the first important results were achieved only in the second half of the 1980' [Gabriel et al., 1989; Gabriel and Goldstein, 1988; Zebker and Goldstein, 1986; Prati et al., 1989], especially be-

cause at that time, data represented by a small selection of the SEASAT-A images were the only available data for the interferometric applications. The actual beginning of the scientific community to have a big set of data that is suitable for interferometric processing was in 1991, after launching the European Space Agency (ESA) satellite ERS-1. The launched satellite was with an outstanding performance in terms of image calibration, hardware stability, and the accuracy in tracing its orbit at the level of dm and cm. In 1995, ERS-2 was launched. It was the identical twin of ERS-1. ERS-1 and ERS-2 worked in a parallel mode during the TANDEM mission, where they were imaging the same area [Perissin and Wang, 2011]. The following European SAR sensor was the ASAR system which was launched in 2002 aboard ENVISAT satellite. As compared with ERS systems, ASAR system was with advanced capabilities, such as dual-polarization and beam steering. It was designed to have full data compatibility with previous ones [Guarnieri et al., 2003; Colesanti et al., 2003; Guarnieri and Prati, 2000]. It is highly important to mention other spaceborne SARs because of their interferometric capabilities. These are: C-band RADARSAT-1 that was flown by the Canadian Space Agency (CSA) in 2006, L-band system JERS and ALOS PALSAR that were flown by the Japanese Space Agency (JAXA) in 1992 and 2006, respectively, SIR-C/X-SAR sensor that was launched by NASA in April and October 1994 aboard the space shuttle, one similar sensor that was augmented by another receiving antenna and launched in 2000 aboard the shuttle in aim to have a topography map that covers almost the entire Earth's surface. The mission was called SRTM (Shuttle Radar Topography Mission) and resulted in a model that is now available for the public use which is: planetary Digital Elevation Model (DEM) [Rabus et al., 2003].

Furthermore, we should never forget to mention the three new missions that flown in 2007. These spaceborne SARs mentions were: COSMO-SkyMed constellation (X-band) that was flown by the Italian Space Agency (ASI), TERRASAR-X (X-band) that was flown by the German Aerospace Center (DLR), and the Canadian C-band RADARSAT-2. Due to the enhanced orbital control of these systems and their shorter revisit times, they were supposed to give better interferometric capabilities with respect to the past. Advanced Land Observing Satellite 2 (ALOS 2), also called Daichi 2, is a 2-ton Japanese satellite launched in 2014. The PALSAR-2 radar is a significant upgrade of the PALSAR radar, allowing higher-

resolution (1x3m per pixel) spotlight modes in addition to the 10m resolution survey mode inherited from the ALOS spacecraft. Recently, the European Space Agency conducted the Sentinel-1 Copernicus Programme satellite composed of two satellites Sentinel-1A and Sentinel-1B. The first satellite, Sentinel-1A, launched on 3 April 2014, and Sentinel-1B was launched on 25 April 2016. Both satellites lifted off from the same location in Kourou, French Guiana.

Finally, though that airborne SAR systems cannot compete for the spaceborne systems in the coverage capabilities, we can say that they proved, due to their capability to load heavy equipment and their flexibility in use, their importance to be used either in the carry out of the radar surveys on specified areas or in the development of new SAR imaging modalities. There are several examples of airborne SARs as American AIRSAR, that was flown by the Jet Propulsion Laboratory (JPL) and which can acquire quad pol data in C, L, and P bands, the French RAMSES that was flown by ONERA and can work in quad-pol mode in C, Ka, Ku, L, P, S, W bands, DLR's E-SAR that can acquire quad pol data in L, P, S bands and a single pol data in bands C and X, and the Swedish CARABAS that was flown by the Swedish Defense Research Agency (FOI) and is operating in the VHF band, recently, UAVSAR JPL/NASA was flown to acquire fully polarimetric L-band data over Gabon forests in the frame of AfriSAR campaign in 2016.

1.3 Research problem and Objectives

The dissertation focuses on SAR Multibaseline applications such as TomoSAR and In-SAR to remotely sense the earth's surface like forests and urban areas.

In forest areas, P-band TomoSAR abilities in penetrating through tropical forest canopy down to the ground are assessed in different ecosystems. While Characterizing forest structures using L-band TomoSAR seems to be limited [[Ho Tong Minh et al., 2015a](#)]. Min et al., (2015) used data acquired over tropical forests in French Guiana in the frame of TropiSAR campaign. Our tomographic study leads to answer the following questions: are L-band signals capable to penetrate tropical forest structure? what is the impact of phase calibration

on tomographic analysis? Can one use TomoSAR data to derive forest structure parameters that enhance biomass estimators?

The second study carried out here is the exploitation of different InSAR techniques applied on SAR data acquired at C band in order to monitor earth's surface deformations and generate a subsidence map with millimetric accuracy, taking Lebanon as a case study.

The general objective of the dissertation is to provide a better understanding of different Multibaseline SAR applications for the remote sensing of natural scenarios. TomoSAR analysis at L- and P-band was applied and compared with the capabilities to derive tropical forest structure parameters. another objective was to monitor and generate land subsidence map for Lebanon through different InSAR techniques

1.4 Thesis contributions

First, we developed an enhanced strategy to characterize tropical forest structure at L-band. A comparison of L-band and P-band TomoSAR data is done using AfriSAR data campaign carried out over Gabon forests. Before carrying on tomographic analysis, different phase calibration methodologies have been implemented. Phase calibration methods were used here are phase calibration using Sum of Kronecker Product (SKP) and phase calibration via phase center double localization. We implemented phase calibration of airborne tomographic data via phase center double localization in a proper way that differs in its steps than the proposed one by [\[Tebaldini et al., 2016\]](#).

The ability of SAR tomography at L- and P-band to monitor and estimate the tropical forest structure parameters for enhanced forest management and to support biomass missions has been evaluated. Forest structure parameters and indices can be estimated from the perfect 3D radar reflectivity profiles generated by TomoSAR inversion. Our results in this part open prospects to use TomoSAR data in order to classify the forests into structural categories. Using this structural classification, we will explore if we will be able to estimate more accurately both forest biomass and above-ground wood productivity in case we included the structural information.

Second, PS/DS InSAR time series technique has been applied to Sentinel-1 SAR C-band data. Land subsidence map has been generated for Lebanon. A comparison of multi-temporal radar interferometry techniques using Sentinel-1 data is implemented. Our prospect to this part is to import the phase calibration of SAR data in the processing chain of InSAR techniques. Phase calibration of InSAR data must get rid of orbital errors and enhance the InSAR results.

1.5 Thesis outline

This thesis consists of six consecutive chapters. Chapter 1 presents the context, historical background of SAR missions, research objectives and problem formulation, Thesis contributions, and the outline of the thesis.

Chapter 2 provides an overview of Synthetic Aperture Radar applications in forests and urban areas. It provides SAR basics and geometry and presents SAR Multibaseline techniques from interferometry to tomography, as well as a review on tomographic phase calibration. The latter three chapters represent published and draft work to be submitted in peer-reviewed scientific journals. Therefore each chapter can be read without the necessity of reading the previous chapter.

Accordingly, in chapter 3 the evaluation of L-band TomoSAR data in estimating tropical forest vertical structure is discussed. This chapter reports the L-band UAVSAR tomographic results carried out in the Gabon Lope National Park. The paper of this chapter was published to the Remote Sensing in February 2019 (see Appendix A).

Chapter 4 presents the Monitoring of tropical forest structure using SAR tomography at L- and P-band. This chapter proposes a better understanding of the capabilities of L and P-band to derive forest structure parameters that enhance the performance of biomass estimators and help in forest management activities. The paper of this chapter was submitted to the Remote Sensing in July 2019 (see Appendix B).

Chapter 5 shows the comparison of multi-temporal radar interferometry techniques

using Sentinel-1 taking Lebanon as a case study. The paper of this chapter will be submitted to the Remote Sensing Journal (see Appendix C).

Finally, chapter 6 summarizes the thesis findings by highlighting the conclusions from previous chapters, the main scientific contribution, and further suggestions and perspectives.

Synthetic Aperture Radar algorithms and applications

Contents

2.1	Synthetic Aperture Radar basics	41
2.2	Interferometry SAR	48
2.3	Permanent scatterer interferometry	49
2.4	Tomography SAR background	50
2.5	phase calibration	52

2.1 Synthetic Aperture Radar basics

SAR is mostly a coherent airborne or space-borne side-looking radar system mounted on a moving platform and offers dramatically high-resolution remote sensing imagery data. SAR emits series of coherent microwave pulses and records the echoes scattered back from the imaged area in its line of sight (LOS), these records form the complex SAR image and named Single Look Complex (SLC) data. SLC image can be seen as a two-dimensional array of complex-valued pixels. Each pixel is the coherent sum of microwave back-scattered within corresponding resolution cell. The complex number at each pixel

presents the amplitude of the back-scattered energy at each scatterers and the phase that is determined by the slant range distance from the pixel location to the radar sensor.

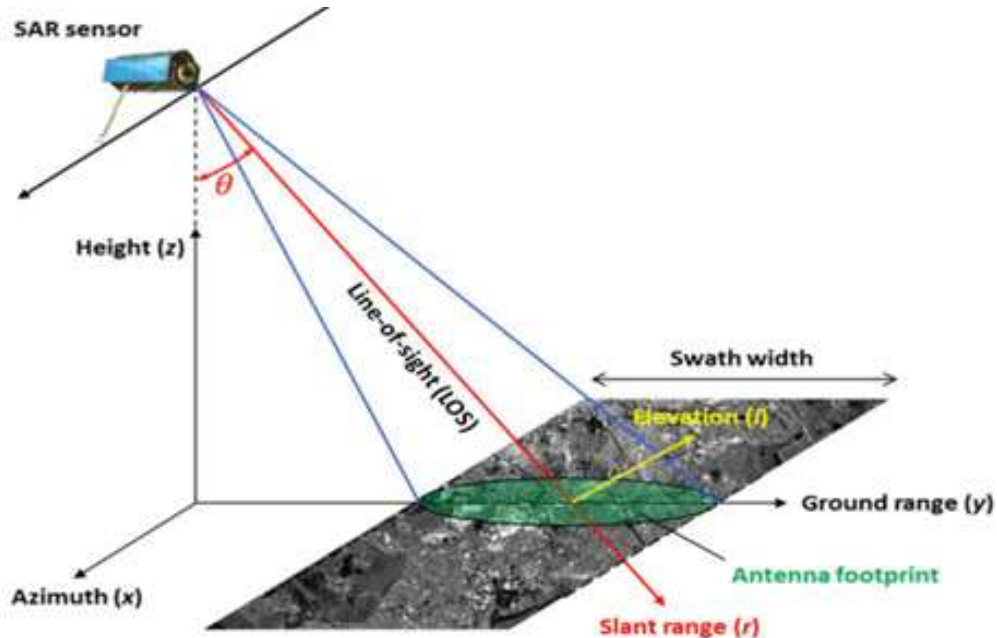


Figure 2.1 – SAR imaging.

SAR has several advantages when compared to optical sensors operating in the visible or infrared bands, these advantages:

(1) SAR system can operate at all times (day, night) and in all weather conditions due to the electromagnetic wave characteristics.

(2) SAR is a coherent system that retains both amplitude and the phase of the back-scattered echoes. Thus the SAR images consist of information about the physical properties and the range of the objects.

(3) SAR uses polarized radiation (Horizontal and vertical polarization), so it can exploit the polarization signature of the imaged scatterers and obtain additional information about the structure of such scatterers.

(4) Modern SAR sensors transmit echoes over large bandwidth (in order of tens/hundreds of MHz), thus leading to fine spatial resolution along the slant range direction.

A cylindrical coordinate system is used to specify the 3D position of scatterers Figure 2.1: (1) The azimuth axis x defines the position of the scatterers along the sensor path. (2) The slant range axis r defines the distance of the scatterers from the SAR sensor. (3) The look angle θ represents the angle between the sensor-to-scatterers line and nadir.

2.1.1 Single look complex data

SAR system collects raw data and compresses them in the range and azimuth directions. The compression of the raw data produces the focused SAR image. The focused SAR image is known as Single Look Complex (SLC) image and can be seen as a two-dimensional array of complex-valued pixels. Each pixel has a complex number, where the amplitude of this complex number presents the coherent sum of the microwave field backscattered by all the scatters (rocks, sands, vegetation, buildings, etc.) within corresponding resolution cells projected on the Earth surface. The phase of the complex number is determined by the slant range distance from the pixel location to the sensor location.

2.1.2 SAR resolution

The resolution of the SAR image is one of the most important characteristics of the SAR system. SAR data pixels are characterized by spatial and temporal resolutions. Spatial resolution is defined as the ability of the SAR system to distinguish between two closely targets. In SAR systems, there are two resolutions, azimuth resolution, and range resolution. Another resolution that should be taken into account when applying a multi-temporal time series analysis of the SAR data is the temporal resolution. It is determined by the revisit time of the SAR sensor at the same imaged area.

2.1.3 Speckle in SAR images

SAR data are subjected to speckle noise which interferes with the sharpness of the images. Speckle noise affects both the amplitude and the phase of radar signals. Speckle noise degrades the quality of the images and therefore affects the performance of their analysis and interpretations.

2.1.4 SAR data characteristics

The main data-sets described hereby are the ones utilized in the dissertation. These data-sets consists of spaceborne and airborne data acquired over different locations. For the TomoSAR study applied over tropical forests, airborne SAR data acquired by different platforms (L-band UAVSAR from JPL/NASA and P-band SETHI from ONERA) are utilized. While, for InSAR analysis, we used sentinel-1 C-band SAR data acquired over Lebanon as a case study.

2.1.5 Sentinel-1 data

The SENTINEL-1 spaceborne mission is the European Radar Observatory for the Copernicus joint initiative of the European Commission (EC) and the European Space Agency (ESA). This Copernicus Program satellite constellation consists of two satellites, Sentinel-1A and Sentinel-1B, respectively launched in 2014 and 2016 [Sentinel, 2013]. Sentinel-1 is an imaging radar that operates at C-band (wavelength range: 3.75-7.50cm). Sentinel-1 mission is designed to provide high-resolution imagery data that cover all global landmasses, coastal zones, and shipping routes. Sentinel-1 sensor operates in four acquisition modes, the configuration parameters and imaging modes of the Sentinel-1 sensor are shown in Table 2.1.

Table 2.1 – Sentinel-1 data configuration.

parameters	IW	WV	SM	EW
Polarisation	Dual(HH+HV, VV+VH)	Single (HH, VV)	Dual(HH+HV, VV+VH)	Dual(HH+HV, VV+VH)
Incidence angles	31 46	23 37	20 47	20 47
Azimuth resolution	< 20 m	<5 m	<5 m	<40 m
Range resolution	< 5 m	<5 m	<5 m	<20 m
Swath	>250 km	vignette 20x20 km	>80 km	>410 km

Data products are available in single-polarization (VV or HH) for wave mode (WV) and

dual-polarization (VV + VH or HH + HV) and single polarization (VV or HH) for Strip Map (SM), Interferometric Wide (IW) and Extra Wide (EW) swath modes.

Each mode produce products at different levels: 1- Level 0 raw data. 2- Level 1 SLC data (with the size of 8GB/image) consists of amplitude and phase data. 3- Level 1 Ground Range Detected (GRD) data with multi look intensity only. 4- Level 2 ocean data for retrieved geophysical parameters of the ocean.

2.1.6 Airborne data

a- JPL/NASA UAVSAR data and ONERA SETHI data

The data-sets acquired over Gabon Lopé National Park consists of seven fully polarimetric Single Look Complex (SLC) data L-band NASA/JPL UAVSAR from AfriSAR data conducted during the AfriSAR campaign in 2016. UAVSAR platform operates at a frequency band 1217.5–1297.5 MHz. The imaged area is about 22 km wide, with incidence angles extending from 25 to 60 degrees. The scanning is performed by the Gulfstream III jet at that flight at an altitude of 12.5 km. The ground range and azimuth resolution of the UAVSAR polarimetric SLC are 1 m and 2.5 m, respectively. The configuration of L-band UAVSAR is shown in Table 2.2. P-band data consists of 13 fully polarimetric SLC data acquired by ONERA over the Lopé in the AfriSAR airborne campaign (July 2015). The data collection is performed using the SETHI SAR system developed by ONERA and onboard a Falcon 20 aircraft. The pixel resolution of the SLC images is 1.54 m in azimuth range and 3 m in slant range. The configuration of P-band SETHI data including acquisition geometry, bandwidth, carrier frequency, and aircraft altitude are shown in Table 2.3.

The tomographic 125 MHz data set considered in the Paracou experimental site consists of six fully polarimetric SLC images at L and P-band acquired on 24 August 2009. All the acquisitions took about 1 h (from 9:00 a.m. to 10:00 a.m.), resulting in almost no temporal decorrelation.

In this thesis, we also used six tracks fully polarimetric images acquired during the TropiSAR campaign over Paracou.

Table 2.2 – L-band UAVSAR acquisition parameters.

Acquisition Parameters	
Acquisition Mode	PolSAR
Look Direction	Left looking
Pulse duration	40 (μ s)
Steering Angle	90 (deg)
Bandwidth	80 (MHz)
Ping-Pong or Single Antenna Transmit	Ping-Pong
Air craft speed	224 (m/s)
Range of look angle	21–65 (deg)
Antenna Length	1.5 (m)

Table 2.3 – Description of the SETHI system configuration of P-band acquisition parameters. The superscript * indicates the parameters that are identical between the SETHI and F-SAR systems.

Acquisition Parameters	
Acquisition Mode *	PolSAR
Look Direction	Left looking
Effective Pulse Repition Frequency (PRF)	1250 (Hz)
Steering Angle	90 (deg)
Frequency range */Bandwidth	50 (MHz)
Pulse duration	30 (μ s)
Transmitted power	500 (W)
Aircraft speed	100–150 (m/s)
Flight ground altitude	6096 (m)

b- Lidar data-sets

The Lidar data-sets used in this thesis consists of discrete Lidar Small Footprint Lidar (SFL) data and LVIS Lidar waveform. The first data set which we will refer to as the SFL data set was acquired by Sassan Saatchi's team (JPL) in July 2015 with a variable point density and footprint diameter of about 10 cm. i) Digital Terrain Model (DTM), ii) Canopy Height Model (CHM) and other canopy metrics derived from CHM are derived from SFL data. Based on the DTM, slope maps were estimated, the heights of the Lidar point were normalized by removing the ground elevation. The DTM and CHM data were developed in a

raster format at 1m posting characterizing the forests structure of an area of approximately 15 km² of old-growth and successive forests, as well as savanna vegetation of the northern Lopé study site. The second Lidar data set was acquired by NASA's airborne Land Vegetation Ice Sensor (LVIS) during March 2016 as a part of the NASA-ESA collaboration of the BIOMASS, GEDI and NISAR calibration and validation activities. LVIS is a Large Footprint Lidar (LFL) with full-waveform capability with applications of measuring ground elevation and vertical profile of vegetation structure in various ecosystems (data can be downloaded from https://lvis.gsfc.nasa.gov/Data/Data_Download.html).

2.1.7 SAR applications

SAR has been a significant tool for a wide variety of landscape applications in a broad sense (natural habitats, rural areas, forests, natural hazards, urbanization). SAR data being collected over 2-D synthetic aperture can be processed using signal processing algorithms to focus the illuminated scatters in the 3-D space. In particular, the high temporal frequency of the radar acquisitions that are currently being achieved is considered as a beginning of a new stage for the application of the SAR techniques such as Interferometry SAR (InSAR), Polarimetry SAR (PolSAR), and Tomography SAR (TomoSAR). Polarimetric SAR is an advanced imaging radar system, it plays an important role in radar remote sensing. Full polarimetry radar provides five datasets, HH, HV, VH, VV, and total power (TP). With full SAR polarimetry, it is possible to obtain much more information than conventional SAR systems (i.e. single polarized SAR system), fully polarimetric mode provides more information about the physical structure of the imaged area. Nowadays polarimetric SAR has much application including agriculture (crop classification, soil moisture extraction), oceanography (surface currents and wind field retrieval), forestry (forest monitoring, classification, and tree height estimation), and military (ship detection, target recognition/classification) [Boerner]. InSAR has been successfully used to infer the information about earth's surface, including sectors such as topographic mapping, seismology [Massonnet et al., 1993; Peltzer and Rosen, 1995], volcanology [Massonnet and Sigmundsson, 2000], detecting ground subsidence and deformations [Amelung et al., 1999]. Such a technique exploits the information contained in the radar phase of at least two complex SAR

images acquired at different times over the same area to be used in the formation of an interferometric pair. TomoSAR is Multibaseline (MB) SAR technique that provides vertical resolution capabilities. This technique was repeatedly demonstrated using airborne data [Reigber and Moreira, 2000; d'Alessandro and Tebaldini, 2012].

2.2 Interferometry SAR

Differential InSAR (DInSAR) is a new radar remote sensing technique that exploits the geometric properties of the SAR image phase to and measures the elevation and the deformation of the scatterers. InSAR uses short wavelengths to monitor surface displacements with millimetric accuracy. InSAR technique suited for monitoring long term dynamic processes such as volcanoes, crustal dynamics, and land subsidence. The rationale of InSAR is to subtract the phases of two SAR images taken from two nearby locations in the same area. The distance between the two locations is named the baseline. The phases subtraction is done by the multiplication of the complex SAR image named master with the complex conjugate of the second image named slave to generate the interferogram. The interferometric phase obtained contains information about the phase of the deformation in the earth's surface (if it is found), topographic phase, and phase noise due to different aspects such as atmospheric effects or noise in the system.

The interferogram phase between two acquisitions N and M can be written as:

$$\phi_{\text{int}} = \phi_{\text{Dis}} + \phi_{\text{topographic}} + \phi_{\text{Atm}_N} - \phi_{\text{Atm}_M} + \phi_{\text{orbital}_N} - \phi_{\text{orbital}_M} + \phi_{\text{Noise}} + 2.k.\pi \quad (2.1)$$

ϕ_{Dis} is the deformation phase, $\phi_{\text{topographic}}$ is the residual topographic phase, ϕ_{Noise} is the phase noise due to temporal decorrelation, mis-coregistration, uncompensated spectral shift decorrelation, orbital errors, and thermal noise. ϕ_{Atm_N} and ϕ_{Atm_M} is the atmospheric phase screen at different passes due to the propagation delay of the signal in the atmosphere. Here, it is necessary to mention the limitations and difficulties that face the extraction of the deformation phase from the interferogram phase. These limitations

are: the temporal and geometric decorrelation that effect the ϕ_{Noise} term [Hanssen et al., 2001], the phase unwrapping problem that lead to estimate the phase cycles [Ghiglia and Pritt, 1998], and the atmospheric phase term [Zebker et al., 1997].

2.3 Permanent scatterer interferometry

InSAR results accuracy is strongly affected by the atmospheric disturbances and phase noise, thus a proposition was found to use Permanent scatterers (PS) and distributed scatterers (DS) starting from long temporal series of interferometric SAR images. Permanent Scatterers Interferometry (PSI) is an advanced type of DInSAR based on large number of stacked SAR images that make it able to estimate the deformation time series, the average displacement rate, and the RTE. Different PSI techniques were proposed in the last years, the first PSI technique was developed by [Ferretti et al., 2001] for long-term deformation monitoring, especially in urban environments. After that, similar approaches have been proposed by different scientists [Adam et al., 2003; Hooper et al., 2004; Meyer et al., 2006]. Different PSI techniques are followed by this approach, the small baseline subset SBAS technique which is one of the most important and documented technique [Berardino et al., 2002; Lanari et al., 2004; Pepe and Lanari, 2006; Pepe et al., 2011]. A similar approach was proposed by [Mora et al., 2003]. Another approach was done based on step-wise linear functions for deformation estimates are described in [Crosetto et al., 2008; Werner et al., 2003]. Recently a new algorithm SqueezeSAR is proposed to jointly process PS and DS taking into account their different statistical behavior. SqueeSAR is proposed by [Ferretti et al., 2011]. More relevant contributions are: 1. Adapting LAMBDA method used in GPS to the PSI parameter estimation [Kampes and Hanssen, 2004]. 2. Use of different adaptive deformation model in PSI [Van Leijen and Hanssen, 2007]. 3. Methods to derive different characteristics of PS and to classify them especially in urban areas [Perissin and Ferretti, 2007].

All the mentioned PSI techniques differ either in method choosing the PS candidate or in the deformation model used in the PSI estimation. Since the PSI needs to retrieve the coordinates of single points, the imaging in 3D is done by tomography, estimating the

reflectivity in elevation is derived. In urban areas, the multiple scatterers must be considered in the tomographic 3D reconstruction and model selection must be applied in the estimation of the relevant scatterers. The first experiment on SAR tomography was carried out in the laboratory, under ideal experimental conditions, and by using airborne systems [Reigber and Moreira, 2000]. Another SAR tomography method is advanced imaging in the 4D (space-time SAR imaging) enhancing another than the separation of the point scatterers in the same azimuth-range resolution cell, it estimates their relative deformation also [Fornaro and Serafino, 2006]. The SAR tomography is a spectrum estimation problem along with a specific resolution cell, the complex SAR image is the sampled Fourier transform of the reflectivity function in the elevation direction. There are many different spectrum estimation strategies are used, such as singular value decomposition (SVD) and nonlinear least square (NLS). Thus SAR tomography is a young method to determine the 3D reflectivity function, depending on multi pass acquisitions, and is discussed in different publications [Fornaro et al., 2006; Reigber and Moreira, 2000].

2.4 Tomography SAR background

TomoSAR implementation requires an accurate approach regarding the relative phase difference between different passes. The rationale of tomography is to employ multiple flight tracks nearly parallel to each other [Ho Tong Minh et al., 2016] as shown in the left panel of Fig.3.2. The ensemble of all flight lines allows us to form a 2D synthetic aperture, resulting from the coherent multiple SLC images of different passes, providing a possibility to focus the signal in the whole 3D space. By exploiting tomography, MB SAR data can be converted into a new multi-layer SAR data stack where each layer represents scattering contributions associated with a certain height [Ho Tong Minh et al., 2016]. We will refer to (x,y,z) as the azimuth, ground range, and height, respectively. Let's consider an MB data-set of SLC images acquired by N sensors parallel track, and let $SLC_n(y,z)$ denote the SLC

value at the pixel with slant range and azimuth range (y, z) in the n -th image. The following model holds [Tebaldini et al., 2016]:

$$\text{SLC}_n(y, z) = \iint S(y, z) \exp(j \frac{4\pi}{\lambda} R_n) dy dz \quad (2.2)$$

where: R_n is the distance from the sensor to the scatterer. $S(y, z)$ is the scene complex reflectivity within SAR resolution cell, λ is the carrier wavelength. The expression of topography-compensated SLC data can be conveniently approximated as:

$$\text{SLC}_n(r, \xi)^{\text{tc}} = \int P(\xi) \exp(j K_n \xi) d\xi \quad (2.3)$$

where: $P(\xi)$ denotes the projection of target reflectivity along cross-range axis, ξ , (r, ξ) denote the slant-range and cross-range coordinates, b_n is the normal InSAR baseline with respect to the master track. k_n is the wave-number associated with the cross-range direction.

$$K_n = \frac{4\pi}{\lambda R} b_n \quad (2.4)$$

An essential demand for both Tomography and Interferometry SAR is that SLC data stack is not affected by phase terms other than those associated with the spatial distribution of targets [Tebaldini and Guarnieri, 2010]. Indeed, any phase disturbances will affect the TomoSAR and InSAR products by affecting the coherence phase of the interferometric phase. There are different sources of phase screens such as Ionosphere, Troposphere, orbit inaccuracy [Ferreti et al., 2000], antenna phase center stability and clock phase stability [Massonnet et al., 1995]. while Ionosphere and troposphere affect space-borne SAR data, orbit inaccuracy is a common issue that affects both airborne and space-borne SAR systems and can appear as phase screens in the SLC data stack. Actually, phase disturbance arises in SAR images as a result of undesirable variation of the optical path from sensor to target. In particular, uncompensated phase terms due to either unpredicted geometrical factors (orbit uncertainty) or propagation through troposphere and ionosphere results in

blurring and side lobes phenomena [Tebaldini and Guarnieri, 2010]. Phase screens need to be estimated and corrected for during the data processing in order to improve MB SAR data quality and enhance the interpretation of TomoSAR and InSAR applications. In the following, a detailed discussion of different phase calibration approaches was done.

2.5 phase calibration

Before carrying on MB SAR algorithms, a fundamental issue should be taken into account is the phase calibration of the SAR data, in order to compensate the phase residuals that influence the focusing MB SAR SLC data stack. These phase disturbances originated from atmospheric propagation delays or an error in allocating the platform position [Tebaldini et al., 2016]. In order to eliminate these residuals, iterative phase calibration algorithm which is capable of estimating the phase screens and correct the data stack can be applied. For this issue, Various phase calibration techniques were proposed. Some techniques are based on the Permanent Scatterers (PS) in which the calibration performance could be defective by the nature of the scatterers having important limitations when applied to the tropical forests due to decorrelation that is caused by dense vegetation [Tebaldini and Rocca, 2009]. Another approaches proposed the separation of the ground contribution and volume contribution in order to isolate the ground phase using Sum Kronecker Product (SKP) structure in presenting the data covariance matrix [Tebaldini, 2009b] based on Multi-polarimetric Multibaseline (MPMB) SAR data. One more technique proposed phase calibration of MB data by distributed targets using MB estimation techniques, such as Phase Linking [Guarnieri and Tebaldini, 2008], SqueeSAR [Ferretti et al., 2011]. Tebaldini et al [Tebaldini et al., 2016] proposed a recent strategy for calibrating the airborne data-set using Distributed Scatterers Interferometry DS-InSAR based on the double localization of target position and sensor position errors responsible for the phase disturbances in the data stack. Where it was shown that phase screens can be accurately retrieved based on volumetric targets like forests and ice, even in the absence of prior information about the scene topography or reference targets.

We want to focus on the phase calibration methods proposed to handle the effect of

phase disturbance that affect the performance of Multi-baseline SAR algorithms. These algorithms applied successfully to airborne SAR data.

2.5.1 Phase Calibration algorithms

In this section, the main phase calibration algorithms proposed in the literature are discussed. Three of the most important phase calibration approaches are then described.

2.5.2 Phase Calibration by Permanent Scatterer Interferometry (PS-InSAR)

Accurate retrieval of ground motions can be established by the founded approach Permanent Scatterers Interferometry through assaying of SAR data stacks [Ferreti et al., 2000]. This approach utilizes the existence of a set of point targets within the illuminated scene, which are stable enough to allow for precise phase measurements. Point Selection is executed by considering only those targets that show stable amplitude in all images in the data-stack, thus the name Permanent Scatterers (PSs).

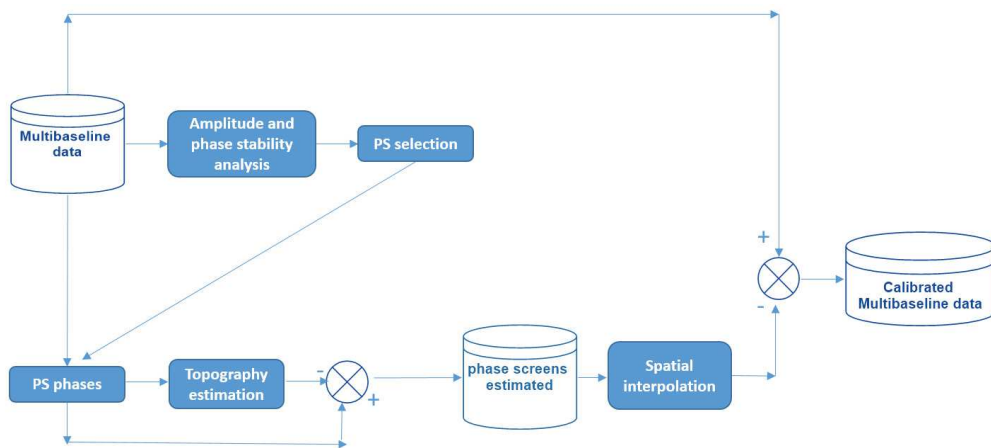


Figure 2.2 – Phase calibration of MB SAR data using PS-InSAR approach .

As in the more general case of multi-pass InSAR, the differentiating of phase contributions related to motions from those resulting from atmospheric propagation (phase

screens) is the most substantial theme in PS-InSAR. Part of the atmospheric signal can be eliminated using auxiliary data from meteorological models [Pichelli et al., 2015]. However, the precision of the mentioned methods are inadequate in most cases and a data-based technique is essential. Data-based techniques for calculating and removing the atmospheric signal are dependent on its statistical characteristics, principally its spatial correlation length. According to such characteristics, the atmospheric signal is evaluated at points where earlier suppositions can be made (i.e. linear motion or absence of motion) and then added to reassemble the atmospheric phase screen at each point of the image stack [Ferreti et al., 2000].

In the case of PS-InSAR used for phase calibration of a forest scenario presented in [Tebaldini, 2009b], double bounce interactions of tree trunks and branches with the ground were found to work as PSs. As the phase center of double bounce echoes is ground locked, the extraction of DTM and phase screens elimination is possible. It has to be mentioned that the two factors that empowered the application of PS-InSAR are the flat ground topography and the existence of a relatively sparse and managed forest site. As an example, the additional interpretation of the BIOSAR 2008 data-set (Northern Sweden) showed an obvious reliance between PS density and terrain slope. The different steps of phase calibration by PS-InSAR is shown in Figure 2.2.

Double-bounce interactions were also recognized in tropical areas using data from TropiSAR. Results are stated in [d'Alessandro et al., 2013], together with a precise study of the dependence of double bounce on terrain slope. In the mentioned study, however, double bounces were recognized based on tomographic data cubes, as their signature was not as obvious as in SLC data. A long term investigation of the effectiveness of PSInSAR in the forest is absent nowadays. Nevertheless, it is predicted that the mentioned method will be accurate in many forest sites due to the combination of different aspects like variation of moisture, terrain slope, and forest density.

2.5.3 Phase Calibration by Algebraic Synthesis (AS)

The Algebraic Synthesis (AS) technique is an algebraic procedure to decompose ground and volume scattering based on multi-baseline and multi-polarimetric data [Tebaldini, 2009b]. The AS method is displayed to broaden the idea of PolInSAR to the case of multiple baselines, and it defaults to PolInSAR in the case where only two polarimetric acquisitions are available [Tebaldini, 2009b]. In the case of phase calibration, utilization of the AS technique followed by multi-baseline phase estimation allows the derivation of the phase of ground scattering contributions. The restored phases correspond to the sum of the topographic phase and the residual phase screens, and thus they resemble the phase offsets. The different steps of phase calibration by AS is shown in Figure 2.3.

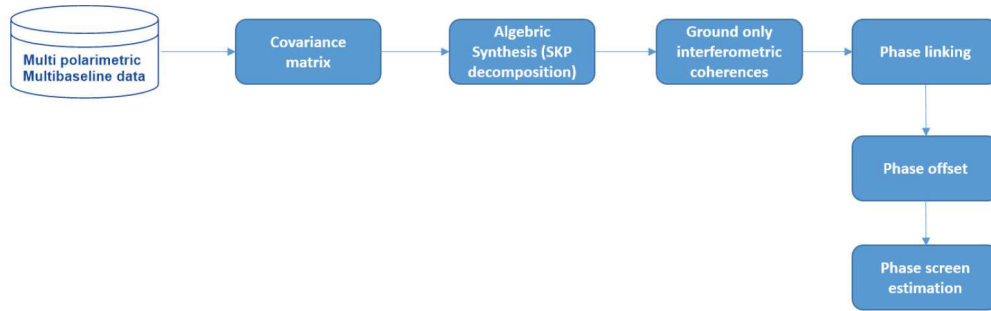


Figure 2.3 – Phase calibration of MB SAR data using AS approach .

An appealing characteristic of this technique is that relative phase calibration is automatically acquired by counter-rotating the data for the obtained phase offsets, without the need to particularly separate phase screens from the topographic phase. Nevertheless, a further InSAR analysis is essential to evaluate terrain topography.

This approach was realized and validated at P-Band based on campaign data from BioSAR, BioSAR 2, and TropiSAR [Tebaldini and Rocca, 2009], [Tebaldini and Rocca, 2012b], [Gatti et al., 2011], [Ho Tong Minh et al., 2014].

The TomoSAR data phase calibration using the AS approach is done by eliminating the ground phase contributions from the tomographic Single Look Complex (SLC) data. The exploitation of MultiPolarimetric and MultiBaseline (MPMB) data allows the identification

of different Scatterer Mechanisms (SM) [Tebaldini and Rocca, 2012b]. The separation of the ground contribution and the vegetation from MPMB data is performed by presenting the data covariance matrix through SKP [Tebaldini, 2009b].

The structure model of the data covariance matrix, where each scatterer mechanism is presented by Kronecker Product (KP) of two matrices, can be addressed as follows:

$$\begin{aligned} W &= E[YY^H] \\ &= \sum_{k=1}^K \lambda_k C_k \otimes R_k \approx C_g \otimes R_g + C_v \otimes R_v \end{aligned} \quad (2.5)$$

Where Y is the MPMB SLC data vector, H is the Hermitian conjugate, W denotes the data covariance matrix, K is the total number of SMs that contribute to SAR signal, $C_{g,v}$ and $R_{g,v}$ are the polarimetric signature and structure matrix corresponding to the ground and volume contribution, respectively.

Phase calibration solution:

- 1- Retrieve an initial guess for ground phases by Capon spectra for the HH channel.
- 2- Correct the original data using this ground phase.
- 3- Re-retrieve the ground phases by Sum of Kronecker Products (SKP) model.

initialize ground phases:

$$\phi_n^{\text{initial}} = \frac{4\pi}{\lambda r \sin \theta} B_n z_g^0 \quad (2.6)$$

where:

$$z_g^0 = \text{argmax} S_{\text{capon}}(z, \text{HH}) \quad (2.7)$$

Assuming two main Scattering Mechanisms - ground and volume scattering :

- 1-The best LS approximation of W is obtained by retaining the first 2 terms of the SKP Decomposition.

2- The matrices R_g , R_v , C_g , C_v can be determined from the terms of the SKPD via a linear transformation.

Retrieval of ground phases:

$$\phi_n^{\text{ground}} = \frac{4\pi}{\lambda r \sin \theta} B_n z_g + \eta_n \quad (2.8)$$

$$\phi_n^{\text{ground}} = \text{PL}(R_g) + \phi^{\text{initial}} \quad (2.9)$$

After the estimation of the ground covariance matrix, the Phase linking algorithm is applied to estimate ground phases. After that, the calibration is carried out by removing ground phases from the original SLC data. Finally, Capon beamforming power estimation is applied to get the tomographic profiles.

2.5.4 Phase Calibration by Distributed Targets (DS-InSAR)

Multi-pass InSAR using distributed scatterers, which will be mentioned as DS-InSAR, is enabled by multi-baseline estimation methods, such as Phase Linking [Guarnieri and Tebaldini, 2008], SqueeSAR [Ferretti et al., 2011], and SBAS [Berardino et al., 2002]. A common feature of these methods is the ability to mutually process a number of different image pairs, or even all available image pairs. It is completed to rebuild the phase, or instead of the related optical path, of decorrelated interferograms since direct phase estimation is not viable. A theory that implements the lower bound of the precision obtainable by these methods is found in [Guarnieri and Tebaldini, 2007].

DS-InSAR is based on the analysis of multi-looked interferograms. This results in a resolution loss with respect to PS-InSAR, in exchange for the possibility to analyze areas where PS density is not enough. The different steps of phase calibration by DS is shown in Figure 2.4.

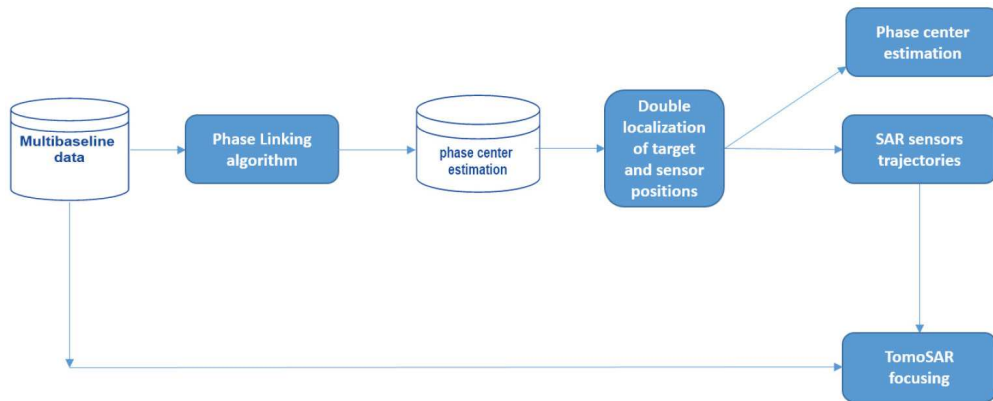


Figure 2.4 – Phase calibration of MB SAR data using DS approach .

Phase calibration of airborne data-sets using DS-InSAR was lately illustrated in [Tebaldini et al., 2016], where it was shown that phase screens can be precisely estimated depending on volumetric targets like forests and ice, even in the absence of prior information about the scene topography or reference targets. The key ideas of that work are: i) multi-baseline phase estimation favors illustrating volumetric targets as equivalent phase centers, ii) multi-baseline data provide enough equations to simultaneously assess aircraft positions and target phase center height. These approaches were then utilized to calibrate campaign data acquired over ice (AlpTomoSAR), and boreal (BioSAR 2008) and tropical (TropiSAR) forests, developing more precise tomographic products in all three cases.

It is significant to mention that the approach used in [Tebaldini et al., 2016] is adjusted to the case of airborne data, for which phase screens are the outcome of uncompensated platform motion. Similar methods could in principle be prolonged to evaluate phase screens originating from mechanical oscillations, which can be logically parameterized, and possibly clock errors.

Part II

Tomography SAR for forested areas

L-band UAVSAR tomographic imaging in dense forests, Gabon forests

Contents

3.1	Introduction	61
3.2	Materials and Methods	64
3.3	Results	75
3.4	Discussion	78
3.5	Conclusion	82

3.1 Introduction

Tropical forests have major impacts on earth ecosystem in terms of carbon storage, regulating water and weather. Above Ground Biomass (AGB) is the most important parameter that is related directly to the amount of carbon in the global ecosystem cycle [Pan et al., 2011]. Uncertainty in balancing the global carbon budget arises from a deficiency in AGB density estimation and carbon stocks in tropical forests. Indeed, developing new technologies is critical in surveying and monitoring tropical forests. NASA, ESA, AGEOS, and DLR have developed united efforts in the implementation of the AfriSAR campaign on the Gabon forests [Lou et al., 2017]. In this context, the objective of AfriSAR campaign

was to acquire airborne and field data for the development, calibration, and validation of the vertical structure of tropical forests and biomass estimation algorithms. The airborne data provided by the campaign consists of polarimetric Synthetic Aperture Radar (SAR) interferometry (Pol-InSAR), Tomography SAR (TomoSAR) datasets, Lidar full waveforms and small footprint Lidar (SFL).

SAR and Lidar provide records sensitive to 3D forests structure parameters at high spatial resolution [Drake et al., 2002; Dubayah et al., 2010; Cazcarra-Bes et al., 2017b]. Lidar sensors emit a laser beam which is reflected by forest structure elements within the laser path, and the returned waveform is recorded by the Lidar system [Lefsky et al., 2002]. Metrics extracted from Lidar waveforms are used to estimate forests vertical structure. Concerning SAR, the development of approaches for the estimation of forests structure has been enhanced by the introduction of Pol-InSAR [Papathanassiou and Cloude, 2001] and TomoSAR [Reigber, 2000]. SAR is mostly a coherent airborne or space-borne side-looking radar system that utilizes the flight path of the moving platform and offers a high-resolution remote sensing imagery data. SAR has been a significant tool for a wide variety of landscape applications in a broad sense (e.g. natural habitats, rural areas, forests, natural hazards, urbanization) [Kramer, 2002]. SAR data collected over 2-D synthetic aperture can be processed using signal processing algorithms to focus the illuminated scatters in the 3D space. Polarimetric SAR is an advanced imaging radar system [Zebker and Van Zyl, 1991], it plays an important role in radar remote sensing. Full polarimetry radar provides five datasets from each polarization band, namely HH, HV (H: horizontal, V: vertical), VH, VV, and total power (TP). With a polarimetric SAR, we can obtain much more information than a single polarized SAR system. Now polarimetric SAR has many applications including agriculture (crop classification, soil moisture extraction) [Ferrazzoli et al., 1997; Ballester-Berman et al., 2005; Hoekman et al., 2011; Baghdadi et al., 2012], oceanography (surface currents and wind field retrieval) [Schmullius and Evans, 1997], forestry (forest monitoring, classification, and tree height estimation) [Cloude and Papathanassiou, 1998; Freeman, 2007], and military (ship detection, target recognition/classification) [Boerner; Liu et al., 2005].

TomoSAR is a Multibaseline (MB) SAR technique which provides vertical resolution capabilities [Reigber, 2000; d'Alessandro and Tebaldini, 2012]. This technique has been repeatedly demonstrated using airborne data [Reigber, 2000]. The potential of TomoSAR arises from its capability to identify the forests top height, which is an essential parameter for the AGB estimation [Ho Tong Minh, D et al., 2017; Ho Tong Minh, Dinh et al., 2014]. Forests height estimation has been demonstrated using Pol-InSAR model inversion over different forests (boreal, temperate, and tropical) at multiple frequencies varying from P-up to X-band using airborne and spaceborne platforms [Kugler et al., 2015]. Also, forests 3D reconstruction by TomoSAR techniques today is well-established and has been demonstrated in various experiments over different forests ecosystems [Ho Tong Minh, D et al., 2017; Ho Tong Minh, Dinh et al., 2014, 2015a]. The ability of P-band TomoSAR for characterizing 3D vertical structure of tropical forests has been discussed and evaluated previously [Ho Tong Minh et al., 2016], while L-band TomoSAR capabilities are still in a rather early stage of development. Using airborne data acquired during TropiSAR campaign, D.H.T Minh et al. [Ho Tong Minh, Dinh et al., 2015b] demonstrated that the use of tomographic imaging at L-band in tropical forests appears limited. The TropiSAR campaign carried out in 2009 in French Guiana offered the first opportunity to test TomoSAR for tropical forest areas. However, these data were suboptimal for assessing multi-frequency TomoSAR performance for forest structure monitoring. To overcome this limitation, the AfriSAR campaign was successfully carried out in 2015 and 2016, it has acquired an optimal tomographic and polarimetric data over dense forests on Gabon.

The aim of the chapter is to analyze the capability of L-band TomoSAR to retrieve tropical forests 3D structure and estimate accurately forests top height in dense forests. First, we validate L-band vertical profile with Digital Terrain Model (DTM) and Canopy Height Model (CHM) from SFL data set as a reference. Second, qualitative comparison of Capon beam forming profile of L-band at HH and HV polarizations with LVIS Level 1B waveform Lidar data were carried out over different regions of interest in the Gabon Lopé National Park. In addition forests top height has been retrieved from the TomoSAR L-band data. The results suggest that L-band TomoSAR holds promise for mapping forest structure in tropical forests.

3.2 Materials and Methods

3.2.1 Study area

The NASA-sponsored AfriSAR campaign has been carried out over the tropical forests of Gabon in Africa. This campaign has performed L-band UAVSAR acquisitions (in February 2016). The campaign was conducted in collaboration with an ESA-sponsored campaign [Lavalle et al., 2017]. UAVSAR and Lidar systems have flown over the same sites where ESA platforms have acquired data. We will focus on the presentation of Lopé in which our tomographic study was conducted (Fig. 3.1). Lopé National Park is one of the largest national

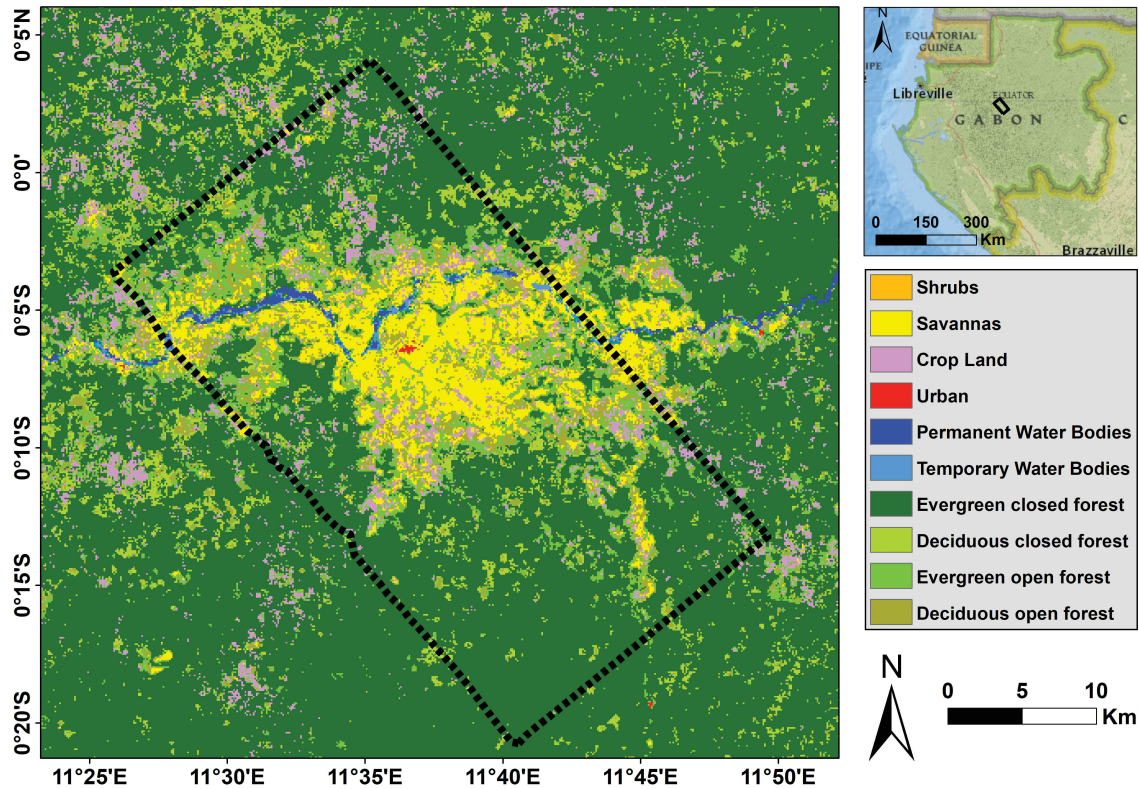


Figure 3.1 – Study area, Gabon Lopé Park. The black polygon represents where UAVSAR acquired L-band TomoSAR data. The background is derived from the Africa Copernicus Land Cover of 100 m x 100 m spatial resolution [Tsendbazar et al., 2018]. The land cover shows different vegetation features of the Lopé National Park.

Table 3.1 – Region of interests at Lopé Park.

Campaign	Type	CHM (m) [min, median, max]	Number of pixels
COL1	Colonizing forests (Intermediate)	[6.9, 29.5, 43.1]	6166
OKO1	Okoumé forests	[3.7, 33.8, 44.3]	9839
OKO2	Okoumé forests	[26, 31.7, 40.1]	10421

parks in central Gabon covering an area of 4913 km². Although the terrain is mostly rain forests, the scene in the northern part is composed of the last remnants of grass savanna created in central Africa during the ice age 15000 years ago. The park was the first protected area in Gabon. It is frequently tracked by the National Park Agency of Gabon which makes it well cited as a perfect scientific research site (Fig. 3.1). This landscape consists of vast Savanna areas in the north, bounded by the Ogooué River and often burned to preserve the forests Savanna areas, in addition to an expanded region of compact tropical forests with patches of successive forests with complex structure, which are advanced through time with savanna recolonization [White, 2001]. Lopé is a convenient landscape for showing the effective performance of UAVSAR for tomographic imaging due to the gradient of forests biomass from the forests savanna boundary (up to 100 Mg/ha) to compact undisturbed humid tropical forests (greater than 400 Mg/ha). Tree height and vertical structure can also vary gradually from Savanna through forests, providing mono-dominant uniform trees of Okoumé (30-50 m tall) to regions with dense Marantaceae understory, and large gaps in mid canopy, creating skewed vertical profiles. The topography of Lopé is also diverse, varying between large flat plains and steep slopping terrains. To achieve qualitative analysis between UAVSAR-TomoSAR vertical profile and Lidar waveforms, three Region of Interests (ROIs) were selected. These regions include: two ROIs in the Okoumé dominated forests (OKO1 and OKO2), and one ROI in colonizing forests (COL1) (Table 4.1).

3.2.2 Data-sets

Different data sets have been acquired over the Lopé during the AfriSAR campaign. The NASA AfriSAR campaign involved three data sets, UAVSAR data, LVIS Lidar data and SFL data.

Radar acquisitions configuration

The AfriSAR campaign aims to provide support to forthcoming NISAR, GEDI and BIOMASS missions. Using UAVSAR and the LVIS waveform Lidar instruments, NASA acquired 39.6 and 32.4 of flight hours of data, respectively over various sites in Gabon for the sake of calibration, verification, and new algorithm exposition of several ecosystem science products. The operating band of the UAVSAR radar instrument is 1217.5-1297.5 MHz (L-band), (data can be downloaded from <https://uavsar.jpl.nasa.gov/cgi-bin/data.pl>), which exploits an electronically scanned array antenna to allow a robust repeat-pass interferometric measurements [Hensley et al., 2008]. The Gulfstream III jet, with an acceptable flight altitude of 12.5 km, allows the scanning of about a 22 km wide area, with incidence angles extending from 25 degree to 60 degree. A typical UAVSAR polarimetric single-look-complex (SLC) product has ground range and azimuth resolution of 2.5 m and 1.0 m, respectively [Fore et al., 2015]. In the following, we show the tomographic imaging over the northern part of the Lopé National Park in Central Gabon using 7 PolInSAR single-look-complex images collected by UAVSAR. The total area covered by the image is 22 km x 50 km, but a part of approximately 1 km x 5 km is considered for our study. UAVSAR dataset acquired over Lopé is fully polarimetric and has been gathered by increasing the aircraft altitude by 20 m each flight track, leading to significantly low variation of vertical resolution from near range to far range. (we present the acquisition parameters of UAVSAR configuration in Table 4.2, also baseline configuration of the acquisitions is shown in Table 3.3).

Lidar data-sets

Using different instruments, two Lidar data sets have been collected over the area of Lopé. The first data set which we will refer to as the SFL data set was acquired by Sassan Saatchi's team (JPL) in July 2015 with a variable point density and footprint diameter of about 10 cm. The data sets were pre-refined to eliminate any artefacts of helicopter motions in order to present a more uniform point density of about 10 points per m² for vegetation characterization. i) DTM, ii) CHM and other canopy metrics derived from CHM are derived from SFL data. Based on the DTM, slope maps were estimated, the heights of

Table 3.2 – L-band UAVSAR acquisition parameters.

Acquisition Parameters	
Acquisition Mode	PolSAR
Look Direction	Left looking
Pulse Length	40 (μ s)
Steering Angle	90 (deg)
Bandwidth	80 (MHz)
Ping-Pong or Single Antenna Transmit	Ping-Pong
Air craft speed	224 (m/s)
Range of look angle	21-65 (deg)
Antenna Length	1.5 (m)

Table 3.3 – Baseline configuration of Multi-baseline UAVSAR acquisitions.

Track	Relative baseline
1	master
2	20m
3	40m
4	60m
5	80m
6	100m
7	120m

the Lidar point were normalized by removing the ground elevation. The DTM and CHM data were developed in a raster format at 1m posting characterizing the forests structure of an area of approximately 15 km² of old growth and successive forests, as well as savanna vegetation of the northern Lopé study site. The second Lidar data set was acquired by NASA's airborne Land Vegetation Ice Sensor (LVIS) during March 2016 as a part of the NASA-ESA collaboration of the BIOMASS, GEDI and NISAR calibration and validation activities. LVIS is a Large Footprint Lidar (LFL) with full-waveform capability with applica-

tions of measuring ground elevation and vertical profile of vegetation structure in various ecosystems. For LVIS, there are two different datasets available: Level 1B and Level 2 (data can be downloaded from https://lvis.gsfc.nasa.gov/Data/Data_Download.html). The level indicates the amount of processing, which the data has undergone before it was published. Level 1B data contains georeferenced Lidar returned waveforms. Level 2 data contains georeferencing information for different reflecting surfaces within the laser footprint and the locations of which have been derived from the Level 1B waveform.

3.2.3 TomoSAR background

TomoSAR implementation requires an accurate handling regarding the relative phase difference between different passes. The rationale of TomoSAR is to employ multiple flight tracks nearly parallel to each other [Ho Tong Minh et al., 2016] as shown in the left panel of Fig. 3.2. The ensemble of all flight lines allows forming a 2D synthetic aperture, resulting from the coherent multiple Single Look Complex (SLC) images of different passes, providing a possibility to focus the signal in the whole 3D space. By exploiting tomography, SAR data can be converted into a new multi-layer SAR data stack where each layer represents scattering contributions associated with a certain height as shown in the right panel of Fig. 3.2 [Ho Tong Minh et al., 2016]. We will refer to (r, x, ξ) as the Slant, azimuth and cross ranges, respectively. We consider a data-set of SLC images acquired by N sensors parallel track, and let $Y_n(r, x, \xi)$ denote the SLC value within pixel resolution cell (r, x, ξ) in the n -th image. The expression of topography-compensated (tc) SLC data can be approximated [Tebaldini et al., 2016] as:

$$Y_n(r, x)^{tc} = \int P(r, x, \xi) \exp(j \frac{4\pi}{\lambda r} b n \xi) d\xi \quad (3.1)$$

where: $P(r, x, \xi)$ denotes the projection of target reflectivity along cross-range axis ξ , ξ represents the cross-range coordinate, orthogonal to the radar Line-of-sight (LOS) that's

defined by the slant range coordinate r . We can define k_n , which is the wavenumber associated with the cross-range direction.

$$K_n = \frac{4\pi}{\lambda R} b_n \quad (3.2)$$

where R is the distance from the sensor to the scatterer, λ is the carrier wavelength, and b_n is the normal InSAR baseline with respect to the master track.

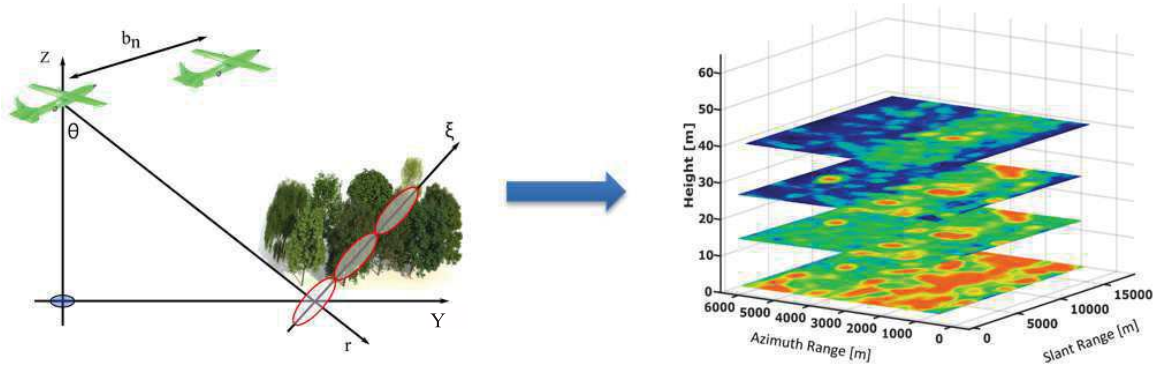


Figure 3.2 – Left, Schematic representation of the TomoSAR acquisition. Azimuth axis is orthogonal to the picture. Right, schematic view of TomoSAR imaging, where each layer represent scattering contributions associated with certain height.

3.2.4 TomoSAR Phase Calibration

Prior to MB SAR algorithms, a fundamental issue should be taken into account, which is the phase calibration of the TomoSAR data, in order to compensate the phase residuals that influence the focusing of MB SAR data. These phase disturbances are originated from atmospheric propagation delays or an error in allocating the platform position. To overcome this issue, we adopted UAVSAR data to phase calibration using algebraic synthesis (AS) approach. This technique is an algebraic procedure to decompose ground and volume scattering based on multi-baseline and multi-polarimetric data [Tebaldini, 2009a]. This approach was already realized and validated at P-Band based on campaign data from BioSAR, BioSAR 2, and TropiSAR, see [Ho Tong Minh, Dinh et al., 2014; Tebaldini and Rocca, 2009, 2012b; Gatti et al., 2011].

The TomoSAR data phase calibration using AS approach is done by eliminating the ground phase contributions from the tomographic SLC data. The exploitation of Multi-Polarimetric and MultiBaseline (MPMB) data allow the identification of different Scatterer Mechanisms (SM) [Tebaldini and Rocca, 2012b]. The separation of the ground contribution and the vegetation from MPMB data is performed by presenting the data covariance matrix through Sum Kronecker Product SKP [Tebaldini, 2009a].

The structure model of the data covariance matrix, where each SM is presented by Kronecker Product of two matrices, is addressed as follows:

$$\begin{aligned} W &= E[YY^H] \\ &= \sum_{k=1}^N \lambda_k C_k \otimes R_k \approx C_g \otimes R_g + C_v \otimes R_v \end{aligned} \quad (3.3)$$

Where Y is the MPMB SLC data vector, H is the Hermitian conjugate, W denotes the data covariance matrix, k is the total number of SMs that contribute to SAR signal, $C_{g,v}$ and $R_{g,v}$ are the polarimetric signature and structure matrix corresponding to the ground and volume contribution, respectively.

The first step of Phase calibration is to retrieve an initial guess for ground phases by applying Capon spectrum estimation using HH channel, then the original data is corrected using this ground phase. Then the ground phases is retrieved by Sum of Kronecker Products (SKP) model. Assuming two main scattering mechanisms, ground and volume scatterings, we obtain the best LS approximation of the covariance matrix W by retaining the first 2 terms of the SKP Decomposition, and the matrices R_g , R_v , C_g , C_v can be determined from the terms of the SKP Decomposition, via a linear transformation. Starting from initialization of ground phases, one can present the initial guess of ground phase at each track n by:

$$\phi_n^{\text{initial}} = \frac{4\pi}{\lambda r \sin \theta_n} B_n z_g \quad (3.4)$$

where B_n is the normal baseline relative to track n , r is the slant range for the whole scene, z_g is the terrain topography, and θ_n is the look angle associated to each track n :

$$z_g = \operatorname{argmax} S_{\text{capon}}(z; HH) \quad (3.5)$$

Here, z denotes the vertical axis used in order to apply spectrum estimation problem. After that, we can retrieve the ground phases at each track n , it can be expressed by:

$$\phi_n^{\text{ground}} = \frac{4\pi}{\lambda r \sin \theta} B_n z_g + \eta_n \quad (3.6)$$

Where η_n is the phase screen at track n . After the estimation of the ground covariance matrix, Phase linking algorithm is applied to estimate ground phases.

$$\phi_n^{\text{ground}} = \text{PL}(\mathbf{R}_g) + \phi_n^{\text{initial}} \quad (3.7)$$

Where PL denotes the Phase Linking algorithm [Tebaldini et al., 2016]. After that, the calibration is carried out by removing ground phases from the original SLC data to obtain the calibrated SLC data.

$$Y_n^{\text{cal}} = Y_n \cdot \exp(-j \cdot \phi_n^{\text{ground}}) \quad (3.8)$$

Finally, Capon beamforming power estimation is applied to get the tomographic profiles.

3.2.5 TomoSAR inversion

SAR data were acquired over forests from slightly different altitude and incidence angles providing useful information in the vertical direction [Ho Tong Minh, D et al., 2017]. The L-band UAVSAR airborne system provides fully polarimetric mode in the NASA

AfriSAR campaign. Tomographic techniques composed of power estimation methods applied on the multi-baseline SLC data to retrieve the backscattered power that characterize the vertical profile of the forests [Ho Tong Minh, D et al., 2017; Ho Tong Minh, Dinh et al., 2014]. In this chapter, Capon beam forming power estimator is applied to represent the vertical profile of vegetated areas.

Capon beam forming

Capon beam forming is a non-parametric power estimation method used in the tomographic analysis that allows obtaining a continuous vertical profile without any knowledge on the statistical properties of the data [Stoica et al., 2005a]. The Capon estimated vertical profile $P_c(\xi)$ is retrieved from the covariance matrix of the MB SLC data [Gini et al., 2002a], and can be expressed as:

$$P_c(\xi) = \frac{1}{\mathbf{a}(\xi)^t \mathbf{W}^{-1} \mathbf{a}(\xi)} \quad (3.9)$$

where $\mathbf{a}(\xi)$ is the steering vector containing the interferometric information for a scatter at cross range ξ for all the baselines relative to a master track, and \mathbf{W} is the maximum likelihood estimation of the covariance matrix. \mathbf{Y} denotes the multibaseline SLC data configuration. N is the number of tracks. Note that since the inverse of the estimated covariance matrix is used, the Capon estimator requires \mathbf{W} to be well conditioned in order to ensure that \mathbf{W}^{-1} can be trusted.

3.2.6 Estimate forests top height

The canopy structure in tropical rain forests is more complex than any other forest type. The main challenge in such a field is the estimation of the forests top height because it is often hard to clearly identify the top leaf or branch of a tree in the canopy. TomoSAR has been demonstrated as a powerful tool to estimate the forests top height thanks to its accurate characterization of the vertical structure of tropical forests. Forests vertical structure can be observed by taking a tomographic profile, i.e. a slice of the multi-layer data stack. Using the Capon beamforming power estimator, we can retrieve the 3D backscatter distribution from the multi-layer SLC and show the vertical backscatter distribution function. Each ver-

tical distribution is characterized by two effective contributions, one corresponding to the signal, where most of the backscatter is concentrated, the so-called Canopy contribution or phase center, and another contribution corresponds to the reflected signal from ground. Figure 3.3 shows a schematic view of the vertical backscatter distribution in which it is assumed that the shape of the distribution can be divided into four zones. The first zone corresponds to the ground contribution which is the signal reflected from the ground. The second one corresponds to the canopy layer contribution. The third one is the power loss zone, where the backscatter undergoes a loss along the vertical direction from the phase center (canopy contribution) location. Further away, the backscatter Capon profile is dominated by noise, unlikely to be associated with any physically relevant components. Forests top height can be retrieved by two different ways, either by identifying the power loss from the phase center location in the upper envelope of the profile or by identifying the power loss from the noise level (location of the highest return detected by TomoSAR platform) to the forests top height.

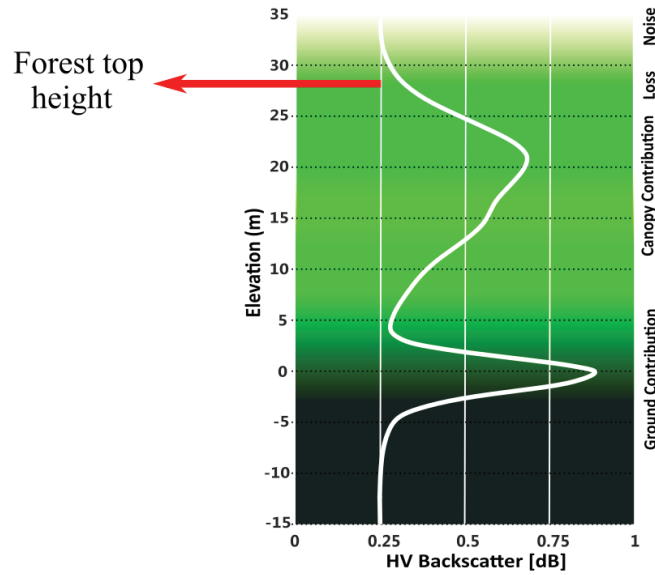


Figure 3.3 – The schematic view of the vertical backscatter distribution (TomoSAR Capon profile at certain cell).

$$H(r, x) = \operatorname{argmin}(P(H_n, r, x) - P(H_c, r, x) - K) \quad (3.10)$$

where $P(H_n, r, x)$ is the backscatter at the phase noise level, H_n is the elevation of the noise level, K is the power loss value, and H_c is the LiDAR height value from SFL data. Since the forest top height retrieval depends on the choice of the power loss value K , we used the CHM from the SFL dataset to select the optimal power loss value.

Tomographic imaging is carried out simply by taking the Fourier beamforming (with respect to the normal baseline) of the MB SLC data set at every slant range and azimuth location (r, x) . The result of this process is a multi-layer SLC stack, where each layer is referred to a height above the terrain. Here, we will refer to each image within the multi-layer data stack simply by the associated height (i.e.: 15 m layer, 30 m layer), or as a ground layer for the image focused at 0 m. To provide a comparison of tomographic layers associated with each height, we also show the layers of the selected study area extracted from the Lidar LVIS waveform.

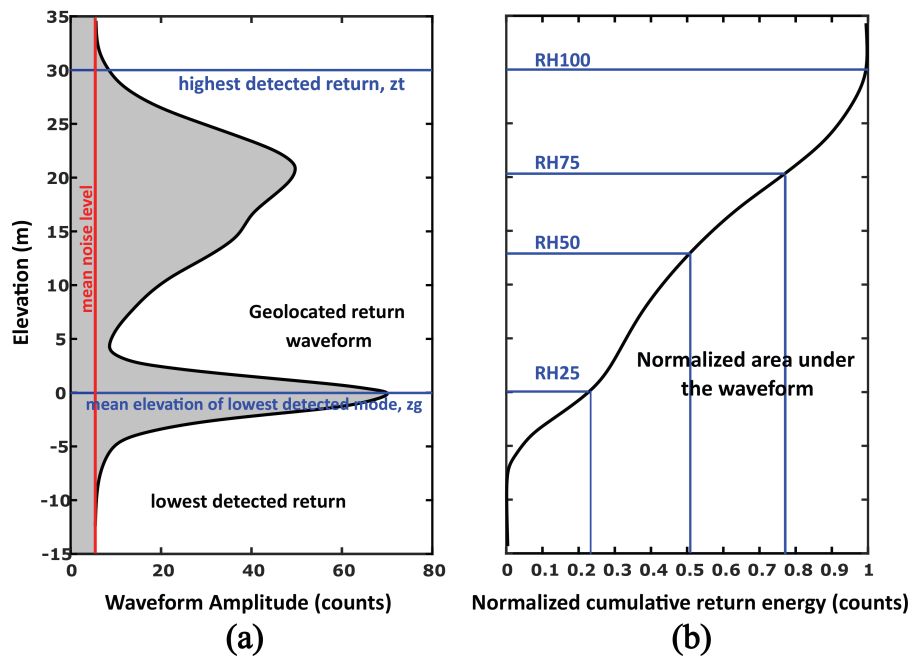


Figure 3.4 – (a) Schematic view of Lidar LVIS waveform divided into four zones. Zone 1: ground contribution, zone 2: Canopy contribution, zone3 : Noise and unwanted reflected signal. (b) Extraction of Lidar level 2 data from LVIS waveform. RH100 is the elevation of the highest detected return (forest top height). RH25 is the elevation where 25% of the waveform energy is occurs, it denotes the ground layer associated with LVIS data.

The schematic view of Lidar waveform is illustrated in Fig. 3.4, where it is characterized by canopy and ground contributions.

3.3 Results

This section is devoted to present the L-band tomographic imaging at different zones over the Gabon Lopé Park. The experiment has been formed based on N=7 tracks L-band fully polarimetric SAR images. The baseline spacing is 20 m, resulting in a total baseline of 120 m.

The backscatter SLC image, where we had chosen the studied sections, is illustrated in Figures 3.5a and 3.5b). The Tomogram has been validated using SFL data (Figures 3.5e and 3.5f).

The Capon estimator has been applied on sliding windows of 33x33 pixels ($n=1089$ pixel = 2722 m^2) for each position in the azimuth and range directions. The tomographic profiles from the Capon beamforming power estimator are normalized between 0 and 1. The first observation is that the tomographic profiles achieved a good correlation with the CHM and DTM from SFL data and clearly the canopy layer and ground layer are detected as shown in Figures 3.5e and 3.5f. A Qualitative comparison between HH, HV Capon profiles and LVIS profile is illustrated in Fig. 3.6. The LVIS Level 1B has been used to plot the vegetation profiles at different ROIs. The mean DEM value on the corresponding ROI has been added to the vertical sampling of the LVIS profiles for the sake of presentation. Also, the mean value of the SFL data for ground elevation DTM has been added to the canopy elevation CHM. We observe that the mean LVIS profiles are similar to the tomographic Capon profiles. Figure 3.7 shows original SAR image and the HH backscatterer for layers at ground layer 0 m, 15 m layer, and 30 m layer over the Gabon Lopé National Park.

The Lidar LVIS level2 data at three different layers are illustrated in Fig. 3.8. RH25, RH50, and RH75 are heights relative to the elevation at which 25 %, 50 %, and 75 % of the waveform energy occurs.

Moreover, forests top height from L-band TomoSAR data is estimated using the CHM

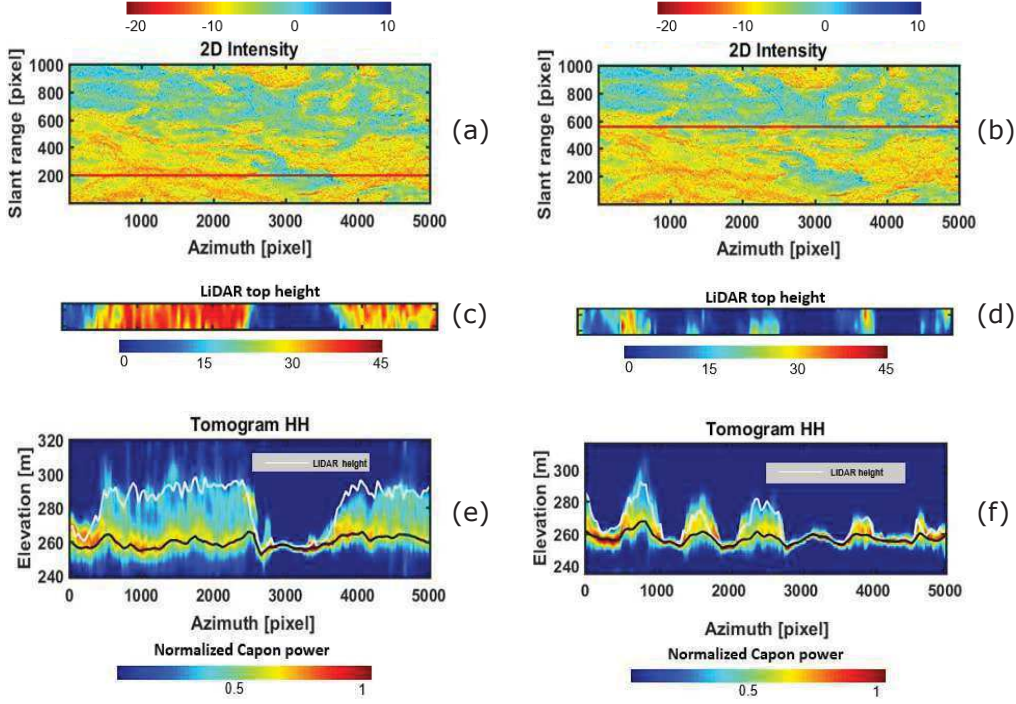


Figure 3.5 – (a,b) The 2-D intensity of the TomoSAR image; the red lines correspond to the slant range positions where the cut was chosen. (c,d) The Lidar cut at two slant range positions 200 and 590, respectively. (e,f) HH Capon spectra. The black and white lines in (e,f) correspond to the digital terrain model (DTM) and canopy height model (CHM) from small-footprint Lidar (SFL), respectively. Capon power was normalized between 0 and 1 to enhance visualization of the scatterers.

from SFL Lidar data. We assess forests top height location (in the tomographic profile similar to the schematic figure shown in Fig. 3.3) with respect to noise floor location, ranging the power loss from -11 dB to -8 dB with step 0.1 dB (as shown in Fig. 3.9). The bias associated with L-band TomoSAR top-height decreased regularly with the power loss, while the root mean square error is decreased from about 8.3 m at -11 dB down to 3.32 m at penetration loss equals to -9.2 dB, which is significantly low, then it tends to increase after this value to reach about 5.5 m at penetration loss value -8 dB. The bias value at penetration loss equals to -9.2 dB is -0.059 m. After obtaining the optimal value of penetration loss, we can estimate forest top height from TomoSAR data based on this value.

Then we compared the extrapolated L-band TomoSAR top-height with the CHM SFL

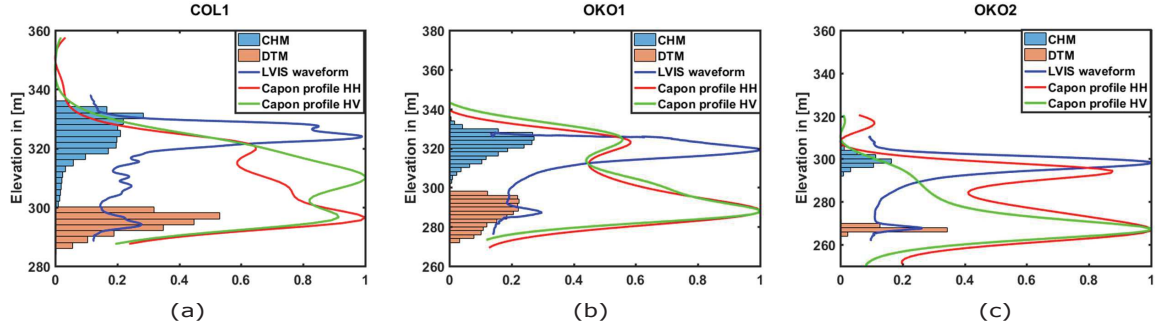


Figure 3.6 – Regions of interest (ROIs) named (a) COL1, (b) OKO1, and (c) OKO2 in the Gabon Lopé Park. HH(in red), HV(in green) Capon profiles. Capon power and LVIS waveform power are normalized between 0 and 1. The histograms of SFL canopy and ground elevations are presented respectively in blue and in brown. The blue curve corresponding to LVIS waveform Level 1B.

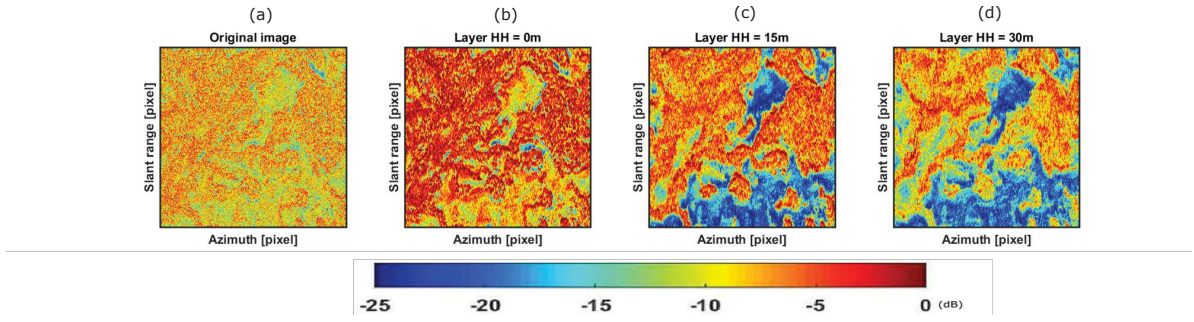


Figure 3.7 – (a) original SAR image. HH power intensities associated with SAR image with three layers produced by TomoSAR, (b) 0 m, (c) 15 m, (d) 30 m.

data over the same area. Fig. 3.10 shows forests top height estimated from Fig. 3.10a L-band TomoSAR, Fig. 3.10b CHM from SFL data, and Fig. 3.10c shows the difference between the estimated height (from L-band TomoSAR) and reference height CHM.

Figure 3.11 displays the distribution of the difference between the estimated height by L-band TomoSAR data and CHM from SFL data. The histogram is similar to the normal distribution function and it is unbiased. Bias is equal to -0.059 m where the RMSE is equal to 3.32 m and the coefficient of determination has a value of 0.92.

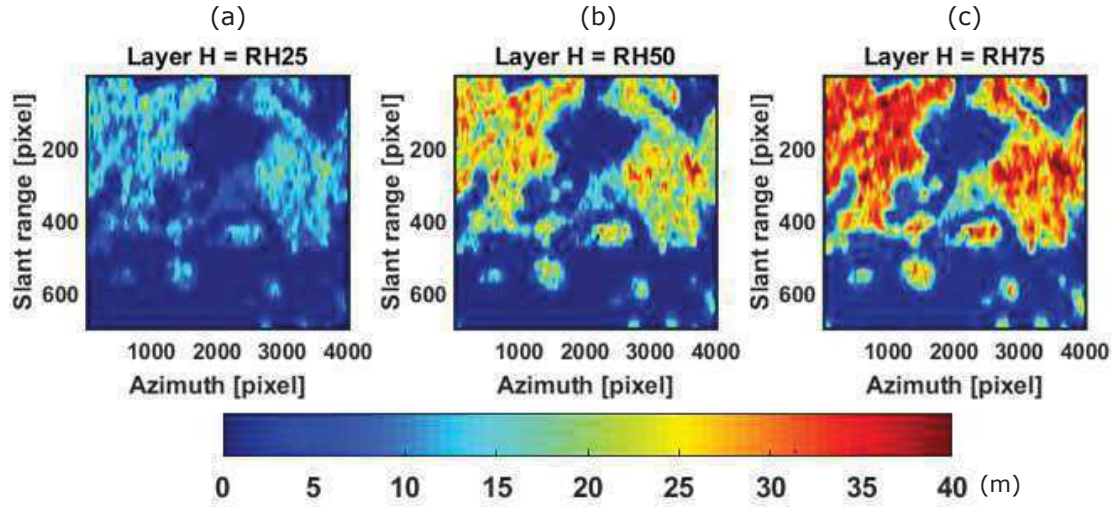


Figure 3.8 – Lidar LVIS Level2 different layers (a) RH25, (b) RH50 and (c) RH75 corresponds to the Lidar LVIS layers. RH25% represents the elevation where 25% of waveform energy occurs (ground layer). RH50% represents the elevation where 50% of waveform energy occurs, and RH75% represents the elevation where 75% of waveform energy occurs.

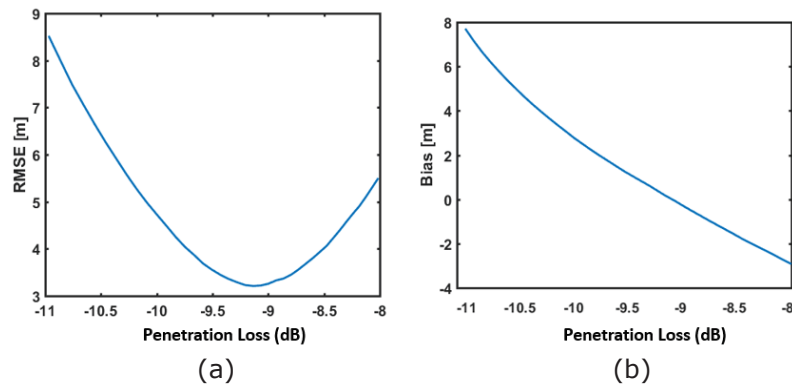


Figure 3.9 – (a) forests top height RMSE and (b) bias versus penetration loss with respect to Noise floor elevation.

3.4 Discussion

In this chapter, it is proved that L-band TomoSAR imaging can be feasible even in tropical forests. A tomographic study is implemented using L-band NASA/JPL UAVSAR data collected during the AfriSAR campaign 2016. We show tomograms at different sections of the Lopé and we validated it with SFL data. A qualitative comparison is done between

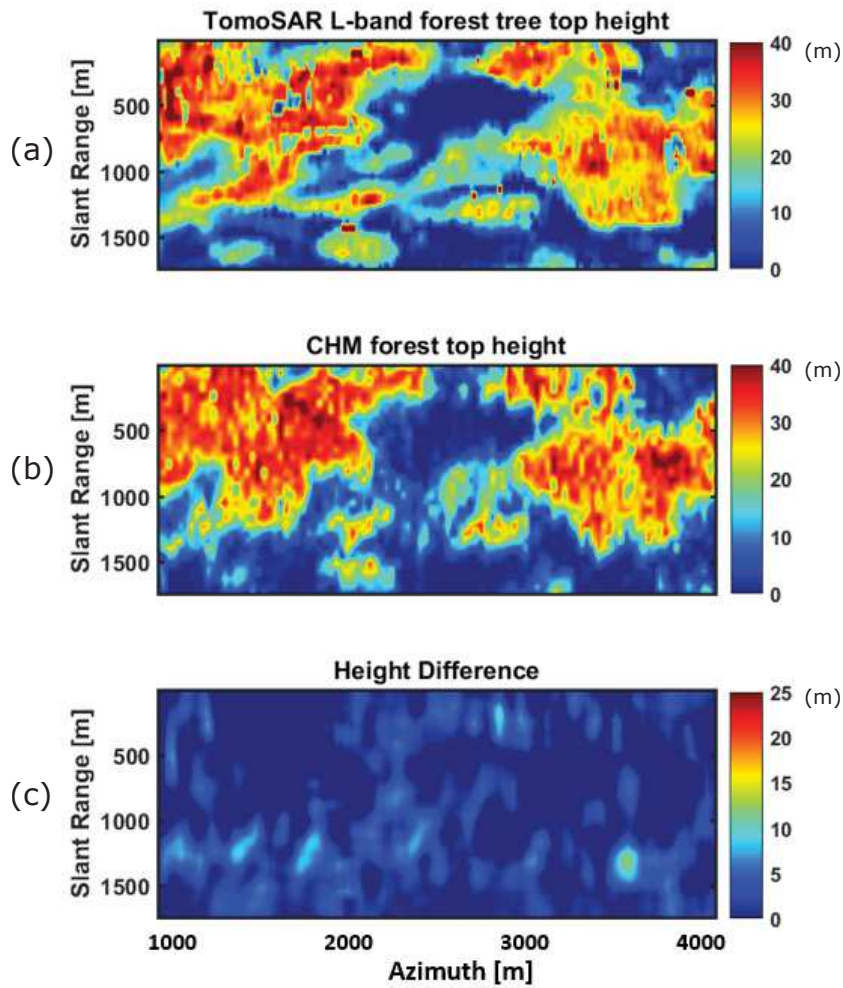


Figure 3.10 – (a): Tree top height from L-band TomoSAR. (b): CHM from SFL data. (c): Relative difference between Lidar and TomoSAR tree top height, height difference = (HTomo - HLidar).

Capon profiles and LVIS waveforms at different ROIs in the Gabon Lopé Park. Finally, the forest top height from UAVSAR data has been estimated. Thus, these results can confirm our expectation in the ability of L-band TomoSAR to characterize accurately the tropical forests 3D structure. In order to analyze TomoSAR results, good knowledge about the main factors that control effectively the correct illumination of the scatterers above the ground is required. These factors are: the quality of the tomographic data, power estimation meth-

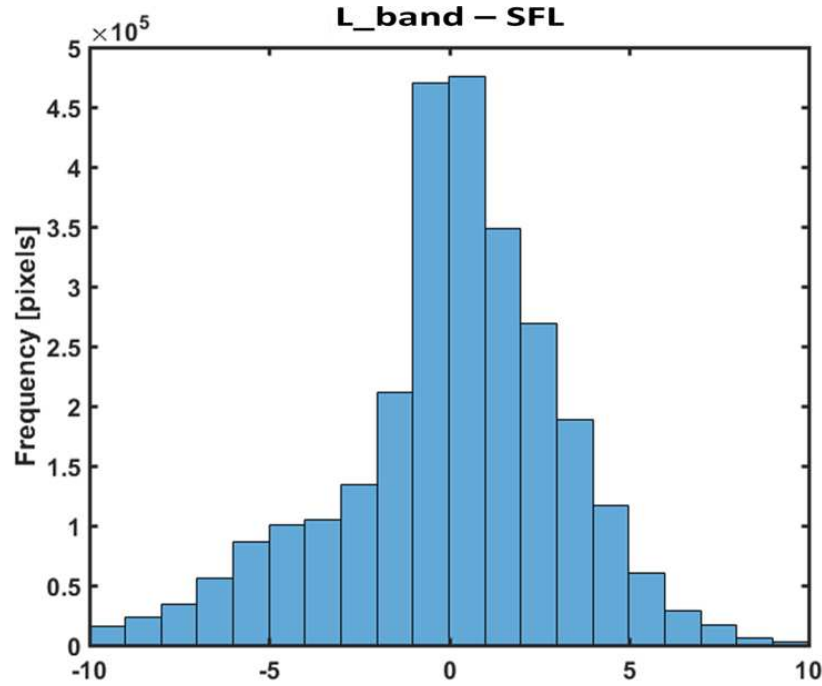


Figure 3.11 – Histogram of the height difference (L_band - SFL Lidar data).

ods used in the tomographic inversion, the operating frequency of TomoSAR signal and TomoSAR vertical resolution.

First, the ability to penetrate through the canopy down to the ground is assessed using L-band TomoSAR data. Canopy and ground layers are detected correctly. The tomogram has been validated by SFL. In contrary to our study, a previous work, which has been carried out on French Guiana [Ho Tong Minh, Dinh et al., 2015a], has shown a limitation in using L-band data concerning the illumination of the scatterers for dense forests of 30 m height and more. While in this chapter, we established a correct illumination of the scatterers above the ground in dense tropical forests using L-band TomoSAR (Fig. 3.5). Capon beam forming has been applied on a sliding window of 33x33 pixels (1089 total pixels) for each position in azimuth and slant range direction. Knowing that using Capon windows of 33x33 pixels which may blur the details in the vertical direction, it provides a general understanding of the vertical structure of vegetation.

Second, a strong correlation is detected between the Capon profiles at different po-

larization channels with the LVIS waveform and the distribution of SFL data, opening prospects to estimate tropical forests vertical structure using L-band TomoSAR (see Fig. 3.6). The LVIS and Capon results show great similarities. The Capon profiles at these three ROIs are not similar to those found from P-band TomoSAR in [Wasik et al., 2018]. The study carried out over Gabon forests using P-band TomoSAR data in [Wasik et al., 2018] show that the HH ground contributions are stronger than HV for the analyzed ROIs, while HV canopy contributions are larger than those of HH. Indeed, this behavior is expected for P-band imaging. Here, it is highlighted that we do not have the same performance of P-band concerning the behavior of polarization channels (HH and HV) at L-band data in terms of canopy and ground signals. In our study, the operational response of L-band TomoSAR differs over the ROIs. We can observe the consequence of the weaker penetration capabilities of the LVIS system compared to the L-band TomoSAR in the high vegetation volumes COL1 and OKO2. The penetration potential of each platform can be seen very well in the regions where we have dense vegetation (COL1 and OKO2). We noticed a small shift or offset in the Canopy contribution location. Also, it is clear that the ground contribution from L-band TomoSAR is stronger than those of LVIS data.

Moreover, when observing Fig. 3.7, it is found that the ground layer image is characterized by better contrast information compared to the original SAR image. The signal at ground level is focused by the tomography processing, thus rejecting the contributions from the vegetation layers and allowing the characterization of the polarimetric signature of ground scattering. We can study the behavior of polarimetric signature with respect to topographic terrain ground slope and often interpret this behavior by a physical model to understand well different scattering mechanisms (single bounce, double bounce). For the sake of comparison with TomoSAR layers, we display the LVIS Level 2 data Fig. 3.8. It contains geo-referencing information of different reflecting surfaces, the locations of which have been derived from the Level 1B waveform, within the laser footprint. The typical surface parameters are ground elevation, canopy top elevation, canopy height and several other height metrics. We assume that RH25 represents the ground layer [LVI] of Lidar LVIS waveform, RH50 represents the 15 m layer, and RH75 represents the 30m layer. Regarding

the RH25 layer, there is no ground contribution because of the penetration capabilities of the Lidar LVIS which is different from SAR penetration performance.

Finally, the canopy height estimation using L-band TomoSAR data can be performed efficiently even in tropical forests. By evaluating the vertical forests structure from tomographic profiles, forests top height can be retrieved. Using the CHM from SFL data as a reference, the power loss value of -1.8 dB (from -11 dB to -9.2 dB we have 1.8 dB difference) with respect to the noise floor location (in the vertical profile distribution, upper zone) was used to retrieve forests height with no bias and minimum errors. Note that the same power loss value cannot straightforwardly be transferred to other campaigns study cases. As shown in the frame of the BioSAR 2008 campaign [Tebaldini and Rocca, 2012a], the power loss should be varied in space due to a strong variation of the vertical resolution across the scene swath. Here, the RMSE was estimated to be 3.32 m as shown in Fig. 3.9. This shows that there is no limitation for the implementation of a canopy height retrieval algorithm with L-band TomoSAR. Recent studies reported RMSE 2.5 m using P-band TomoSAR in tropical forests [Ho Tong Minh, Dinh et al., 2014]. P-band penetration performance is better than L-band due to its longer wavelength, which allows fewer interactions with leaves and branches leading to a deeper penetration to the ground layer. To give precise knowledge about the accuracy of our proposed method applied in estimating forest top height, we show in Fig. 3.10c the spatial distribution of the height differences between L-band TomoSAR and Lidar height. After analyzing the histogram of Fig. 3.11, it is noticed that the histogram of the height difference between TomoSAR and Lidar tends to be normally distributed. We can generalize that the height difference values (between TomoSAR and Lidar) are distributed around -0.059 m, having an RMSE of 3.32 m. Our results considerably reinforce the proposal that L-band TomoSAR will be able to provide highly accurate 3D vertical structure even in high dense forests worldwide.

3.5 Conclusion

In this work, the TomoSAR analysis has been applied for estimation of the forests canopy height and terrain using L-band UAVSAR AfriSAR data collected over the Gabon

Lopé Park on February 2016. Prior to tomographic imaging, a phase residual correction methodology based on Sum Kronecker Product has been implemented. The tomographic capon profiles at different sections in the forests are validated in a good correlation with SFL Lidar data DTM and CHM from the SFL data set as a reference. Second, we compared the vertical profile of vegetation at different sections in the Lopé using L-band TomoSAR Capon power estimator at HH, HV polarizations with LVIS Level 1B waveform Lidar data were carried out over different regions of interests in the Gabon Lopé National Park. Finally, we report on the performance of forests top height retrieved from the TomoSAR L-band data. Forests top height from L-band data is estimated and validated with SFL data having an RMSE of 3.32 m. The result demonstrates that L-band tomographic imaging can now be carried out even in the dense tropical forests. We hope that our results reinforce the scientific basis to estimate tropical forests structure using TomoSAR at L-band. L-TomoSAR appears to be a promising technique to be used for the retrieval of tropical forests height. One of the main perspectives is to compare TomoSAR analysis using L- and P-band in tropical forests, showing their capabilities in retrieving the 3D structure of tropical forests, and to provide support of using L-band TomoSAR in the future biomass estimation missions.

Monitoring tropical forest structure using SAR tomography at L and P-band

Contents

4.1	Introduction	85
4.2	Materials and Methods	88
4.3	Results	99
4.4	Discussion	105
4.5	Conclusions	110

4.1 Introduction

Tropical Forests play a vital role in the global carbon cycle, and subsequently within the global climate [Wright, 2005]. Tropical forests are incredibly complicated, diverse, and frequently threatened. Indeed, there’s a crucial demand to develop a new technology to help in surveying and revealing the dynamics of tropical forests. The dynamic processes like growth, regeneration, decay, and disturbance, strongly affects the forest 3D structure. For-est 3D structure is so closely associated with their history, diversity, function, and micro-climate [Spies, 1998]. At the same time, forest structure information is essential for de-veloping a precise forest biomass estimators. The latter is needed to observe better and

evaluate forest ecosystems' contribution in the overall carbon cycle [Grace, 2004; Gatti et al., 2014; Froking et al., 2009]. Traditionally, forest structure observation has been implemented by inventory plots at local scales. Inventory measurements provide correct estimates of a variety of single trees and stand parameters. However, these measurements are time demanding and they are performed at smaller scales. The extrapolation of those plot measurements from into larger scales depends on the ability of these measurements to represent their surrounding landscape [Fischer et al., 2019]. The establishment of the temporal continuity of these measurements is challenging. Remote sensing techniques have the potential to overcome this limitation and make an enormous contribution in qualitative and quantitative observation of three-dimensional forest structure [Hall et al., 2011; Bergen et al., 2009; Goetz et al., 2007; Turner et al., 2003].

Today, Tomography Synthetic Aperture Radar (TomoSAR) and airborne LiDAR are the two technologies that allow the measurement of 3D forest structure. Measures derived from the LiDAR waveform are utilized to evaluate structural forest parameters as forest height and biomass [Tello et al., 2018]. Recently, continuous forest mapping with global coverage at spatial and temporal resolutions is assessed and established using SAR imaging configuration. Indeed, a big effort has been put to demonstrate the potential of typical SAR configurations to estimate spatial biomass utilizing SAR measurements [Beaudoin et al., 1994]. The SAR system provides measurements sensitive to the whole vegetation and from the underlying ground at high spatial resolution. The initial step started with introducing SAR interferometry as it has an exaggerated sensitivity to forest geometry and vertical structure components. Polarimetric interferometric SAR measurements allows model-based inversion to assess vertical forest structure parameters such as forest height and biomass [Treuhft and Siqueira, 2000; Garestier et al., 2009; Cloude and Papathanassiou, 1998, 2003]. The next step is using multi-baseline interferometric acquisitions in order to reconstruct the vertical distribution of the scatterers [Reigber and Moreira, 2000]. Recently, tomographic acquisitions, which will be seen as an extension of multi-baseline interferometric acquisitions, have been used to reconstruct the three-dimensional radar reflectivity of forests [Reigber and Moreira, 2000; Frey and Meier, 2011; Neumann et al., 2010; Caicoya et al., 2015; Tebaldini and Rocca, 2012b; Aguilera et al., 2013; Pardini and

[Papathanassiou, 2012](#)]. The promising outcomes accomplished initiated the execution of TomoSAR acquisition modes in future spaceborne SAR missions, like Biomass [[Le Toan et al., 2011](#)] or Tandem-L [[Krieger et al., 2016](#)], for mapping structural forest parameters and to enhance the performance of biomass estimators at a global scale.

TomoSAR has been demonstrated to be a powerful tool for observing forested areas from space owing to its capability in providing vertical resolution based on multi-baseline observations [[Reigber and Moreira, 2000](#); [Gini et al., 2002b](#); [Tebaldini, 2009b](#); [Huang et al., 2012](#)]. Tomographic techniques consist of power estimation strategies applied to the multi-baseline Single Look Complex (SLC) data to retrieve the back-scattered power that characterizes the vertical profile of forests [[Ho Tong Minh et al., 2016, 2014](#)]. In its most simple formulation, TomoSAR aims to extract the vertical distribution of the backscattered power within the system resolution cell. A potential answer to the current problem is to take advantage of super-resolution techniques like Capon beamforming, Multiple Signal Classification, Singular Value Decomposition analysis, and others [[Gini et al., 2002b](#); [Sauer et al., 2007](#)]. A unique solution could also be found within the works by Fornaro et al. [[Fornaro et al., 2005](#)] and Cloude [[Cloude, 2007, 2008](#)], wherever super-resolution is achieved by exploiting prior information concerning target location, like ground topography and canopy height model [[Cloude, 2008](#)]. The capabilities of L-band TomoSAR to characterize 3D vertical structure of tropical forests are still in early stages of development while those of P-band TomoSAR have been discussed and evaluated. Ho Tong Minh et al. [[Ho Tong Minh et al., 2015a](#)] used the airborne data that were acquired during TropiSAR campaign to prove that the use of L-band tomographic imaging in tropical forests seems limited. The first experience in testing TomoSAR in tropical forest areas was carried out in French Guiana by the TropiSAR campaign in 2009. However, these data were sub-optimal to assess the performance of multi-frequency TomoSAR in monitoring the forest structure and estimating forest structure parameters as forest top height. To overcome such limitation, and acquire optimal tomographic and polarimetric data, the AfriSAR campaign was successfully carried out over the dense forests of Gabon in 2015 and 2016. Nevertheless, the link between physical forest structure and the reconstructed 3D radar reflectivity is still

not understood and is far from being established. The main challenge, thus, is the interpretation of 3D radar reflectivity in terms of the 3D forest structure parameters.

The 3D radar reflectivity relies on the operating system frequency and polarization. Plus, it also depends on the used acquisition geometry (e.g., incidence angle), and the achieved 3D spatial resolution. In fact, the generic interpretation of 3D reflectivity is difficult because scatters that are seen by radar are changing with frequency and polarization. Accordingly, this chapter focuses mainly on comparing the capabilities of L- and P-band TomoSAR to extract forest top height. First, the P- and L-band vertical profiles are validated with a Canopy Height Model (CHM), which is obtained from a Small Footprint LiDAR (SFL) dataset. Second, qualitative comparisons of the Capon beamforming profile at HH and HV (H: horizontal, V: vertical) polarizations with Land Vegetation Ice Sensor (LVIS) Level 1B waveform LiDAR data and CHM and Digital Terrain Model (DTM) from SFL data, over the region of interest in Gabon Lopé National Park, are carried out. Additionally, forest top height is retrieved from the TomoSAR data.

The chapter is organized as follows: Section 4.2 describes the study area, datasets, and methods used for the tomographic analysis. Section 4.3 illustrates the validation of the results. Section 4.4 is devoted to discuss and interpret the tomography results. Section 4.5 demonstrates the concluding remarks.

4.2 Materials and Methods

4.2.1 Study Area

To develop algorithms that assess the performance of BIOMASS SAR measurements in different forest ecosystems, several airborne field campaigns have been designed and implemented. One can name the AfriSAR campaign in Gabon, BioSAR campaign in Sweden, and TropiSAR campaign in French Guiana (Figure 4.1).

The AfriSAR campaign aims to provide support to forthcoming NISAR, GEDI and BIOMASS missions. Four sites presenting various forest structures have been selected: Lopé, Mabounie, Mondah, and Rabi, located, respectively, at 250 km, 180 km, 25 km, and

260 km from the Libreville airport, where the calibration site was deployed. In this section, we will focus on the presentation of Lopé, which is the primary acquisition site. Lopé National Park, a 4913 km² national park in central Gabon, is known as one of the largest parks in the area. The scene of the northern part consists of the last remnants of grass savanna that was created in central Africa, during the ice age from 15,000 years ago. This natural site is composed of vast areas of Savanna in the north, which is surrounded by the Ogooué River and frequently burned in order to preserve the forests' Savanna areas, in addition to an extended area of tropical forests that are combined with parts of successive forests of complex structure, which were developed throughout time with savanna recolonization [Lee, 2001]. Lopé is a convenient natural view to prove the adequate performance of tomographic imaging because of the gradient of forest biomass from the forests' savanna boundary (up to 100 Mg/ha), to dense undisturbed humid tropical forests (greater than 400 Mg/ha). The height and structure of the trees vary gradually from savanna into forests, which provide uniform mono-dominant trees of okoume (OKO) of tall: 30–50 m for regions with the presence of significant gaps in mid-canopy. This creates skewed vertical profiles. Lopé topography is also diverse. It varies between either broad flat plains or steep sloping terrains. OKO2 region is selected to perform a qualitative analysis between UAVSAR–TomoSAR L-band, SETHI P-band vertical profile, and LiDAR waveforms.

4.2.2 Data-Set

During the AfriSAR campaign, different datasets have been acquired over the Gabon Lopé National Park. The NASA sponsored AfriSAR campaign involved three data sets, L-band UAVSAR data, LVIS LiDAR data, and SFL data. ONERA and DLR defined a common configuration for P-band imaging of their radar systems. P-band SAR P-band acquisitions were performed by ONERA (SETHI radar system) in July 2015 and by DLR (F-SAR radar system) in February 2016.

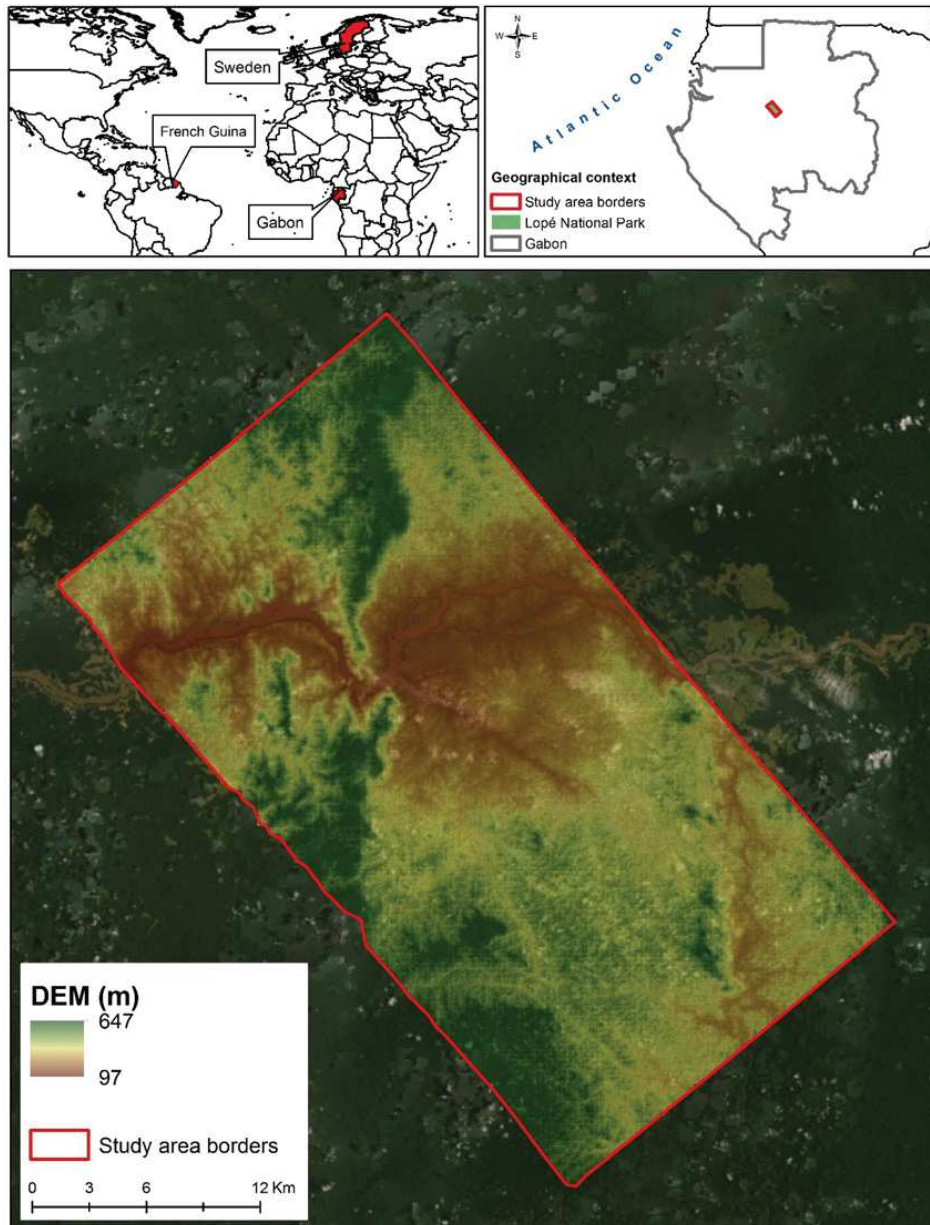


Figure 4.1 – TropiSAR, BioSAR , and AfriSAR Campaigns. Study area main site (Gabon Lopé National park). The red polygon denotes the footprint of L-band UAVSAR platform. The Digital elevation model of the Lopé is displayed.

LiDAR Data-Sets

Throughout the AfriSAR campaign, the SFL data set was collected by the NASA Jet Propulsion Laboratory (JPL) in July 2015, with a footprint diameter of 10 cm. Canopy

Height Model (CHM) and Digital Terrain Model (DTM) rasters are provided with 1 m spatial resolution. The second LiDAR dataset was collected in March 2016, NASA's Land Vegetation Ice Sensor (LVIS) acquired the LiDAR data set as part of NASA–ESA's BIOMASS, GEDI, and NISAR calibration and validation activities. LVIS is a large-scale, waveform LiDAR with applications for measuring ground elevation and vertical profile of the vegetation structure in various ecosystems. The LiDAR datasets LVIS consists of two levels: Level 1B and Level 2 (data can be downloaded from https://lvis.gsfc.nasa.gov/Data/Data_Download.html). Level 1B data contain geo-referenced LiDAR returned waveforms, such that, at each footprint, we have a corresponding shot number, and, using this shot number, one can get the LiDAR waveform at each footprint. Level 2 data contain geo-referencing data for different reflecting surfaces within the laser footprint, the locations of which were derived from the Level 1B waveform.

Radar Acquisition Configuration

The tomographic data set here consists of seven fully polarimetric Single Look Complex (SLC) data L-band NASA/JPL UAVSAR from AfriSAR data conducted over the Lopé during the AfriSAR campaign in 2016. The operating band of UAVSAR platform is 1217.5–1297.5 MHz. The scanning of about a 22 km wide area, with incidence angles extending from 25 to 60 degrees, is performed by the Gulfstream III jet at that flight at an altitude of 12.5 km. The ground range and azimuth resolution of the UAVSAR polarimetric SLC are 1 m and 2.5 m, respectively. The tomographic SLC data acquired over Lopé by increasing the flight altitude by 20 m each flight track. The configuration of L-band UAVSAR is shown in Table 4.1, while the P-band data consists of 13 fully polarimetric SLC data acquired by ONERA over the Lopé in the AfriSAR airborne campaign (July 2015). The data collection is performed using the SETHI SAR system developed by ONERA and onboard a Falcon 20 aircraft. The pixel resolution of the SLC images is 1.54 m in azimuth range and 3 m in slant range. The configuration of P-band SETHI data including acquisition geometry, bandwidth, carrier frequency, and aircraft altitude are shown in Table 4.2.

The tomographic 125 MHz data set considered in the Paracou experimental site consists of six fully polarimetric SLC images at L and P-band acquired on 24 August 2009. All

Table 4.1 – L-band UAVSAR acquisition parameters.

Acquisition Parameters	
Acquisition Mode	PolSAR
Look Direction	Left looking
Pulse duaration	40 (μ s)
Steering Angle	90 (deg)
Bandwidth	80 (MHz)
Ping-Pong or Single Antenna Transmit	Ping-Pong
Air craft speed	224 (m/s)
Range of look angle	21–65 (deg)
Antenna Length	1.5 (m)

Table 4.2 – Description of the SETHI system configuration of P-band acquisition parameters. The superscript * indicates the parameters that are identical between the SETHI and F-SAR systems.

Acquisition Parameters	
Acquisition Mode *	PolSAR
Look Direction	Left looking
Effective Pulse Repetition Frequency (PRF)	1250 (Hz)
Steering Angle	90 (deg)
Frequency range */Bandwidth	50 (MHz)
Pulse duration	30 (μ s)
Transmitted power	500 (W)
Aircraft speed	100–150 (m/s)
Flight ground altitude	6096 (m)

the acquisitions took about 1 h (from 9:00 a.m. to 10:00 a.m.), resulting in almost no temporal decorrelation.

In this chapter, we also used six tracks fully polarimetric images acquired during TropiSAR campaign over Paracou. In the following section, we will compare P and L band tomographic results conducted over Gabon Lopé Park with the LiDAR data set SFL.

4.2.3 Tomography SAR

TomoSAR implementation requires accurate handling concerning the relative phase difference between different acquisitions. The rationale of TomoSAR is to use multiple flight tracks that are nearly parallel to each other [Ho Tong Minh et al., 2015a], as shown within the left panel of Figure 4.2.

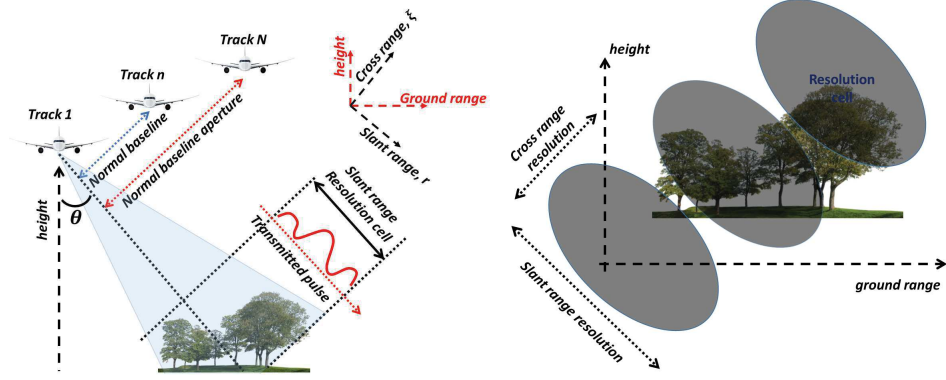


Figure 4.2 – TomoSAR acquisition.

The ensemble of all flight lines allows the formation of 2D synthetic aperture, ensuing the coherent multiple Single Look Complex (SLC) images of various passes, providing the likelihood of focusing the signal within the entire 3D space. We will refer to (r, x, ξ) as the slant, azimuth, and cross ranges, respectively. Consider a dataset of SLC images acquired by N parallel track sensors, denoted by $Y_n(r, x, \xi)$, representing the SLC value inside the resolution cell (r, x, ξ) within the n -th image. The expression of topography-compensated (tc) SLC data are often approximated [Tebaldini et al., 2015] as:

$$Y_n(r, x)^{tc} = \int P(r, x, \xi) \exp(jK_n \xi) d\xi, \quad (4.1)$$

where $P(r, x, \xi)$ denotes the projection of target reflectivity on the cross-range axis ξ , and ξ represents the cross-range coordinate, orthogonal to the measuring system line-of-sight (LOS) that are outlined by the slant range coordinate. In TomoSAR applications, the vertical sensitivity of the phase difference between two acquisitions is linked through the vertical wavenumber k_n expressed by:

$$K_n = \frac{2\pi}{H_0 A} = \frac{4\pi}{\lambda R} b_n, \quad (4.2)$$

where HoA is the height of ambiguity, λ is the radar wavelength, R is the slant-range distance, and b_n is the horizontal distance between the two acquisitions.

4.2.4 Tomography Inversion

SAR data were acquired over forests from slightly different altitude and incidence angles, providing helpful information within the vertical direction [Ho Tong Minh et al., 2016]. In this chapter, the Capon beamforming power estimator was applied to represent the vertical profile of vegetated areas. The Capon spectral estimator is a conventional non-parametric method in tomographic analysis that enables one to obtain the endless vertical profile of the vegetation without any prior knowledge on the statistical properties of the data [Stoica et al., 2005b]. The Capon estimator vertical profile $P_c(\xi)$ is retrieved from the covariance matrix of the SLC data [Gini et al., 2002b]:

$$P_c(\xi) = \frac{1}{\mathbf{a}(\xi)^t \mathbf{W}^{-1} \mathbf{a}(\xi)}, \quad (4.3)$$

where $\mathbf{a}(\xi)$ is the steering vector containing the interferometric information for a scatter at cross range ξ , for all the baselines relative to a master track, and \mathbf{W} is the maximum likelihood estimation of the covariance matrix. t is the transpose operator.

4.2.5 TomoSAR Phase Calibration

The previous section described the theoretical model for tomographic analysis assuming no disturbances on the path of the propagating signal. Prior to Multi-baseline SAR algorithms, the phase calibration of the TomoSAR data should be taken into account, in order to compensate the phase residuals that influence the focusing of Multi-baseline SAR data. These phase disturbances originate from atmospheric propagation delays or uncertainties in allocating the platform position.

Indeed, for airborne systems, the atmospheric perturbations are limited (no ionosphere propagation). The phase screen compensation method chosen to be applied on the Lopé data are largely inspired by the work of Tebaldini et al. [Tebaldini et al., 2015]. A simple proposition is to assume that the phase residuals only result from uncertainties in

the antennas' positions (Figure 4.3). The phase screens α_n can be approximated as a function of dZ_n and dY_n , which represent, respectively, the position errors of the platform n in altitude and in the ground range direction for a fixed position in azimuth [Tebaldini et al., 2015]:

$$\alpha_n = \frac{4\pi}{\lambda} (-dY_n \sin\theta + dZ_n \cos\theta). \quad (4.4)$$

The Double Localization iterative procedure described in detail in [Tebaldini et al., 2015] is then put in place. The calibration is carried out by removing phase screens from the original SLC data to obtain the calibrated SLC data:

$$Y_n^{\text{cal}} = Y_n \cdot \exp(-j \cdot \alpha_n). \quad (4.5)$$

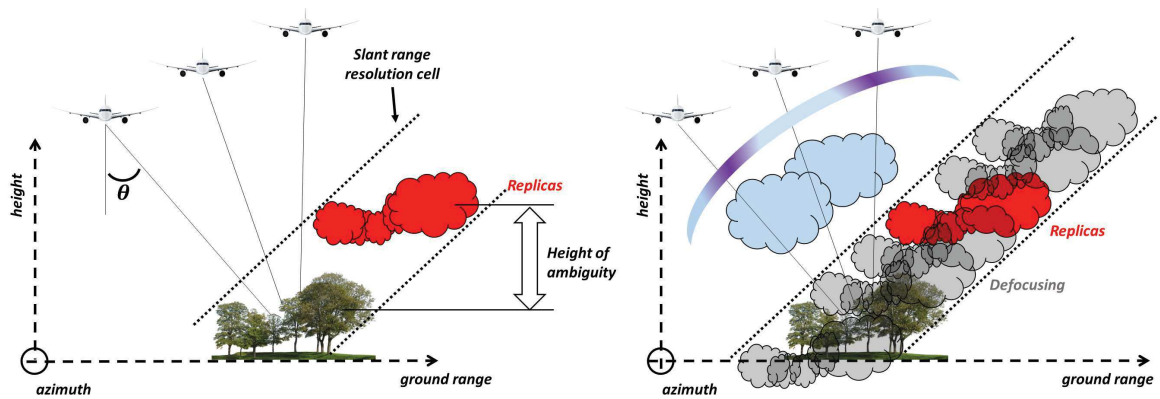


Figure 4.3 – Phase calibration problem formulation.

4.2.6 Forest structure indices

The objective of this section is to characterize a framework for the estimation of forest structure from TomoSAR data and LiDAR data. This framework is inspired from Cazcarra-Bes et. al [Cazcarra-Bes et al., 2017a]. In the following, the 3D forest structure is understood as the vertical and horizontal arrangement of trees and/or tree elements in space. In spite of the troubles in finding a proper characterization for forest structure for a wide scope of applications, spatial scales, and forest types, it is regularly accepted that two basic aspects

of forest structure are the heterogeneity in the position and size of the trees inside a stand. In light of this, an efficient system for the separation of biologically critical structure classes has as of late been proposed [Tello et al., 2015; Bohn and Huth, 2017], which proposes two indices measures: one for the horizontal, and one for the vertical structure. These indices can be estimated from the 3D reflectivity profile. Tello et. al [Tello et al., 2015] discussed about the link between the 3D reflectivity profile and the physical structure of the forest and proposed the methodology to calculate these indices. Basically, the horizontal structure index essentially mirrors the thickness of the tallest trees in the unit zone considered, while the vertical structure file represents the assorted variety of tree heights. In this way,

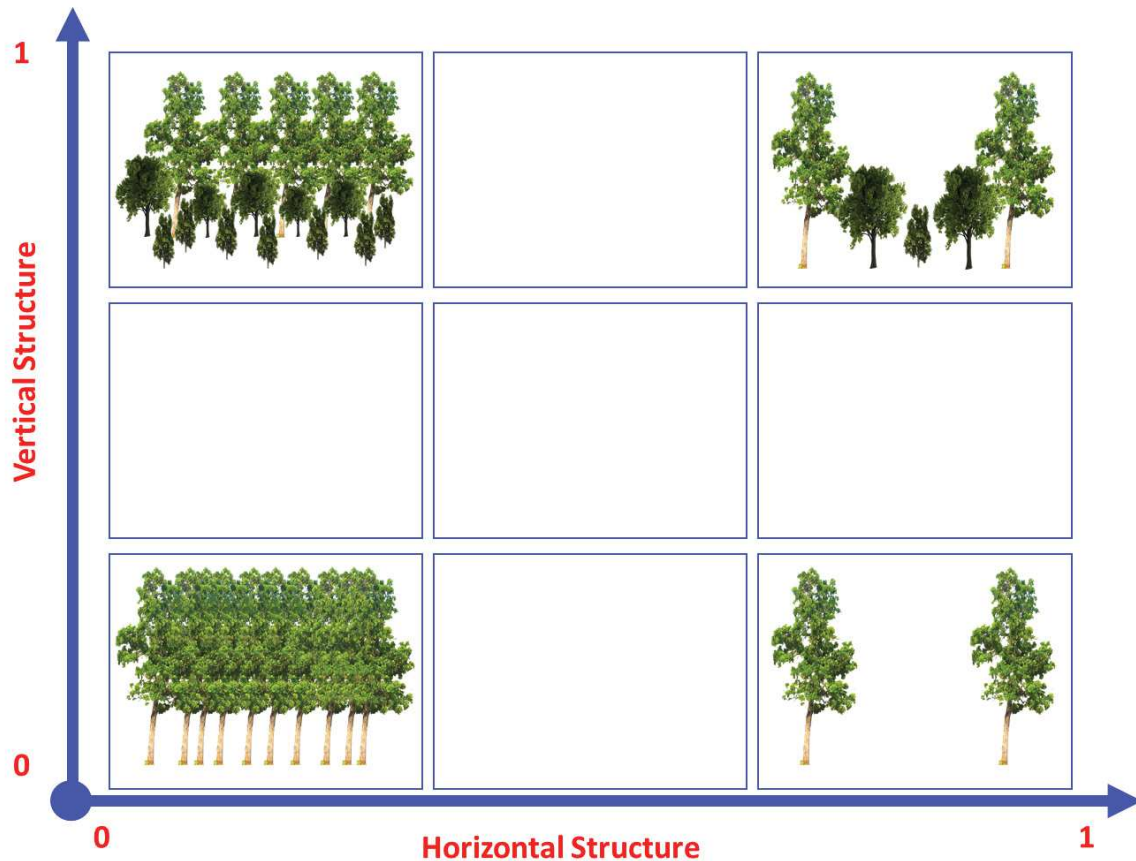


Figure 4.4 – Horizontal/vertical structure plane proposed for forest structure classification.

as indicated by its basic multifaceted nature, a forest stand can be grouped in a horizon-

tal/vertical plane (HV plane in the accompanying) has appeared in Figure 4.4. As the initial step, the tops for each reflectivity profile in the range and azimuth were extracted from the radar reflectivity representing the distribution of scatters along height T. At each point, A three-dimensional (range, azimuth, height) matrix B is characterized by ones at the position of each peak. From this framework, the horizontal and vertical indices were assessed. The Horizontal descriptor HS index at each pixel is estimated as the number of peaks in the upper layer in the unit window centered on that pixel divided by the area of this unit window:

$$HS = \frac{n \times (P_{top})}{S} \quad (4.6)$$

The upper layer is defined as the range of peaks heights between $0.6 h_{max}$ and h_{max} . Where P is the set of peaks, $n(P_{top})$ is the number of peaks in the top layer, S is the area of the unit window. HS is normalized to its maximum HS_{norm} within the scene and $1 - HS_{norm}$ is considered in order to reflect disorder: 0 indicates low and 1 indicates high structural disorder or complexity. Concerning the vertical index descriptor, it is defined as follows:

$$VS = M \times \text{var}(H_p) \quad (4.7)$$

where H_p is the vector of size M obtained from H_p after accounting all peaks that appear at the same height only once and ignoring the peaks of the ground. A minimum height is set and peaks below this height are disregarded. In this chapter, the height threshold is set to 5 m (see the red area in Figure 4.5), Finally, the descriptor of the vertical forest structure VS is normalized to its maximum VS_{norm} within the scene.

4.2.7 Forest Structure Parameters

The main parameter we want to estimate is forest top height. The principal challenge in tropical forests is the estimation of the forests' top height since it is usually difficult to

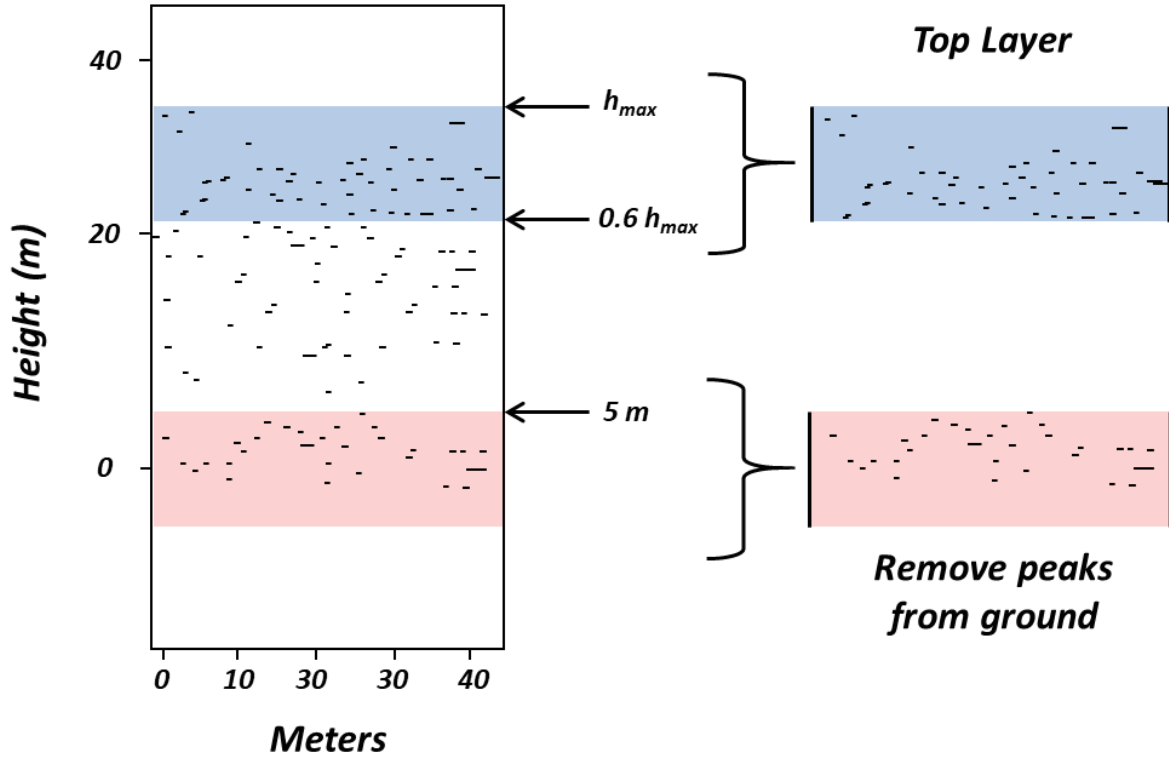


Figure 4.5 – Definition of top layer for the horizontal structure index and the threshold to remove peaks introduced by the ground scattering contributions.

clearly recognize the top leaf or part of a tree in the canopy. Utilizing the Capon beam-forming power estimator, we can recover the 3D backscatter profile from the multi-layer SLC and demonstrate the vertical backscatter distribution function. To do this, we applied the method proposed in [El Moussawi et al., 2019] and we estimated the forest top height H from L- and P-band data:

$$H(r, x) = \operatorname{argmin}(P(H_n, r, x) - P(H_c, r, x) - K), \quad (4.8)$$

where $P(H_n, r, x)$ is the backscatter at the phase noise level, H_n is the elevation of the noise level, K is the power loss value, and H_c is the LiDAR height value from SFL data. Since the forest top height retrieval depends on the choice of the power loss value K , we used the CHM from the SFL dataset to select the optimal power loss value. One can estimate the canopy height model from TomoSAR data by either ranging the power loss from the

phase center location in the upper envelope of the Capon profile, or by ranging the power loss from the noise level (location of the highest return detected by the TomoSAR) from H_n down to the canopy contribution peak elevation in the upper envelope of the 3D profile. At each position, the Root Mean Square Error (RMSE) between the H height and H_c is calculated at given K value ($H(r,x) - H_c(r,x)$); once we have the lowest value of RMSE, we get the forest top height H at each (r,x) position.

4.3 Results

In this section, the limitation of L-band TomoSAR imaging in dense forests using TropiSAR data acquired over Paracou is illustrated; then, we report the results of forest structure characterization over Gabon Lopé National Park by means of tomography imaging using AfriSAR L- and P-band TomoSAR SLC data.

4.3.1 Limitation of L-Band TomoSAR in Tropical Forest (TropiSAR Data)

Figure 4.6 presents the tomographic profile of a constant range section at P- and L-band in tropical Paracou forest and Boreal Krycklan forest. For better visualization, the panels have been normalized in a way that the sum along the height is unitary. In the boreal Krycklan forest, the white line denotes forest top height derived from LiDAR measurements. At the tropical forest in Paracou, the L-band tomogram is not clear at all, as there is a blurring phenomenon, while, on the other hand, the P-band tomogram is clear. The different vegetation layers are illuminated correctly. However, for the Boreal Krycklan forest, the tomograms at L- and P-band are clear with no significant disturbances.

4.3.2 TomoSAR Profiles at L- and P-Band (AfriSAR Data)

Figure 4.7 presents the tomographic profile at a constant slant range cut (centered on the pixel number 200) before and after phase screen correction at a P-band HH channel. Note that UAVSAR L-band data are adapted to phase screen correction. The improvement

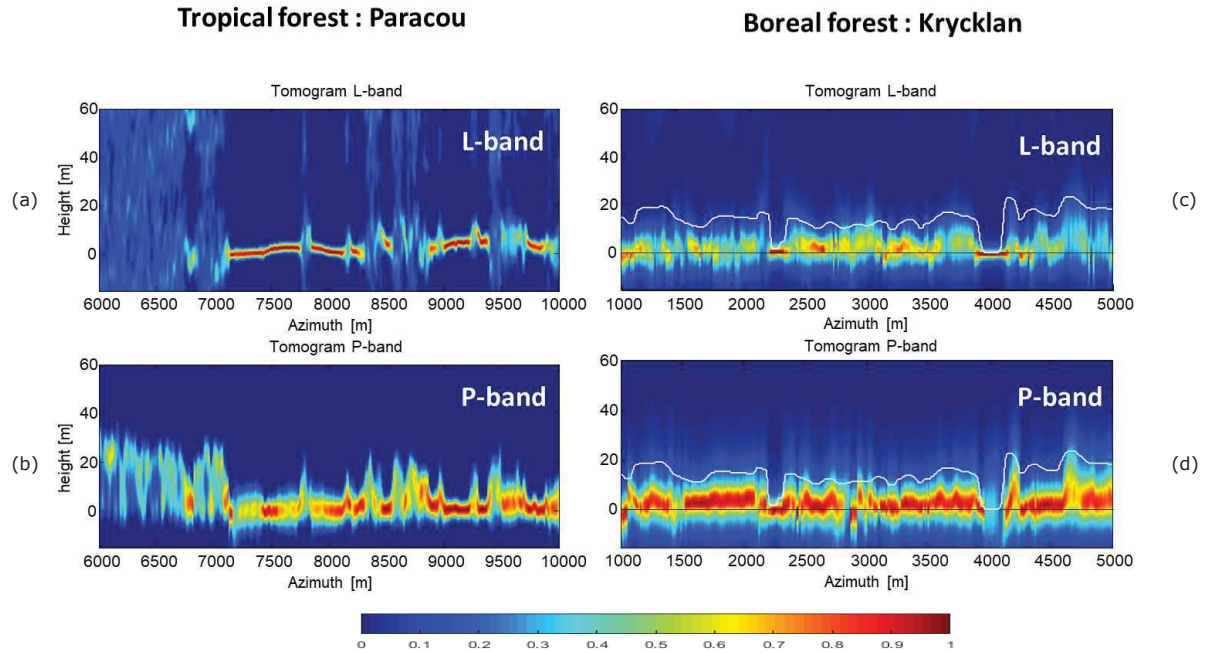


Figure 4.6 – (a) L-band Tomogram (HH channel) at Tropical Paracou forest; (b) P-band Tomogram (HH channel) at Tropical Paracou forest; (c) L-band Tomogram (HH channel) at Boreal Krycklan forest; (d) P-band Tomogram (HH channel) at Boreal Krycklan forest. The algorithm used to get the tomography profiles is the Capon beamforming power estimator.

brought by the phase screen removal for this region is highly visible, providing side lobes' attenuation.

In Figure 4.8, the estimated tomographic profiles for two cuts of the Lopé site in the slant range direction at P-band HH channel, L-band HH channel, and LVIS data are presented. The Capon beamforming estimator has been applied on radar data using a sliding window of $10 \text{ m} \times 25 \text{ m}$ (area of 250 m^2 for each position in the range direction). Using the same sliding window, the average of LiDAR LVIS Level 1B power layers is estimated. It is noticed that the tomograms from different sources of data achieve a good agreement with CHM from SFL data. In addition, we can observe from the tomogram of LVIS data at the two cuts that the penetration capabilities of the Lidar LVIS platform are weak when compared to the penetration performance of radar data. The canopy and ground layers are clearly detected by L- and P-band tomography while it is not the case when applying

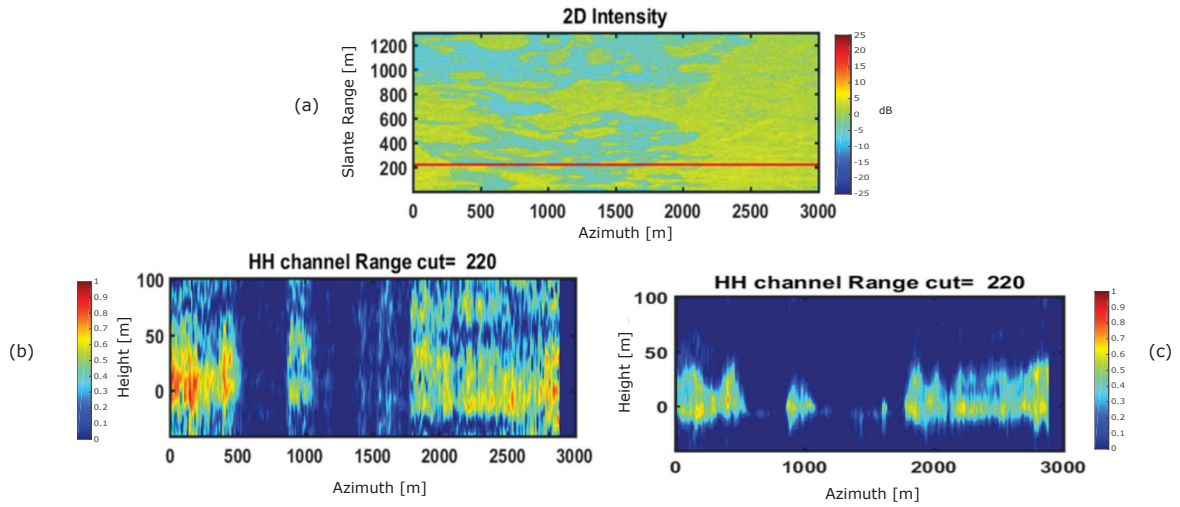


Figure 4.7 – (a) 2D intensity of SLC P-band image. The red line denotes the cut where the Capon beamforming estimator was applied; (b) P-band Tomogram (HH channel) before applying phase screen correction; (c) P-band Tomogram (HH channel) after applying phase screen correction.

tomography on LVIS data. It is worth mentioning that, for some pixels, the canopy layer is not well detected by TomoSAR; this requires studying the physical aspects of radar signals taking into account the ground slopes and the forest type (dry, wet).

Figure 4.9a–c represent the canopy height peak estimated from LiDAR waveform, L-band tomographic data, and P-band tomographic data, respectively. The estimation is performed over a study area of $875 \text{ m} \times 2000 \text{ m}$ ($1,750,000 \text{ m}^2$). The histogram of the differences between canopy peak height estimated from the three different datasets is displayed in Figure 4.10. The RMSE between the canopy peak height estimated from P-band data and canopy peak height estimated from L-band data are about 3.25 m, where the bias value is equal to 0.28 m. However, the RMSE values between L-band and LiDAR on one hand, P-band and LiDAR, on the other hand, are 9.55 m and 9.76 m, respectively. Their corresponding bias is -6.43 and -6.7 , respectively. The coefficient of determination had a value 0.95, 0.85, and 0.86, respectively.

The vegetation profile of OKO2 region at Lopé has been obtained from L-band (HH channel), P-band (HH channel), and LVIS Level 1B data (Figure 4.11). The histograms of

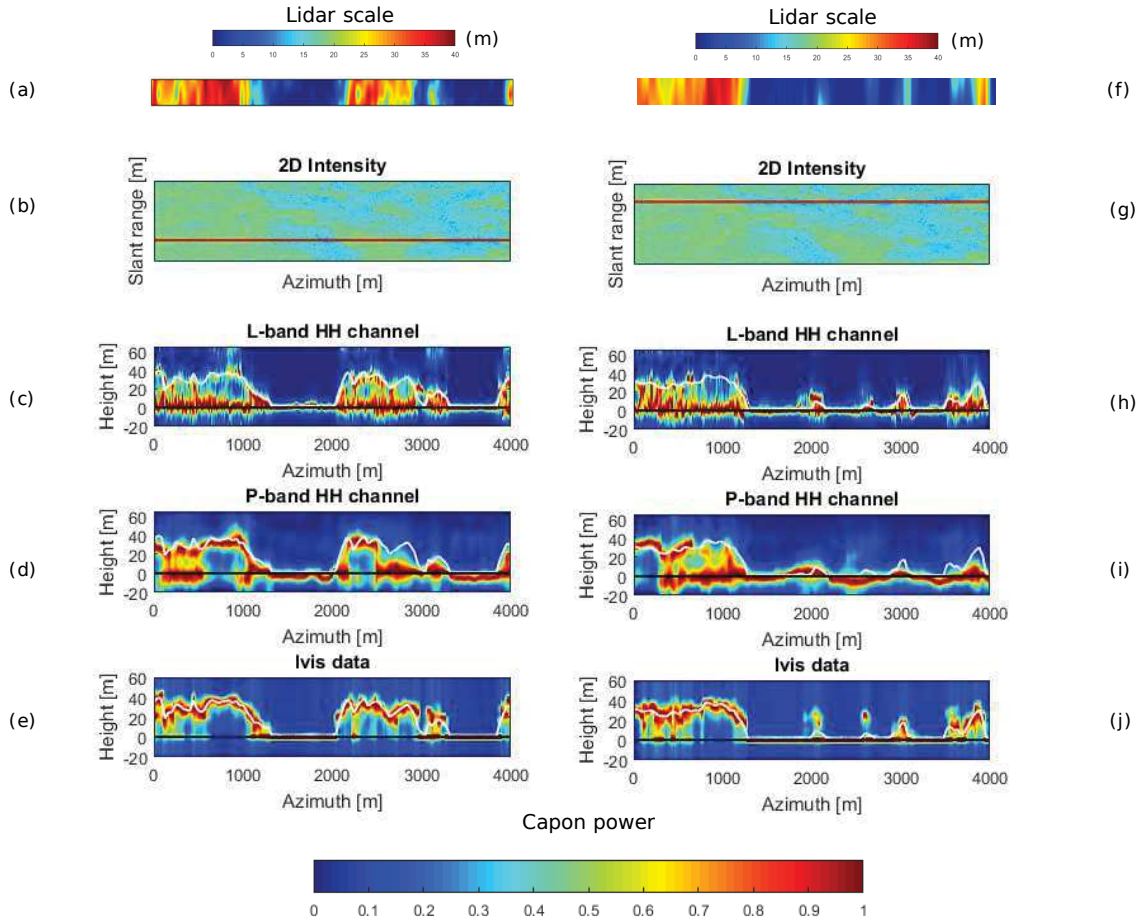


Figure 4.8 – (a) and (f) SFL CHM LiDAR cuts at slant range equal to 300 m and 650 m; (b) and (g) 2D intensity L-band SLC image. The red line denotes the cut where we had chosen to estimate the vertical structure along with slant range; (c) and (h) L-band HH channel Tomographic profile at the two cuts (300 m and 650 m); (d) and (i) P-band HH channel Tomographic profile at the two cuts (300 m and 650 m); (e) and (j) LVIS data layers from LiDAR LVIS Canopy Height Model (CHM), which is obtained from a Small Footprint LiDAR (SFL) it is defined before as land vegetation and ice sensor Level 1B at the two cut, defined before (300 m and 650 m). The white line in all tomograms denote the RH75 height from LiDAR LVIS Level2 data.

SFL data for ground and canopy elevations (DTM and CHM) are shown in Figure 4.11a, while Figure 4.11b presents the vegetation profile at OKO2 from L- and P band data at both HV channels.

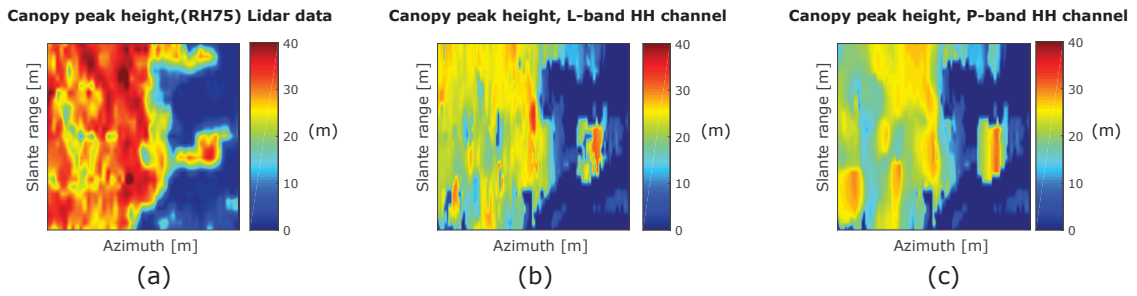


Figure 4.9 – (a) canopy peak height estimated from LiDAR waveform (RH75); (b) canopy peak height estimated from L-band data; (c) canopy peak height estimated from P-band data.

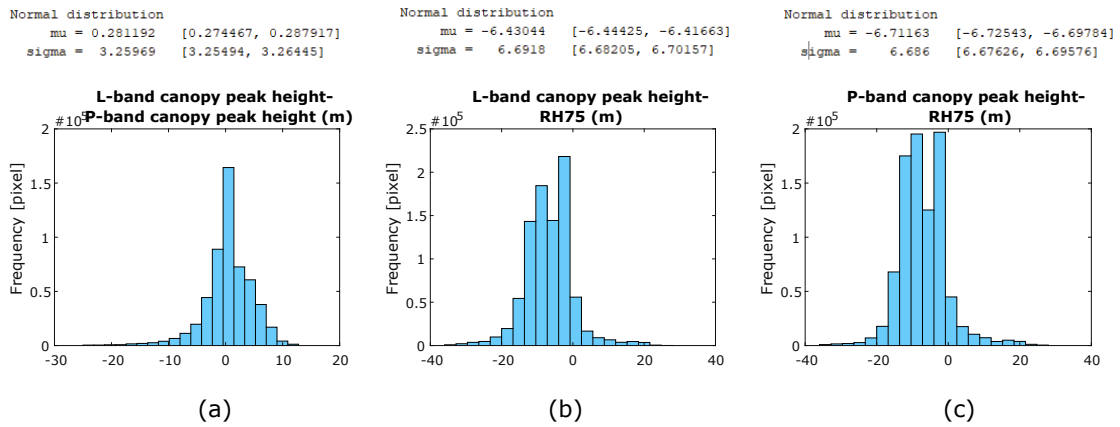


Figure 4.10 – (a) histogram of the difference between canopy peak height estimated from P-band data and canopy peak height estimated from L-band data; (b) histogram of the difference between canopy peak height estimated from L-band data and canopy peak height estimated from LiDAR LVIS Level1B data (or RH75 from LiDAR LVIS Level2 data); (c) histogram of the difference between canopy peak height estimated from P-band data and canopy peak height estimated from LiDAR LVIS Level1B data.

4.3.3 TomoSAR Multi-Layers

Figure 4.12 shows the HH backscatter for the original, ground layer (0 m), 15 m layer, and 30 m layer at P- and L-band and LVIS Level 1B data. It is noticed that the ground layer image is characterized by better contrast information compared to the original data at both P- and L-band. This can be explained as the signal at ground level being focused on

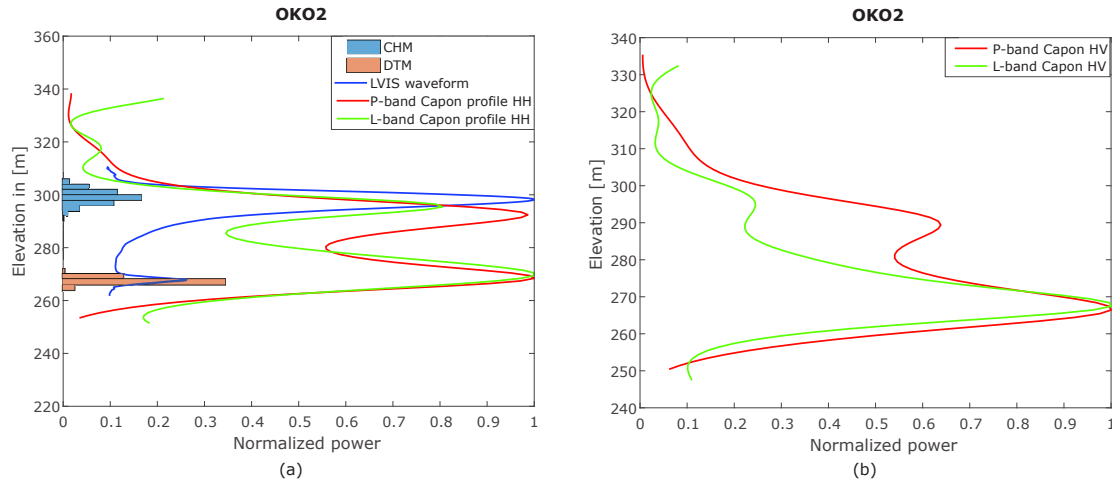


Figure 4.11 – (a) region of interest (ROI) named OKO2 in Gabon Lopé Park. P-band HH (in red) and L-band HH (in green) Capon profiles. Capon power and LVIS waveform power were normalized between 0 and 1. The histograms of SFL canopy and ground elevations are presented respectively in blue and brown. The blue curve corresponds to LVIS waveform Level 1B; (b) P-band Capon HV profile in red. L-band Capon HV profile in green.

the tomography processing, and rejecting contributions from the upper vegetation allows a better characterization of the polarimetric signature of ground scattering.

4.3.4 Forest Top Height Estimation from L- and P-Band

In Figure 4.13a, the CHM from SFL data is shown, while Figure 4.13b shows the forest top height estimated from L-band TomoSAR data in the same area. The relative differences between L-band CHM and SFL CHM data are shown in Figure 4.11c (Relative height difference = $(\text{LbandCHM} - (\text{LidarCHM})/(\text{LidarCHM}))$). Figure 4.13e presents the forest top height estimated from P-band data. The relative difference between P-band CHM and SFL CHM data are shown in Figure 4.13f (Relative height difference = $(\text{PbandCHM} - (\text{LiDARCHM})/(\text{LiDARCHM}))$). The difference between the estimated height from L-band, P-band and CHM from SFL data are shown in Figure 4.13d,g, respectively. The bias of the difference (histogram) between L-band CHM and SFL CHM is equal to -0.0681 , where the RMSE value is 3.68 m; the coefficient of determination shows a value of 0.93 . Regarding the histogram of the difference between P-band CHM and SFL CHM, the bias value is equal to

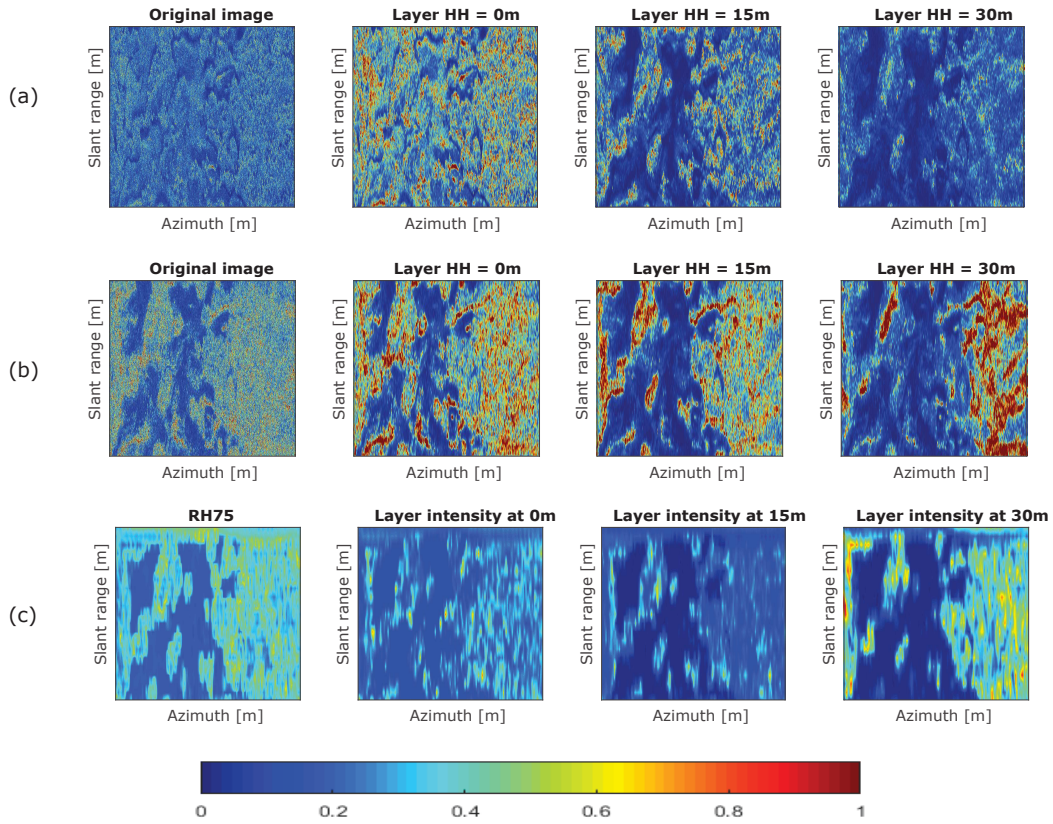


Figure 4.12 – (a) original SAR image. HH power intensities associated with an L-band SAR with three layers produced by TomoSAR: 0 m, 15 m, 30 m; (b) original SAR image. HH power intensities associated with a P-band SAR with three layers produced by TomoSAR: 0 m, 15 m, 30 m; (c) power intensities associated with LVIS data layers produced from LiDAR LVIS Level 1B data: 0 m, 15 m, 30 m.

−0.1151, where the RMSE value is equal to 3.02 m, and the coefficient of determination shows a value of 0.95.

4.4 Discussion

In this work, the ability of L-band TomoSAR imaging to retrieve tropical forest structure parameters has been assessed. A tomographic study was implemented using L-band NASA/JPL UAVSAR data, and P-band SETHI data from ONERA collected during the AfriSAR campaign in 2015 and 2016. We show L- and P-band tomograms at different sections of the

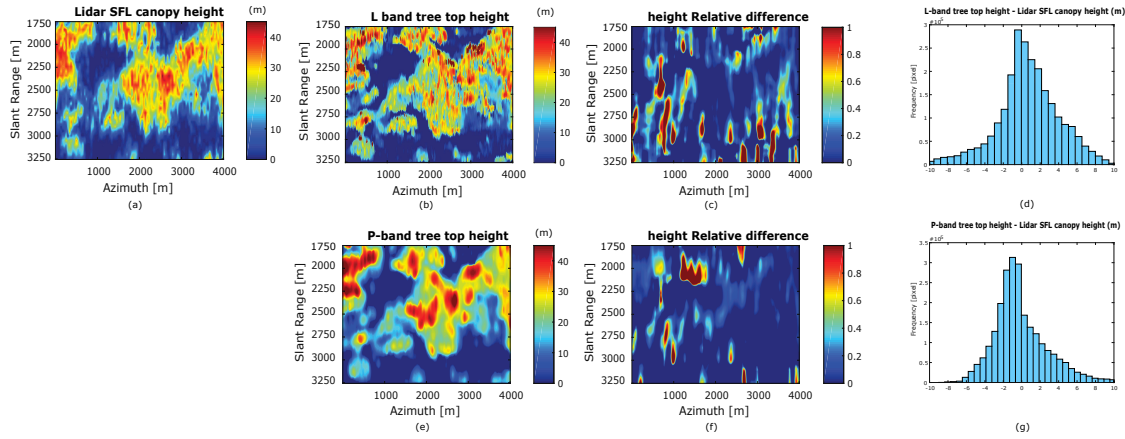


Figure 4.13 – (a) CHM from SFL data; (b) forest top height estimated from L-band TomoSAR data; (c) relative difference between LiDAR and L-band TomoSAR tree top height, height difference = $(H_{\text{Tomo}} - H_{\text{LiDAR}}) / H_{\text{LiDAR}}$; (d) histogram of the difference between the estimated height from L-band and CHM from SFL data; (e) forest top height estimated from P-band TomoSAR data; (f) relative difference between LiDAR and P-band TomoSAR tree top height, height difference = $(H_{\text{Tomo}} - H_{\text{LiDAR}}) / H_{\text{LiDAR}}$; (g) histogram of the difference between the estimated height from P-band and CHM from SFL data.

Lopé and we validated it with CHM from SFL data. We demonstrated that the analysis is improved significantly when the airborne data were corrected for the residual phases related to the perturbations because of motions and flight trajectories uncertainties during the data acquisitions. The impact of phase screen correction in the tomographic inversion is displayed, where it is shown in the tomogram at slant range cut before and after phase calibration. A qualitative comparison is made between Capon profiles from L- and P-band data and LVIS waveforms at a region of interest named OKO2 in the Gabon Lopé Park. Finally, the forest top height from UAVSAR and SETHI data has been estimated. Together, these results confirm our expectation in the ability of TomoSAR to characterize the tropical forests 3D structure accurately.

4.4.1 Limitation of L-Band TomoSAR in Tropical Forest (TropiSAR Data)

The average Height of Ambiguity in L-band tomographic TropiSAR data are about 30 m in the near range and 50 m in the far range. The L-band tomogram is quite disturbed when compared to the P-band tomogram (Figure 4.6) for a dense forest of 30 m and above. In this condition, the use of tomographic imaging at L-band in tropical forests appears limited. Such limitation needs more elaborated processing either in the configuration setup of the acquisitions or in the tomographic techniques and phase calibration. However, when the forest top height is roughly below 20 m (e.g., in forest regrowth), the tomographic results are expected to be the same as in boreal forests.

4.4.2 TomoSAR Profiles at L- and P-Band (AfriSAR Data)

The analysis is done here in the azimuth direction for a fixed slant range positions (sliding window centered on the pixel number 300 m and 650 m). The Capon profile for the HH channel is shown in Figure 4.8 for the corrected data only. In this profile, it can be noticed that, even if the SFL data and the corrected tomographic profiles seem to show generally a good correlation at the two bands L and P, the mean SFL elevations can sometimes be notably different from the positions of the peaks of the Capon profiles. This could be linked to the SFL data that do not describe the same location due to the difference in penetration capabilities between radar signals and SFL or to other uncompensated effects. After analyzing the histograms of Figure 4.10, the differences in the canopy height peak estimated from L-band, P-band, and LiDAR waveform are mainly originated from the difference in the penetration capabilities of TomoSAR at L- and P-band, and the LiDAR LVIS platform. In addition, this was expected. The platform resolution is another cause for the high observed bias.

The same interpretation is carried out for a specific region of interest in the Lopé named OKO2. The difference in the vegetation profile shapes between the LVIS and the Capon profiles may be originated from a difference in penetration capabilities or a variation of profile resolution between LVIS and TomoSAR data. After comparing the LVIS and the Capon pro-

files, the results show significant similarities. Despite the fact that tomography SAR in L & P bands with Capon estimator may not be able to produce vertical profiles with a resolution as good as the LVIS imaging system, it can always reveal stronger ground contribution as shown in the studied ROI (OKO2).

4.4.3 TomoSAR Multi-Layers

By observing Figure 4.12, and by comparing with the original SAR image at L- and P-band TomoSAR data, we found that the ground layer image has better contrast information. This implies that a ground-level signal is focused by tomography processing, thus rejecting contributions from vegetation layers and permitting the characterization of polarimetric signature of the ground scattering. The behavior of a polarimetric signature can be studied with respect to the topographic terrain ground slope. It often uses a physical model for interpreting this behavior to better understand the various scattering mechanisms (single bounce, double bounce). To compare with TomoSAR layers, the LVIS Level 1B and level 2 data as tomography were processed through reconstructing the LiDAR waveform along the z-axis; thus, the LVIS multi-layer similar to TomoSAR layers was obtained (Figure 4.12). Qualitatively, regarding the ground layer (or 0 m), no ground contribution is present because of the LiDAR LVIS penetration capabilities, which are lower than those of SAR.

4.4.4 Forest Top Height Estimation from L- and P-Band

The canopy height estimation is performed using the L-and P-band TomoSAR data in the Gabon Lopé National Park. By evaluating the vertical forests structure from tomographic profiles, the forests' top height can be retrieved using CHM from SFL data as a reference. Here, RMSE was estimated to be 3.68 m for L-band TomoSAR as Figure 4.13d, while the value of RMSE is 3.02 m using P-band TomoSAR data. This reveals as before that no limitation is present for the implementation of canopy height retrieval algorithm with the L-band and P-band TomoSAR. The penetration performance of P-band is better than that of L-band due to its longer wavelength. The latter permits fewer interactions with the

leaves and the branches, thus leading to deeper penetration of the radar signals to reach the ground layer. In order to give precise knowledge about the accuracy of the proposed method that is applied in estimating the forest top height, Figure 4.13c,f show the spatial distribution of height differences between L-band TomoSAR, P-band TomoSAR and that of LiDAR height. By analyzing the histogram of Figure 4.13d,g, one can notice that the height difference histogram between TomoSAR and LiDAR tends to be normally distributed. Our results considerably reinforce the proposal that L-band TomoSAR will be able to provide a highly accurate 3D vertical structure even in the densest forests worldwide.

4.4.5 Forest Structure Indices and Parameters

As prospective work, we aim to estimate the forest structure indices as the vertical and the horizontal indices that support biomass retrieval algorithms and enhance forest management activities. However, the forest structure is an important factor in its ecology as it is correlated with many ecological processes [Pretzsch et al., 2010; Shugart et al., 2010; Mundell et al., 2010]. Furthermore, it is also used as an indicator to detect the biodiversity, where the vertically structured forests foster some taxa biodiversity [Boncina, 2000; Ishii et al., 2004; Schall et al., 2018]. In addition, either the horizontal or the vertical structural heterogeneity can enhance the forest ecosystems' resistance against disturbances [Dobbertin, 2005; Pretzsch et al., 2016]. Previous studies have also explored the forest structure's effects on the productivity of the forest [Bohn and Huth, 2017; Dănescu et al., 2016; Liu et al., 2016; Schall et al., 2018], where they found that the main drivers of the productivity of forest are the variables that characterize the structure of the forest rather than the biodiversity-related variables. Though it is highly important to know the structure of the forest in order to understand its dynamics, there are still no available global forest structure maps yet. There are only a few coarse-resolution maps that are present, but these only show the components of the structure of forest (e.g., the height of a forest from MODIS and ICESat, resolution 1 km, Indeed, larger regions of multi-layered forest structure should be efficiently analyzed. Recent satellite missions have been (e.g., GEDI, ICESat2 sensor) and will be launched (e.g., BIOMASS, and Tandem-L) where new technologies will be used in order to measure, on a global scale, the structure of forest including its height and its ver-

tical heterogeneity. Nowadays, there are two main elements: the vertical and horizontal forest structures [Bohn and Huth, 2017; Cazcarra-Bes et al., 2017a; Getzin et al., 2012; Tello et al., 2018]. Finding a clear and suitable definition for forest structure is highly difficult. Furthermore, the metrics of forest structure differ depending on whether they are based either on remote sensing or on field data. The remote sensing-based descriptors often depend on the heterogeneous canopy structure for a given area; however, the field-based descriptors for the forest structure are derived from size measurements of each individual tree [Cazcarra-Bes et al., 2017a]. Terrestrial Laser Scanning (TLS) is a hybrid approach for forest structure, which is measured by both field and remote sensing data [Stovall and Shugart, 2018]. It gives highly detailed measurements for every single tree and for the forest canopy structure. TLS is the best replacement for plot-level inventory data in many systems. We note hereby that TLS cannot be considered as an alternative to large extent remote sensing techniques, but it is a critical component of calibration and validation of EO products. Therefore, in order to capture forest structure on a larger scale, either airborne or satellite-based remote sensing data could be suitable choices for this.

In our future studies, we are interested in using the forest modeling, LiDAR remote sensing, and airborne TomoSAR in order to be able to answer the question, “How can we estimate structure of a forest by using remote sensing, and what is the role played by forest structure in estimating the forest biomass and the above-ground wood productivity?” Our aim is to use the vertical and horizontal descriptors that can be measured by remote sensing in order to classify the forests into structural categories. Using this structural classification, we will explore if we will be able to estimate more accurately both forest biomass and above-ground wood productivity in case we included the structural information.

4.5 Conclusions

In this work, TomoSAR analysis has been applied for the estimation of the forests’ canopy height and terrain using L-band UAVSAR and P-band SETHI from AfriSAR data, collected over the Gabon Lopé Park on 2015 and 2016. Prior to tomographic imaging, a phase residual correction methodology based on phase calibration via phase center dou-

ble localization was implemented. The tomographic P- and L-band Capon profiles at different sections in the forests are validated in a good correlation with SFL LiDAR data CHM from the SFL data set as a reference. Second, the vertical profile of the vegetation at different sections in the Lopé using a Capon power estimator at HH, HV polarizations with IVIS Level 1B waveform LiDAR data, carried out over the OKO2 region in the Gabon Lopé National Park, was compared. The 3D profiles from Lidar waveform and from L- and P-band TomoSAR data show a high correlation. Finally, we report on the performance of forests' top height retrieved from the TomoSAR L-band and P-band data. Forests' top height from TomoSAR data that are estimated and validated with SFL data have an RMSE of 3.68 m for the L-band data. The RMSE value of P-band forest top height with respect to SFL was 3.02 m. The corresponding coefficient of determination was 0.95 and 0.93 for P- and L-band, respectively. Together, these results demonstrate the potential of TomoSAR to retrieve forest structure parameters. The development of tomographic SAR techniques allows for the reconstruction of the 3D radar reflectivity opening the door for 3D forest monitoring. As the link between physical forest structure and the reconstructed 3D radar reflectivity is still not understood and is far from being established, the 3D radar profiles obtained open prospects to derive algorithms that are able to link these profiles to the physical structure of the forest. For future work, we aim to provide an algorithm to estimate horizontal and vertical structure descriptors. These descriptors can be derived from TomoSAR data, which allow the characterization of the physical forest structure. Horizontal and vertical structure descriptors are crucial in boosting up the performance of biomass estimators. We hope that our results reinforce the scientific basis to estimate tropical forests' structure indices and give support for the upcoming biomass missions.

Part III

Land-subsidence monitoring using PS/DSInSAR technique

Comparison of multi temporal radar interferometry techniques using Sentinel-1: Lebanon case study

Contents

5.1	Introduction	115
5.2	Materials and Methods	118
5.3	Results	127
5.4	Discussion	132
5.5	Conclusion	134

5.1 Introduction

Land subsidence is a major hydro-geological hazard that affects our society [Ziegler et al., 2012; Dixon et al., 2006; Osmanoglu et al., 2011]. Differential Interferometric Synthetic Aperture Radar (DInSAR) is a powerful technique used to monitor and measure Earth’s surface deformations using SAR data. DInSAR exploits the phase information of at least two temporally separated SAR acquisitions acquired over the same area to form interferogram and measure the displacements and deformations occurred in the Earth’s surface.

An advanced approach of DInSAR is the Permanent Scatterer Interferometry (PSI) technique [Ferretti et al., 2000a, 2001, 2000b, 2003], such that the interferometry analysis is done on Permanent scatters (PS's) targets (like man-made structures, rocks, and other reflectors...), that have temporally stable phase and amplitude. PSI for the processing of multi-temporal SAR acquisitions is widely used to measure urban ground subsidence and has already shown its ability to map such phenomena on a large spatial scale with millimeters accuracy from space, associated with either ground subsidence [Stramondo et al., 2007, 2008; Tomás et al., 2010; Bell et al., 2012; Bovenga et al., 2012; Chaussard et al., 2013], railway subsidence [Luo et al., 2017], or landslides [Bru et al., 2017], etc. The first PSI technique is proposed by [Ferretti et al., 2000b,a]. Several contributions had followed PSI approach. The Small Baseline Subset technique (SBAS) [Berardino et al., 2002] is a major approach that extensively used in land surface monitoring using SAR data. Another approaches proposed by [Schmidt and Bürgmann, 2003] based on the generation of multi-look interferograms. The adaptation of LAMBDA method used in GPS to PSI approach is performed by [Kampes and Hanssen, 2004]. Hooper et al. [Hooper et al., 2004] proposed a new PSI method to monitor and analyze deformation in non-urban areas. A new SBAS algorithm was introduced by López-Quiroz et al. [López-Quiroz et al., 2009]. The extension of PSInSAR algorithm is proposed by [Ferretti et al., 2011] called SqueeSAR which based on using not only Permanent Scatters but also Distributed Scatters DS. Recently, a new PSI method is proposed by Devanthéry et al. [Devanthéry et al., 2014] based on what so-called Cousin PS's.

During the last two decades, the PSI and DInSAR have practiced a major development, this development mainly related to the ERS-1/2, Envisat and Radarsat missions that provide C-band data over a global scale. The progress accomplished by these missions is that the data covers a long-time period, this is the main warranty for developing algorithms able to monitor long-term deformations. The major step in PSI techniques is the launch of X-band sensors, where X-band data are sensitive to small displacements and variations [Luo et al., 2017; Bru et al., 2017]. The X-band data provides noticeable quality improvements of the time series analysis as compared to C-band data [Crosetto et al., 2010]. Recently, C-band Sentinel-1 satellite that launched on 3 April 2014, it acquires data at a global scale

in Terrain Observation with Progressive Scan (TOPS) mode [De Zan and Guarnieri, 2006]. Radar images acquired by Sentinel-1 offers an improved data acquisition capability with respect to the previous C-band sensors (ERS-1/2, Envisat and Radarsat), and increases the deformation monitoring potential. TOPS Sentinel-1A/1B (the standard mode of operation is Interferometric Wide Swath-IWS) acquires data over an area of 250 by 180 km with a re-visiting cycle of 6 days. Together, and with the additional advantage of sentinel-1 images that they are available free of charge to all data users, the Sentinel-1 coverage and revisit time is essential to PSI techniques over a wide area with high precision.

The goal of the chapter is to understand the performance of two novel techniques PSI and PS/DS using TOPS Sentinel-1. We demonstrate it in Lebanon to map their subsidence phenomena. Specifically, we investigate the ability of C-band SAR to determine ground subsidence phenomena in Lebanon based on Sentinel-1 data from 2015 to 2019. To estimate ground subsidence, we apply two methods. The first method is the standard PSI technique. Second, a Maximum Likelihood Estimator-based approach [Ho Tong Minh et al., 2015b], which exploits not only stable point-like scatters PS but also DS. The increased number of identified PS/DS measurement points on the ground resulting from this approach provide increased confidence in measurements of the ground's motion and displacement, compared to the previous algorithm based on PS only [Ferretti et al., 2001; Hooper et al., 2004].

The chapter is structured as follows: in the next section, the materials and methods are introduced. Results on ground subsidence in section 3 are then presented. while Section 4 provides an interpretation of the ground subsidence. Finally, conclusions are drawn in Section 5.

5.2 Materials and Methods

5.2.1 Interferometry

Interferometric Synthetic aperture radar (InSAR) is a remote sensing technique for extracting information about earth surface over the imaged area. InSAR approach is based on extracting the phase difference of at least two SLC images at a different time and slightly different SAR sensor positions [Gabriel et al., 1989; Massonnet and Feigl, 1998; Bamler and Hartl, 1998], to obtain what so-called the interferogram. SAR Interferogram is generated by multiplying, pixel by pixel, of two SAR SLC images, one with the complex conjugate of the another. Thus the interferogram generated has an amplitude equals to the product of the two SLC images amplitude and it has a phase equal to the phase difference between the two images. Below, the InSAR concepts are briefly summarized.

The SAR sensor acquires the SLC image from position M, measuring the phase to a single-pixel point target P at the ground. The phase of the first image to the target P is expressed as below:

$$\phi_M = \frac{4.\pi.MP}{\lambda} + \phi_{scatt_M} \quad (5.1)$$

Where MP is the distance between the sensor and the target, λ is the wavelength of the echo transmitted by SAR sensor, the factor 4π is related to the two way traveling path, from radar to target and then from target to radar. ϕ_{scatt_M} is the scattering matrix generated due to the interaction of SAR signals with the target P on the ground. It contains geometric information about the target. Consider ϕ_S the phase measured by the second image acquired by SAR sensor from position N,

$$\phi_N = \frac{4.\pi.NP}{\lambda} + \phi_{scatt_N} \quad (5.2)$$

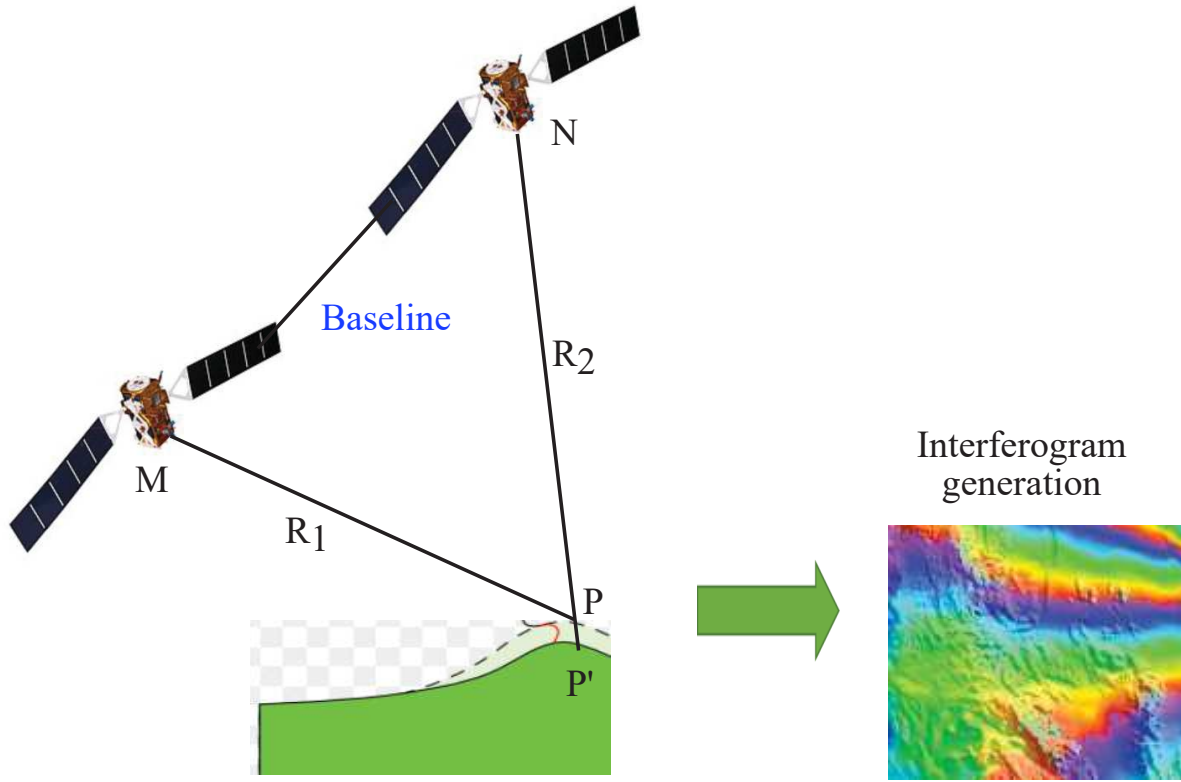


Figure 5.1 – InSAR basics.

By exploiting the phase difference between the two passes, the interferometric phase at point target P is expressed as:

$$\phi_N - \phi_M = \phi_{\text{int}} = \frac{NP - MP}{\frac{\lambda}{4\pi}} + \phi_{\text{scatt}_N} - \phi_{\text{scatt}_M} \quad (5.3)$$

ϕ_{int} is the interferometry phase, it contains information about the distance difference NP - MP required for Digital Elevation Model (DEM) extraction [Bamler and Hartl, 1998]. In order to model the displacement in the earth's surface, suppose that the point target

P moves to a position P' before acquiring the second SLC image, then the phase of the interferogram will be expressed as:

$$\phi_{\text{int}} = \frac{NP' - MP}{\frac{\lambda}{4\pi}} + \phi_{\text{scatt}_N} - \phi_{\text{scatt}_M} \quad (5.4)$$

Then by adding and subtracting the term $\frac{NP}{(\lambda/4\pi)}$, a new equation of the interferogram is obtained:

$$\phi_{\text{int}} = \frac{NP - MP}{\frac{\lambda}{4\pi}} + \frac{NP' - NP}{\frac{\lambda}{4\pi}} + \phi_{\text{scatt}_N} - \phi_{\text{scatt}_M} \quad (5.5)$$

Where the first term is the topographic term, the second term is the phase corresponds to the Line Of Sight (LOS) displacement in the surface at point target P'. Actually the above model is the simplified model of the interferogram phase. The more accurate model should contain phase terms related to the atmospheric delays and orbital errors [Massonnet and Feigl, 1998; Hanssen et al., 2001]. The interferogram phase can be written as:

$$\phi_{\text{int}} = \phi_{\text{Dis}} + \phi_{\text{topographic}} + \phi_{\text{Atm}_N} - \phi_{\text{Atm}_M} + \phi_{\text{orbital}_N} - \phi_{\text{orbital}_M} + \phi_{\text{Noise}} + 2.k.\pi \quad (5.6)$$

ϕ_{Dis} is the deformation phase, $\phi_{\text{topographic}}$ is the residual topographic phase, ϕ_{Noise} is the phase noise due to temporal decorrelation, mis-coregistration, uncompensated spectral shift decorrelation, orbital errors, and thermal noise. ϕ_{Atm_N} and ϕ_{Atm_M} is the atmospheric phase screen at different passes due to the propagation delay of the signal in the atmosphere. Here, it is necessary to mention the limitations and difficulties that face the extraction of the deformation phase from the interferogram phase. These limitations are: the temporal and geometric decorrelation that effect the ϕ_{Noise} term [Hanssen et al., 2001], the phase unwrapping problem that lead to estimate the phase cycles k [Ghiglia and Pritt, 1998], and the atmospheric phase term [Zebker et al., 1997].

The essential solution to separate the deformation phase from other phases is to analyze pixels that have small phase noise values. These pixels typically related to two types of targets: Permanent Scatterer (PS), where the backscattered signal is dominated by strong reflection and it is constant with time. Distributed scatters (DS), where the response of the backscattered signal is due to a spatially distributed object inside the resolution cell and it is constant over time.

5.2.2 PSI

Permanent Scatterer Interferometry (PSI) is a special class of InSAR techniques that uses multi-temporal tracks to minimize issues relative to atmospheric, spatial and temporal decorrelations to estimate ground deformations robustly. PS generally corresponds to man-made structure and other natural reflectors (rocks etc...) such that the reflected signals are constant with time.

The most important PSI technique is surely the one proposed by Ferretti et al. [Ferretti et al., 2000b, 2001], which was the first solution to select PS's and to separate the deformation and topographic phase residual from the APS, overcoming the geometrical and temporal decorrelations. The analysis is based on the selection of highly-coherent point-like targets that have temporal stable amplitude named PS [Ferretti et al., 2001]. These PS often corresponds to man-made structures or natural reflectors (like rocks...) and widely available in urban areas. The main limitation of this approach is that it is based on scatterers with high coherence, which leads to low PS's density in rural areas. Later on, Berardino et al. [Berardino et al., 2002] propose SBAS technique which is a complete PSI procedure using small baselines interferograms to limit the spatial decorrelation. SBAS approach uses a coherence based criterion, and multi-looked data to reduce phase noise. This approach provides increased sampling (spatial and temporal) with respect to the traditional PSI technique. However, this technique is not able to detect local deformation, then an extended SBAS version overcomes this limitation [Lanari et al., 2004]. Hooper et al. [Hooper et al., 2004] proposed a new approach for selecting PS based on not only on amplitude characteristics but on phase characteristics. This approach able to identify natural targets with low

amplitude as PS based on the phase stability of such targets. Followed by this work, the most used PSI packages are then developed, Stamps [Hooper and Zebker, 2007; Hooper, 2008].



Figure 5.2 – PS processing chain.

Here, a detailed steps of PSI processing chain that are discussed in details in Devanthéry et. al [Devanthéry et al., 2014]:

1- First of all, consider N SAR images acquired over an area of interest, generate M multi-look interferograms.

2- Estimate and remove the Atmospheric Phase Screens (APS) components. APS correction is performed by applying a set of Spatio-temporal filters [Ferretti et al., 2000b].

3- Estimate residual topographic phases and remove them from the interferogram phases.

4- Finally derive the deformation time series and calculate the deformation velocity using the phase model of the displacement (assuming constant velocity model):

$$\phi_{\text{disp}}^n = \frac{4 \cdot \pi \cdot t_n}{\lambda} \cdot v \quad (5.7)$$

Where v is the mean deformation LOS velocity of the target, and t_n is the temporal baseline.

In this work, the PS processing chain consists of two main stages. The first stage is the generation of the stack. ISCE tool is used here. First of all, starting from SLC images acquired over the area of interest, and orbital data at each date, the baselines are calculated concerning the common master. After that, the burst overlaps are extracted. Then mis-

registration is estimated for each pair of SLC's and the interferograms are generated. The final step is to merge the bursts.

The second stage is to use Stamps processing, after exporting the stack of interferograms generated by ISCE tool.

details on PSI processing

The PSI processing chain split into two workflows: 1) single master DInSAR processing using ISCE, and 2) the PSI processing using StaMPS.

The master image is selected from the beginning of the data series. Additionally, the overlap bursts inside the IW3 between the master scene and slaves must be selected. The next step involves the generation of all single interferograms. Then the final step is to convert DInSAR processing results into binary raster files compatible with StaMPS readers.

PSI work has been carried out using the InSAR Scientific Computing Environment (ISCE) and StaMPS software packages. The Interferometry processing chain can be created by run the stack generator. After running stack generator, run files will automatically be generated including different commands that generate the data-stack, coregister the stack, extract the overlap bursts between SAR images, calculate the average baseline. The next step after generating the stack is to make the single baseline stack and import it to stamps. It is necessary to mention that the atmospheric Phase Screen (APS) correction has been employed using the Toolbox for Reducing Atmospheric InSAR Noise (TRAIN) [Bekaert et al., 2015]. Gacos model correction was applied [Yu et al., 2017, 2018a,b]. Concerning the PS/DS processing chain, we will discuss it's workflow in the following paragraph.

5.2.3 PS/DS

Recently, the framework of InSAR processing in estimating residual topographic, APS and deformation phases typically based on using not only PS but also DS targets. Many studies were proposed to increase the density of measurement points over areas characterized by DS. These studies aim to preserve the quality of information behind the PS tech-

nique over deterministic targets. In other words, averaging the data over statistically homogeneous areas, and increasing Signal to Noise Ratio (SNR), without affecting the identification of coherent targets and without the need of phase unwrapping algorithms applied on hundreds of interferograms [Lanari et al., 2004]. Maximum Likelihood Estimation (MLE) frameworks act as an attempt to joint PS and DS processing [Ferretti et al., 2011, 2008; Rocca, 2007]. The main idea behind the MLE technique is to design a statistically-optimal estimator for parameters of interest, using the coherences of every interferogram in the stack. Recently, Ferretti et al. [Ferretti et al., 2011] proposed SqueeSAR algorithm. The main idea behind SqueeSAR is to process jointly PS with DS taking into account their different statistical behaviors. Unlike hybrid processing chains, where two or more algorithms are applied to the given data-stack, and the results are combined. SqueeSAR able to process jointly PS and DS without need for any significant change in the traditional PSI processing chain. Exploiting PS/DS processing chain is implemented in two steps: In the first step, the Maximum Likelihood Estimation (MLE) is used that jointly exploits all the $N(N-1)/2$ interferograms available from N images, in order to squeeze the best estimates of the $N-1$ interferometric phases, so-called linked phases. This step is termed Phase Linking or Phase Triangulation [Ferretti et al., 2011], in which the DS-linked phases can be modeled in the same way as a PS target. Once the first estimation step has yielded the estimates of the $N-1$ linked phases, the second step is required to separate the contributions of the decorrelation noises from the parameters of interest, as in PS processing.



Figure 5.3 – PS/DS processing chain

PS/DS processing chain is implemented here using were processed by the IRSTEA TomoSAR platform, which offers SAR, InSAR PS/DS, and Tomography processing [Minh et al., 2016]. In this work, the PS/DS processing chain in [Ho Tong Minh et al., 2015b] is adapted to the Sentinel-1 SAR stack.

detail PS/DS processing chain

1- Co-registration of the Sentinel-1 SLC stack. The slave images were resampled to a common master grid on 11 May 2015. SRTM Digital Elevation Model has been used to compensate for the topographic contribution.

2- Select the family of Statistically Homogeneous Pixels (SHP) by using Kolmogorov–Smirnov (KS) test [Ferretti et al., 2011] at each pixel.

3- Choose a certain threshold to define DS.

4- Estimate the coherence matrix at each DS.

5- Apply phase linking algorithm at each coherence matrix to squeeze the optimized phases.

6- Substitute the phase values of original SAR SLC images with their corresponding optimized values.

7- Apply the iterative algorithm to select PS/DS candidates.

8- At the end, process the PS/DS candidates jointly using PSI algorithms to estimate the deformation time series.

5.2.4 Detail processing from step 6 stamps

Results of the two processing chains were compared, in terms of capability, performance, the accuracy of the derived deformation velocity maps.

Using two different InSAR multi-temporal analysis, deformation velocity was estimated over Lebanon. In the following, the comparison of the two methods is performed.

PSI processing chain as described above is composed of successive steps applied on the Permanent scatters PS's selected. In this chapter, Stanford Method for Persistent Scatterers (Stamps) is used in PS processing. the brief description of Stamps steps is as follows.

Stamps is a software package that implements an InSAR persistent scatter PS method developed to work even in terrains devoid of man-made structures and/or undergoing

non-steady deformation. The first step after generating interferograms is to identify PS candidates. The level of decorrelation is defined whether pixels are PS or not, but the initial selection of PS candidates is done based on the amplitude dispersion along time series interferograms [Ferretti et al., 2001]. Then the phase noise will be estimated at each candidate. Based on the noise characteristics of each candidate, the PS's are selected. After that, the PS weeding is necessary to drop those that are due to signal contributions from neighboring ground elements and those deemed too noisy. The phase correction is carried out, The wrapped phase of the selected pixels is corrected for spatially-uncorrelated look angle (DEM) error. Then Phase unwrapping is carried out. After that, spatially-correlated look angle (SCLA) error is calculated which is due almost exclusively to spatially-correlated DEM error. The final step of the processing chain is atmospheric filtering.

Regarding PS/DS processing chain, the PSI steps including phase unwrapping, Estimate spatially-correlated look angle error, and atmospheric filtering are performed but not only on PS targets but also on DS targets. These steps are steps from 6 to 8 in the Stamps processing chain. Stamps steps from 6 to 8 are common between PS and PS/DS processing chains. A brief explanation of each step is presented below. The phase unwrapping is performed to unwrap 3D data that are irregularly sampled in two dimensions in order to unwrap InSAR PS time series, which are distributed irregularly in space. The third dimension is time. The process of phase unwrapping is to recover unambiguous phase values from phase data that are measured modulo 2π rad (wrapped data). Actually, the phase difference between neighboring PS's depends mainly on the number of cycles multiple of 2π . In order to unwrap correctly the phases, assume usually used that the sampling rate is high and aliasing is voided. In other words, the true absolute phase difference between two neighboring data points is generally less than π rad. The unwrapping problem is that not to allow the integration paths between two adjacent points when the absolute difference between the two is greater than π . The Snaphu software is used to unwrap the interferograms. The second step is to Estimate spatially-correlated look angle error. Spatially-Correlated Look Angle SCLA error is calculated which is due almost exclusively to spatially-correlated DEM error (this includes an error in the DEM itself, and incorrect mapping of the DEM into radar coordinates). The Master atmosphere and orbit error (AOE) phase are estimated si-

multaneously in this step. Finally, spatial filtering must be carried out to separate spatially correlated phase terms like atmospheric, and orbit error phase for each PS/DS candidate. In the end, the deformation velocity map can be generated.

5.3 Results

5.3.1 Lebanon site

Lebanon lies between the Mediterranean Sea one side, and Badiyat El-Sham (Syrian Desert, extension of the Arabian Desert to the north), and is influenced by this gradation over its entire length. The physical environment of Lebanon is dominated by its unique physiography and its position on the Mediterranean shores. Lebanon has two mountain ranges; Mount Lebanon which runs parallel to the sea (NNE-SSW) overlooking the narrow coastal plain and the Anti Lebanon range which runs on the eastern side, parallel to Mount Lebanon. The two mountain chains are separated by the elongated Bekaa plain. The coastal plain together with Mount Lebanon constitutes the occidental segment of Lebanon which makes up 50 % of the total area of the country and accommodate 70% of the Lebanese population (4.2 million persons) with a density of 400 persons/km². The oriental eastern segment is made up of the depression of the Bekaa valley (14%) and Anti-Lebanon ranges (36%). Many authors have described the topography of occidental Lebanon by showing a west-east profile through the country, thus revealing major topographic features of this segment. [Abdallah, 2007] divided the occidental Lebanon into the coastal plain, deeply incised valleys and highlands. [Sanlaville, 1977] ordered these surfaces as occidental segments constituted by the coastal plain, the plateaus at the coast, highly elevated region not exceeding 1500 m altitude, and high mountains. [Hakim, 1985] classified it as lower mountains (altitudes between 300-900 m), moderate mountains (altitudes between 900-1600 m) and elevated mountains (altitudes more than 1600 m). Referring to [Khawlie et al., 2002] and [Abdallah, 2007], the occidental and oriental segments of Lebanon can be divided into ten physio-graphic units depending on different altitudes and rock mass distribution.

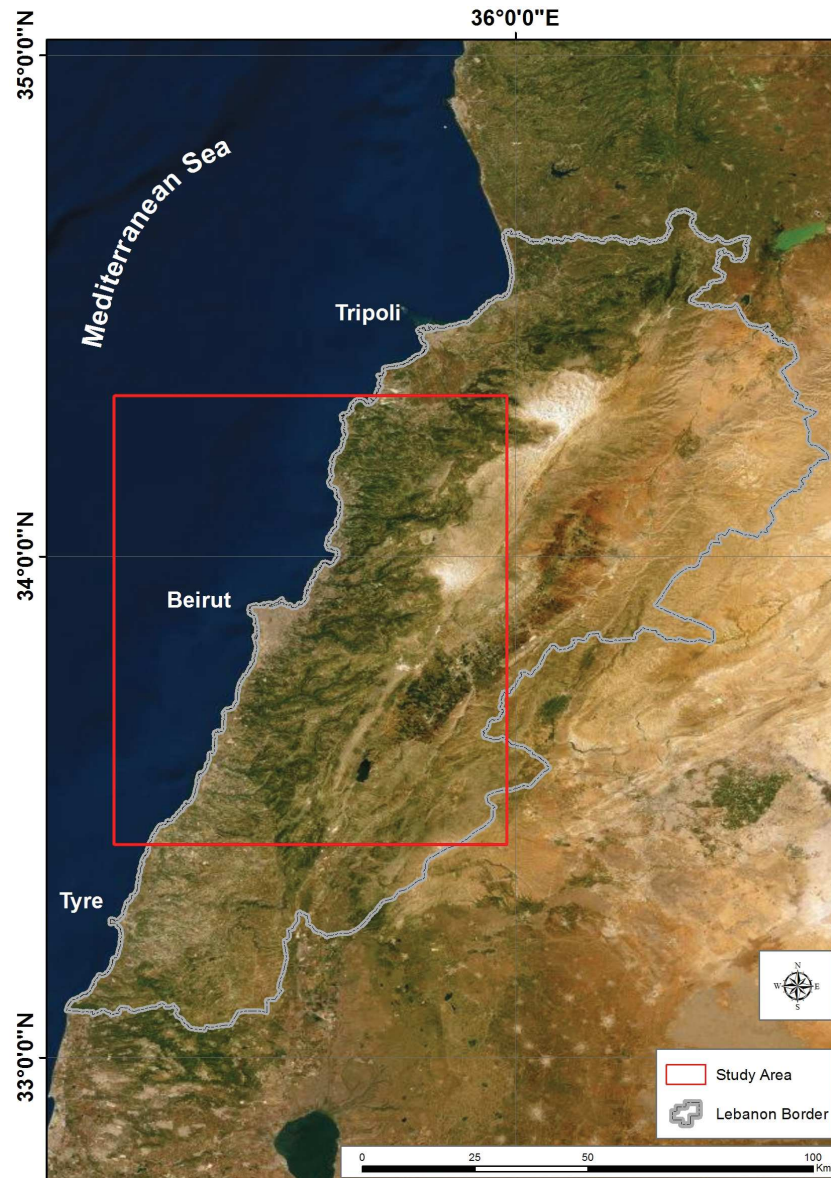


Figure 5.4 – Study area. The red polygon related to the area where Sentinel-1 data stack was processed.

Lebanon is part of the unstable shelf of the Eastern Mediterranean along the active transform border between the Levantine and Arabian plates, known as the Dead Sea Fault Zone (DSFZ). Mount Lebanon (coastal range) and Anti-Lebanon (inner range), which are arched and faulted horst geanticlines, can be considered as belts related with the restrain-

ing bend of the DSFZ. The Bekaa depression, on the other hand, is neither strictly a graben nor an elongated syncline, but possesses structural features of both [Sabagh, 1970; Beydoun, 1972]. These main features started during the Late Cretaceous where the collision zone was offshore and far to the NNW of Lebanon, which gave rise to the first gentle uplifting of Mount Lebanon and Anti-Lebanon area. Substantial uplift occurred in the Late Eocene and Oligocene resulting in the emergence and the marking out of the three fold NNE-SSW trending pattern of modern Lebanon. During the uplift time, the sea drained from the interior of the Bekaa depression and restricted to shallow marine incursions along the line of the present day coast. Since then, there has been continued uplift and local tilting over the last five million years and various block slides due to the strike-slip faulting. The anticline of Mount Lebanon reveals local folds distributed in its northern and eastern parts.

In addition to the major fault (Yammounah fault, central segment of DSFZ) that runs along the western margin of the Bekaa with a NNE-SSW strike and links the major fault of the Jordan valley to the Ghab valley fault of northern Syria, other faults are recognized in Mount Lebanon being almost vertical, with around 10-15 km length, and main strikes being NNE-SSW and NNW-SSE, with a less frequent E-W trend [Khawlie, 1995]. The northern part of Anti-Lebanon is similar to that of Mount Lebanon, though topographically lower. Eastward it is bounded by faults and partly merges into the folds of Damascus-Palmyra arc in Syria. The southern part, Jabal Hermon, is an elongate asymmetric anticlinal uplift cut by faults on both its flanks. Moreover, different faults of Lebanon are well developed locally in the following rock formations: J4, J6, C2b and C4; many of them characterized by relative small displacements (< 1 m) and showing dense spacing.

SAR data

The SAR stacks are consist of C-band Sentinel-1 data (10.0 m in azimuth and ground range) acquired in TOPS acquisition mode for the period 2015-2019. The processing of SAR Sentinel-1 stack requires very accurate images cor-registration, this due to TOPS imaging mode and it's sensitivity to geometric errors. It is worth noting that the exclusion of rainy days was performed. The Sentinel-1 data-set is comprised of 118 Single Look Complex

(SLC) data covers the whole study area. The analysis is done on Sentinel-1A and 1B, the revisit time of the descending orbit is 6 days. This temporal resolution is sufficient given the expected magnitude of ground displacements and the availability of a large number of acquisitions over the area of interests. It should be noted that the Sentinel-1 products are not spatially synchronized, so that their starting and ending times may vary within each orbits. Sentinel-1 SLC Level1 products are acquired in TOPS mode, it consists of 3 sub swaths named IW1, IW2, and IW3. Each sub swath is composed of 9 bursts. For the interferometric processing, the Advanced Land Observation Satellite (ALOS) World 3D (AW3D30) Digital Surface Model (DSM) [Takaku et al., 2016], of 30 m spatial resolution, was utilized.

5.3.2 PS results

Using PSI processing chain, subsidence map was generated using Sentinel-1 images acquired over Lebanon between 11 May 2015 and 26 May 2019. More than 1475650 measurement points were identified within an area of about 3922 km². Assuming that most of the measured deformation corresponds to vertical displacement of the earth's surface due to subsidence, the vertical displacement through straightforward geometrical arguments can be estimated.

5.3.3 PS/DS results

Sentinel-1 images acquired over Lebanon between 11 May 2015 and 26 May 2019 was treated by PS/DS processing chain. More than 2541960 measurement points were identified within an area of about 3922 km². It is necessary to mention that measurement points here are greater than those identified using PS processing chain. The location of the reference point that is chosen for interferometric analysis is between Longitude 35.5300 35.540 and Latitude 33.89 33.9.

Interferograms and Gacos data

The unwrapped interferograms at 6 dates are shown in Figure 5.5. The master date was chosen to be at 11 May 2015. All interferograms are being processed with respect to the master.

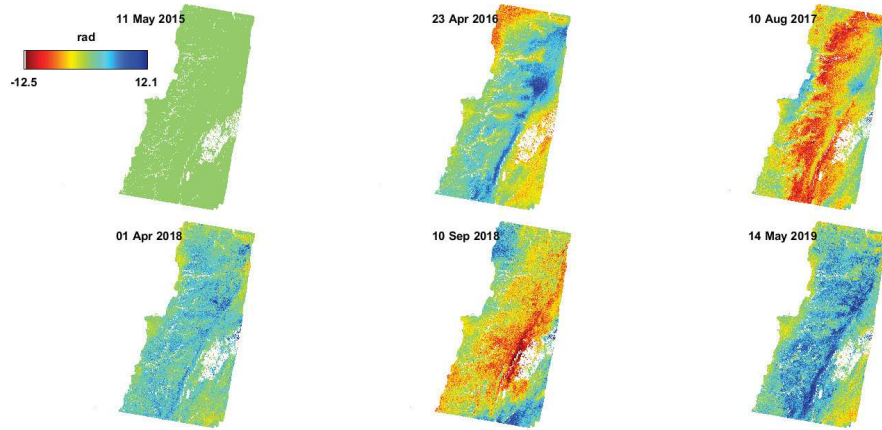


Figure 5.5 – Interferograms generated by PS/DS processing chain at different dates.

Gacos atmospheric correction [Yu et al., 2018a,b, 2017] was applied to the InSAR results. The Gacos phase model for atmospheric correction is shown in Figure 5.6.

Deformation velocity

The Line of Sight (LOS) deformation velocity map generated using two processing chains PS and PS/DS is shown in Figure 5.7. The area where the velocity map has been estimated is located between 33.4 and 34.32 Latitude and between 35.3 and 36 Longitude. There are no displacements detected at the coastal areas. It can be seen that there are many subsidence hot-spots. The areas in the North East part are affected by a deformation about 11.8 mm/year. Another subsidence area is detected near Qaroun Lake located in the south of the country.

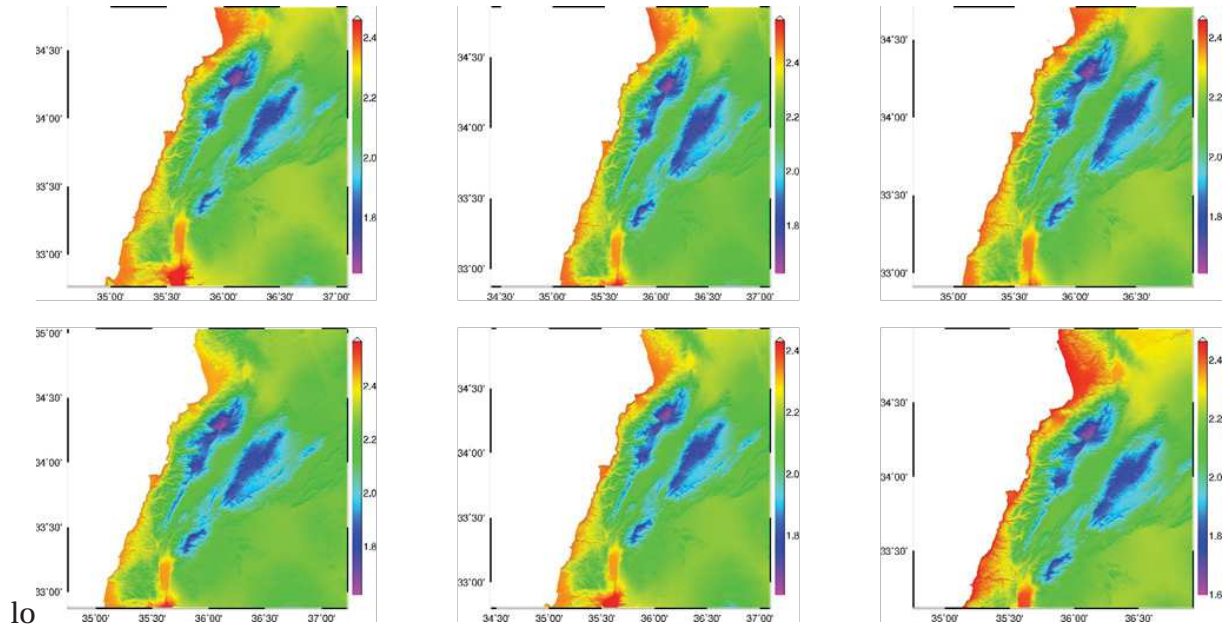


Figure 5.6 – Gacos model for atmospheric phase at different dates.

5.4 Discussion

In this work, first, PSI processing chain is implemented to generate subsidence map taking Lebanon as a case study. Second, PS and DS targets have been jointly processed and used to generate subsidence map for Lebanon. This is done by using Copernicus Sentinel-1 mission data acquired over our study area with fine temporal resolution.

5.4.1 Sentinel-1

The new Sentinel 1 satellites launched by European Space Agency provides open remotely sensed data and high precision and temporal resolution. Sentinel-1 constellation is the only satellite system providing dense time series with global coverage with 6 days revisit time. The constellation of Sentinel-1, which is characterized by small baselines and then low geometric decorrelations allows to have enough numbers of identified PS and DS.

5.4.2 Deformation velocity

Subsidence map has been generated using the PS processing chain applied on Sentinel-1 data acquired over Lebanon for the period between 2015 and 2019.

Ground subsidence has been estimated using PS/DS processing chain for the period between 2015 and 2019 in Lebanon. The number of PS/DS measurement points are larger than those identified by PS processor. Thus the resulting subsidence map contains much more measurement points than the traditional PS processing chain. A statistical analysis has been carried out on the two generated subsidence map. These analysis consists of mean, standard deviation, and mean of velocities at each geological class (Table. 5.1 and Table. 5.3)

5.4.3 Phase calibration via phase center double localization

Orbital errors are considered to be a limitation for InSAR time series techniques. Orbital errors propagate into InSAR LOS and lead to uncertainty in measuring accurately the ground displacements.

Spaceborne SAR systems are usually provided with orbital state vectors which give the sensor position in centimeters precision. The orbital product information is obtained after processing different auxiliary data, such as Global Positioning System, attitude information from the satellite's sensors, and physical model parameters [Wermuth et al., 2009]. The orbital product information is necessary for SAR image formation and thus for interferometry processing. Any disturbances in the orbit will lead to residuals that corrupt further SAR image processing.

Our prospects to this work are to implement phase calibration of spaceborne SAR data to compensate for orbital and baseline errors and correct the SAR data. This will enhance the InSAR results.

5.5 Conclusion

In this chapter, we demonstrated the feasibility of ground subsidence estimates by C-band SAR taking Lebanon as a case study. Using PS and PS/DS techniques, we measured the average velocity of the ground subsidence. A deformation velocity map was generated taking a part of Lebanon as a case study. It is noticed the performance of the PS/DS technique in terms of the number of measurement point that is much larger than those identified by PS approach. The PS/DS technique applied to InSAR appears to be a promising approach for using C-band SAR data to monitor ground surface risks. The results on ground subsidence 2015-2019 (by C-band Sentinel-1), in Lebanon described consistently the subsidence area based on InSAR analysis. Our prospects for this work is to generate the subsidence map for the whole country using ERS, ENVISAT, and Sentinel-1 data. These maps should be carried out after applying phase calibration of SAR data and compensate for the baseline errors.

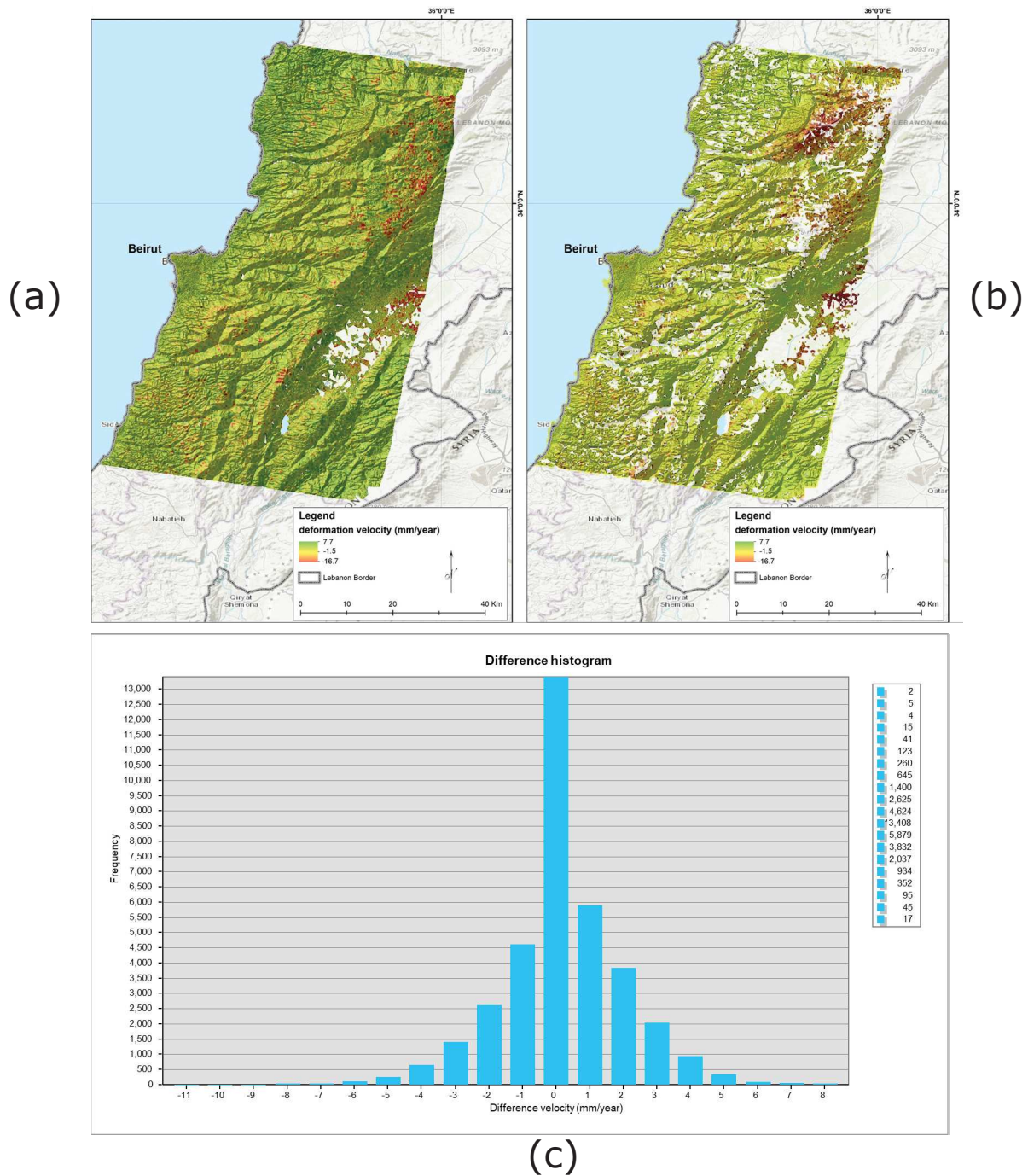


Figure 5.7 – (a) Deformation velocity map using PS/DS processing chain. (b) Deformation velocity map using PS processing chain. (c) Difference velocity histogram between PS velocity and PS/DS velocity.

Table 5.1 – PS results statistics.

Geology	Count(pixels)	Area(m ²)	Mean(mm)	Std(mm)
bc2	183	14965479.74	-3.213115	1.544758
bc2b	24	1962685.867	-2.583333	1.187317
qj	5	408892.889	-2.4	1.496663
qm	6	490671.4668	-2.166667	0.687184
ql	1296	105985036.8	-2.083333	2.682102
bj6	392	32057202.5	-1.691327	1.301148
qe	533	43587981.97	-1.538462	1.615161
qcp	23	1880907.29	-1.521739	1.528556
qc	23	1880907.29	-1.521739	1.55674
a	6	490671.4668	-1.5	1.258306
terrain decolle	4	327114.3112	-1.5	1.118034
ce	4	327114.3112	-1.25	0.829156
c2a	975	79734113.36	-1.202051	1.43766
qtl	10	817785.7781	-1.1	0.943398
mm	33	2698693.068	-1.060606	0.693668
j6	6179	505309832.3	-1.050655	1.098274
c4	11852	969239704.2	-1.022528	1.279824
c1	2152	175987499.4	-1.015335	1.248883
mcg	11	899564.3559	-1	0.953463
c2b	1488	121686523.8	-0.875672	1.285778
j7	208	17009944.18	-0.865385	0.925677
ebouli	96	7850743.47	-0.802083	1.06673
e2	349	28540723.65	-0.793696	1.020065
c3	1706	139514253.7	-0.709848	1.20554
e2b	1670	136570224.9	-0.593413	0.919166
cone de dejection	14	1144900.089	-0.571429	1.049781
m2b	133	10876550.85	-0.533835	0.930267
bc1	21	1717350.134	-0.47619	1.005653
qf	63	5152050.402	-0.47619	0.709508
ml	245	20035751.56	-0.453061	1.262828
c6	1499	122586088.1	-0.439626	1.067841
m2a	48	3925371.735	-0.4375	0.733321
e2a	378	30912302.41	-0.433862	0.971616
qa	56	4579600.357	-0.410714	1.03124
caillouti de pente	10	817785.7781	-0.4	1.113553
qd	52	4252486.046	-0.384615	0.76344
qt	308	25187801.96	-0.363636	0.870275
qdd	334	27314044.99	-0.314371	0.796683
qdm	214	17500615.65	-0.280374	0.829304
urbanism	17	1390235.823	-0.235294	0.876451
c1-2a	34	2780471.645	-0.205882	0.631497
qla	78	6378729.069	-0.153846	0.508314
ml1	397	32466095.39	-0.13602	1.093437
j5	62	5070271.824	-0.064516	0.534939
bp	172	14065915.38	-0.052326	0.649369
j1-3a	2	163557.1556	0	0
j6a	2	163557.1556	0	0
t	1	81778.57781	0	0
m2	98	8014300.625	0.030612	0.691849
j4	1099	89874657.01	0.073703	0.779065
c5	952	77853206.07	0.091387	0.838322
q	17	1390235.823	0.176471	0.512812
qat	65	5315607.558	0.184615	1.036151
qds	4	327114.3112	0.25	0.433013
qaf	8	654228.6225	0.375	0.695971
cp	26	2126243.023	0.384615	0.624926
ad	1	81778.57781	1	0

Table 5.2 – DS results statistics.

Geology	Count(pixels)	Area(m ²)	Mean(mm)	Std(mm)
ql	2176	177950185.3	-2.266085	2.164101
qcp	25	2044464.445	-2.16	1.869331
a	20	1635571.556	-2.15	1.768474
terrain decolle	4	327114.3112	-1.75	0.829156
c3	2065	168872763.2	-1.461985	1.693352
ebouli	135	11040108	-1.437037	1.523191
j6	7195	588396867.3	-1.415288	1.568502
c2b	1871	153007719.1	-1.414751	1.630835
mcg	10	817785.7781	-1.4	1.74356
c2a	1269	103777015.2	-1.371946	1.553471
c4	15449	1263397249	-1.344747	1.979863
bc2	267	21834880.27	-1.344569	1.593878
qds	3	245335.7334	-1.333333	1.247219
qtl	30	2453357.334	-1.333333	1.534782
j7	295	24124680.45	-1.318644	1.46374
c1	3013	246398854.9	-1.308994	1.526546
bj6	467	38190595.84	-1.297645	1.524691
bc1	38	3107585.957	-1.289474	1.393743
qe	691	56508997.27	-1.257598	1.80454
mm	30	2453357.334	-1.2	1.301281
bc2b	37	3025807.379	-1.054054	1.859177
qc	25	2044464.445	-1.04	1.561538
t	2	163557.1556	-1	1
e2	403	32956766.86	-0.940447	1.331589
urbanism	17	1390235.823	-0.882353	1.131493
e2b	1831	149736576	-0.872747	1.530564
e2a	489	39989724.55	-0.770961	1.48912
qdd	309	25269580.54	-0.68932	1.09156
qm	14	1144900.089	-0.642857	1.287697
ce	5	408892.889	-0.6	1.2
qd	51	4170707.468	-0.588235	1.013177
c6	1910	156197083.6	-0.572775	1.608776
qt	322	26332702.05	-0.559006	1.282199
ml1	450	36800360.01	-0.557778	1.518038
qdm	205	16764608.45	-0.512195	1.128823
cone de dejection	17	1390235.823	-0.411765	2.568104
bp	170	13902358.23	-0.388235	1.275047
ml	327	26741594.94	-0.385321	1.279633
m2b	131	10712993.69	-0.358779	1.132913
qf	65	5315607.558	-0.292308	1.309411
m2a	51	4170707.468	-0.27451	1.387316
c1-2a	34	2780471.645	-0.235294	1.214104
qj	29	2371578.756	-0.206897	2.090691
j5	65	5315607.558	-0.2	0.914835
qa	79	6460507.647	-0.189873	1.510101
q	17	1390235.823	-0.117647	1.231085
j4	1084	88647978.34	-0.106089	1.231056
j1-3a	2	163557.1556	0	0
ad	3	245335.7334	0	0.816497
m2	116	9486315.026	0.025862	1.012518
qla	103	8423193.514	0.07767	1.12076
c5	1175	96089828.92	0.110638	1.544136
qaf	9	736007.2003	0.111111	1.286204
cp	31	2535135.912	0.419355	1.040291
qat	82	6705843.38	0.902439	1.33991
caillouti _d ep _{ente}	53	736007.2003	-0.333333	0.942809
j6a	1	81778.57781	2	0

Table 5.3 – Geological classes.

Geology	Combination
bn	Basalt
dune mouvant	Marine
ml1	conglomerate
a	Fluvial
ad	Marine
bc	pyroclastic
bc1	Pyroclastic
bc2	pyroclastic
bc2b	pyroclastic
bj	Basalt
bj5	basalt
bj6	basalt
bp	basalt
c1	Sandstone
c1-2	limestone
c1-2a	sandstone
c2	Limestone
c2a	Limestone
c2b	limestone
c3	Shale
c3a	marl
c4	Limestone
c5	Marl
c6	marne
cailloutis des pentes	colluvial
cone de deject	Colluvial
coulet _d e _b oue	Fluvial
e2a	Marl
e2b	Limestone
eboulie	colluvial
m	conglomerat
m2	Conglomerate
m2a	Conglomerate
mcg	conglomerate
ml	Marl
mud	fluvial
q	Colluvial
qcg	Conglomerate
qd	marine
qf	Alluvial
qf1	fluvial
qtl	Fluvial



General Conclusion

This thesis has considered the use of remote sensing of natural scenarios through multiple baseline SAR acquisitions. The general objective of the dissertation is to exploit SAR multibaseline algorithms and applications in forests and urban areas. Our research required different spaceborne and airborne data sets that have been acquired over different sites. Considering the multibaseline SAR system as a 3D imaging tool for the portion of the Earth's surface into which the transmitted wave penetrates has allowed providing a unified treatment of different kinds of analysis.

The accomplished achievements carried out through the first part of the thesis are that the TomoSAR technique ability to derive dense forest structure is evaluated at L- and P-band. Even though, the phase screens due to propagation disturbances have been shown to constitute a crucial issue as well in multi-baseline applications, either interferometric and tomographic. Thus, different phase calibration techniques were applied and validated. However, a drawback within these techniques is that using SKP, we assessed the ability of L-band data to penetrate tropical forest from the canopy down to ground layer, so that we can extract the digital terrain model under the forest. While using the PCDL technique, only phase calibration is carried out after removing phase residuals from the original SLC, this done without the extraction of the terrain phase. Super-resolution beam-

forming techniques have been implemented to have perfect tomographic profiles. For L and P-band TomoSAR data, we identified the different forest layers (canopy and ground layer) in such a way one can derive forest structure indices that enhance the performance of biomass estimators.

Regarding the second part, different multi-temporal time series InSAR techniques were evaluated. Land subsidence map is generated taking Lebanon as a case study. The feasibility of Sentinel-1 C-band data to estimate ground subsidence is demonstrated. PS/DS technique appears promise technique to monitor ground surface risks. We need in the future, to combine the InSAR technique with insitu measurements in a useful way to monitor and track the ground subsidence in Lebanon. There are many differential GPS stations located in Lebanon at different sites of the country. So our future work in this part is to generate the GPS vertical and horizontal displacements history. After that, the correlation between InSAR measurements and GPS measurements can be carried out. To improve the quality of InSAR results, we propose to implement phase calibration of Multibaseline Sentinel-1 data using PCDL applied on DS, in such a way we can eliminate the orbital errors and phase disturbance from the InSAR data.

TomoSAR perspectives

As perspectives regarding the first part, our aim is to estimate the structure indices of the forest such as the horizontal and the vertical indices that play a role in supporting the biomass recovery algorithms and improving the forest management activities. However, the structure of the forest is considered as an important factor in its ecology because of its correlation with various ecological processes [[Pretzsch et al., 2010](#); [Shugart et al., 2010](#); [Mundell et al., 2010](#)]. Moreover, it has a role as an indicator in the detection of biodiversity, where the forests with vertical structures can enhance a certain biodiversity taxa [[Boncina, 2000](#); [Ishii et al., 2004](#); [Schall et al., 2018](#)]. Also, either the vertical or the horizontal structural heterogenicity can be able to improve the forest ecosystem resistance to disturbances [[Dobbertin, 2005](#); [Pretzsch et al., 2016](#)]. Though it is highly important to know the forest structure in order to be able to understand its dynamics. Finding an appropriate and a

clear definition for forest structure is really very difficult. Furthermore, forest structure parameters vary based on the method of their foundation either data on the ground or remote sensing. Field descriptors of forest structure are often derived from the measurements of the size of each tree individually, however, remote sensing descriptors depend on the heterogeneity in structure of the canopy of a given area. Our interest in the future studies is in using the forest modeling, LiDAR remote sensing, and airborne tomoSAR in order to be able to reply to the question, remote sensing, and what is the role played by the forest in the estimation of forest biomass and surface wood productivity? Our goal is to use the vertical and the horizontal descriptors that can be measured by remote sensing in order to classify the forests into structural categories. Using this structural classification, we will examine whether we will be able to more accurately estimate the forest biomass and the surface wood productivity in case we include the structural information.

InSAR perspectives

Typically, space SAR systems are equipped with state vector systems which give the sensor a position of centimeters of precision. Information on the orbital products is attained after processing various auxiliary data, such as the attitude information of the satellite sensors, the ephemeris of the global positioning system and the parameters of the model physical [Wermuth et al., 2009]. Getting information on the orbital products is highly necessary for the formation of SAR images and thus for the interferometry treatment. Any disturbances that happen in the orbit will cause residues which corrupt SAR image processing. Our prospect for this work is to implement the phase calibration of spatial SAR data to compensate for orbital and basic errors and correct SAR data. This will help in improving InSAR's results.



Bibliography

Nasa land, vegetation, and ice sensor (lvis), afrisar gabon2016 data release oct 2016. [https://lvis.gsfc.nasa.gov/data_sets/2016gabon/LVIS – Gabon – AfriSAR – data – release.pdf](https://lvis.gsfc.nasa.gov/data_sets/2016gabon/LVIS%20Gabon%20AfriSAR%20data%20release.pdf). Cited page 81.

Chadi Abdallah. *Application of remote sensing and geographical information system for the study of mass movements in Lebanon*. PhD thesis, Université Pierre et Marie Curie-Paris VI, 2007. Cited page 127.

Nico Adam, Bert Kampes, Michael Eineder, Jirathana Worawattanamateekul, and Michaela Kircher. The development of a scientific permanent scatterer system. In *ISPRS Workshop High Resolution Mapping from Space, Hannover, Germany*, volume 2003, 2003. Cited page 49.

Esteban Aguilera, Matteo Nannini, and Andreas Reigber. Wavelet-based compressed sensing for sar tomography of forested areas. *IEEE Transactions on Geoscience and Remote Sensing*, 51(12):5283–5295, 2013. Cited page 86.

Falk Amelung, Devin L Galloway, John W Bell, Howard A Zebker, and Randell J Laczniaik. Sensing the ups and downs of las vegas: Insar reveals structural control of land subsidence and aquifer-system deformation. *Geology*, 27(6):483–486, 1999. Cited page 47.

- N Baghdadi, R Cresson, Mohammad El Hajj, R Ludwig, and Isabelle La Jeunesse. Estimation of soil parameters over bare agriculture areas from c-band polarimetric sar data using neural networks. *Hydrology and Earth System Sciences*, 16:p–1607, 2012. Cited page [62](#).
- J David Ballester-Berman, Juan Manuel López-Sánchez, and Joaquim Fortuny-Guasch. Retrieval of biophysical parameters of agricultural crops using polarimetric sar interferometry. *IEEE Transactions on Geoscience and Remote Sensing*, 43(4):683–694, 2005. Cited page [62](#).
- Richard Bamler and Philipp Hartl. Synthetic aperture radar interferometry. *Inverse problems*, 14(4):R1, 1998. Cited pages [21](#), [34](#), [118](#), and [119](#).
- A Beaudoin, T Le Toan, S Goze, E Nezry, A Lopes, E Mougin, CC Hsu, HC Han, JA Kong, and RT Shin. Retrieval of forest biomass from sar data. *International Journal of Remote Sensing*, 15(14):2777–2796, 1994. Cited page [86](#).
- DPS Bekaert, RJ Walters, TJ Wright, AJ Hooper, and DJ Parker. Statistical comparison of insar tropospheric correction techniques. *Remote Sensing of Environment*, 170:40–47, 2015. Cited page [123](#).
- John W Bell, Falk Amelung, and Christopher D Henry. Insar analysis of the 2008 renomogul earthquake swarm: Evidence for westward migration of walker lane style dextral faulting. *Geophysical Research Letters*, 39(18), 2012. Cited page [116](#).
- Paolo Berardino, Gianfranco Fornaro, Riccardo Lanari, and Eugenio Sansosti. A new algorithm for surface deformation monitoring based on small baseline differential sar interferograms. *IEEE Transactions on Geoscience and Remote Sensing*, 40(11):2375–2383, 2002. Cited pages [49](#), [57](#), [116](#), and [121](#).
- KM Bergen, SJ Goetz, RO Dubayah, GM Henebry, CT Hunsaker, ML Imhoff, RF Nelson, GG Parker, and VC Radeloff. Remote sensing of vegetation 3-d structure for biodiversity and habitat: review and implications for lidar and radar spaceborne missions. *Journal of Geophysical Research: Biogeosciences*, 114(G2), 2009. Cited page [86](#).

- Z Beydoun. A new evaluation of the petroleum prospects of lebanon with special reference to the pre-jurassic. *18th Arab Pet. Cong., Algeria*, 1972. Cited page [129](#).
- Wolfgang-Martin Boerner. Applications of polarimetric sar. Cited pages [47](#) and [62](#).
- Friedrich J Bohn and Andreas Huth. The importance of forest structure to biodiversity–productivity relationships. *Royal Society open science*, 4(1):160521, 2017. Cited pages [96](#), [109](#), and [110](#).
- Andrej Boncina. Comparison of structure and biodiversity in the rajhenav virgin forest remnant and managed forest in the dinaric region of slovenia. *Global Ecology and Biogeography*, 9(3):201–211, 2000. Cited pages [29](#), [109](#), and [140](#).
- F Bovenga, J Wasowski, DO Nitti, R Nutricato, and MT Chiaradia. Using cosmo/skymed x-band and envisat c-band sar interferometry for landslides analysis. *Remote Sensing of Environment*, 119:272–285, 2012. Cited page [116](#).
- Guadalupe Bru, Pablo J González, Rosa M Mateos, Francisco J Roldán, Gerardo Herrera, Marta Béjar-Pizarro, and José Fernández. A-dinsar monitoring of landslide and subsidence activity: A case of urban damage in arcos de la frontera, spain. *Remote Sensing*, 9(8):787, 2017. Cited page [116](#).
- Astor Toraño Caicoya, Matteo Pardini, Irena Hajnsek, and Konstantinos Papathanassiou. Forest above-ground biomass estimation from vertical reflectivity profiles at l-band. *IEEE Geoscience and Remote Sensing Letters*, 12(12):2379–2383, 2015. Cited page [86](#).
- Victor Cazcarra-Bes, Maria Tello-Alonso, Rico Fischer, Michael Heym, and Konstantinos Papathanassiou. Monitoring of forest structure dynamics by means of l-band sar tomography. *Remote Sensing*, 9(12):1229, 2017a. Cited pages [95](#) and [110](#).
- Victor Cazcarra-Bes, Maria Tello-Alonso, Rico Fischer, Michael Heym, and Konstantinos Papathanassiou. Monitoring of forest structure dynamics by means of l-band sar tomography. *Remote Sensing*, 9(12):1229, 2017b. Cited page [62](#).

- Estelle Chaussard, Falk Amelung, Hasanudin Abidin, and Sang-Hoon Hong. Sinking cities in indonesia: Alos palsar detects rapid subsidence due to groundwater and gas extraction. *Remote Sensing of Environment*, 128:150–161, 2013. Cited page [116](#).
- Shane R Cloude. Dual-baseline coherence tomography. *IEEE Geoscience and Remote Sensing Letters*, 4(1):127–131, 2007. Cited pages [35](#) and [87](#).
- Shane R Cloude. Multifrequency 3-d imaging of tropical forest using polarization coherence tomography. In *7th European Conference on Synthetic Aperture Radar*, pages 1–4. VDE, 2008. Cited page [87](#).
- Shane R Cloude and Konstantinos P Papathanassiou. Polarimetric sar interferometry. *IEEE Transactions on geoscience and remote sensing*, 36(5):1551–1565, 1998. Cited pages [21](#), [35](#), [62](#), and [86](#).
- Shane R Cloude and Eric Pottier. A review of target decomposition theorems in radar polarimetry. *IEEE transactions on geoscience and remote sensing*, 34(2):498–518, 1996. Cited pages [21](#) and [35](#).
- Shane R Cloude and Eric Pottier. An entropy based classification scheme for land applications of polarimetric sar. *IEEE transactions on geoscience and remote sensing*, 35(1):68–78, 1997. Cited pages [21](#) and [35](#).
- SR Cloude and KP Papathanassiou. Three-stage inversion process for polarimetric sar interferometry. *IEE Proceedings-Radar, Sonar and Navigation*, 150(3):125–134, 2003. Cited page [86](#).
- C Colesanti, F De Zan, Alessandro Ferretti, CLAUDIO Prati, and Fabio Rocca. Generation of dem with sub-metric vertical accuracy from 30’ers-envisat pairs. In *Proc. FRINGE 2003 Workshop, Frascati, Italy*, pages 1–5, 2003. Cited pages [22](#) and [36](#).
- M Crosetto, O Monserrat, N Adam, A Parizzi, C Bremmer, S Dortland, RF Hanssen, and FJ van Leijen. Final report of the validation of existing processing chains in terrafirma stage 2. terrafirma project, esrin. *Contract*, (19366/05), 2008. Cited page [49](#).

- M Crosetto, O Monserrat, R Iglesias, and B Crippa. Persistent scatterer interferometry. *Photogrammetric Engineering & Remote Sensing*, 76(9):1061–1069, 2010. Cited page [116](#).
- John C Curlander and Robert N McDonough. Synthetic aperture radar- systems and signal processing(book). *New York: John Wiley & Sons, Inc, 1991.*, 1991. Cited pages [20](#) and [34](#).
- Mauro Mariotti d’Alessandro and Stefano Tebaldini. Phenomenology of p-band scattering from a tropical forest through three-dimensional sar tomography. *IEEE Geoscience and Remote Sensing Letters*, 9(3):442–446, 2012. Cited pages [48](#) and [63](#).
- Mauro Mariotti d’Alessandro, Stefano Tebaldini, and Fabio Rocca. Phenomenology of ground scattering in a tropical forest through polarimetric synthetic aperture radar tomography. *IEEE Transactions on Geoscience and Remote Sensing*, 51(8):4430–4437, 2013. Cited page [54](#).
- Adrian Dănescu, Axel T Albrecht, and Jürgen Bauhus. Structural diversity promotes productivity of mixed, uneven-aged forests in southwestern germany. *Oecologia*, 182(2): 319–333, 2016. Cited page [109](#).
- Francesco De Zan and A Monti Guarnieri. Topsar: Terrain observation by progressive scans. *IEEE Transactions on Geoscience and Remote Sensing*, 44(9):2352–2360, 2006. Cited page [117](#).
- Núria Devanthéry, Michele Crosetto, Oriol Monserrat, María Cuevas-González, and Bruno Crippa. An approach to persistent scatterer interferometry. *Remote Sensing*, 6(7):6662–6679, 2014. Cited pages [116](#) and [122](#).
- Timothy H Dixon, Falk Amelung, Alessandro Ferretti, Fabrizio Novali, Fabio Rocca, Roy Dokka, Giovanni Sella, Sang-Wan Kim, Shimon Wdowinski, and Dean Whitman. Space geodesy: Subsidence and flooding in new orleans. *Nature*, 441(7093):587, 2006. Cited page [115](#).
- Matthias Dobbertin. Tree growth as indicator of tree vitality and of tree reaction to environmental stress: a review. *European Journal of Forest Research*, 124(4):319–333, 2005. Cited pages [29](#), [109](#), and [140](#).

- Jason B Drake, Ralph O Dubayah, David B Clark, Robert G Knox, J Bryan Blair, Michelle A Hofton, Robin L Chazdon, John F Weishampel, and Steve Prince. Estimation of tropical forest structural characteristics using large-footprint lidar. *Remote Sensing of Environment*, 79(2-3):305–319, 2002. Cited page [62](#).
- Ralph O Dubayah, SL Sheldon, David B Clark, MA Hofton, J Bryan Blair, George C Hurtt, and Robin L Chazdon. Estimation of tropical forest height and biomass dynamics using lidar remote sensing at la selva, costa rica. *Journal of Geophysical Research: Biogeosciences*, 115(G2), 2010. Cited page [62](#).
- Ibrahim El Moussawi, Dinh Ho Tong Minh, Nicolas Baghdadi, Chadi Abdallah, Jalal Jomaah, Olivier Strauss, and Marco Laval. L-band uavsar tomographic imaging in dense forests: Gabon forests. *Remote Sensing*, 11(5):475, 2019. Cited page [98](#).
- Paolo Ferrazzoli, Simonetta Paloscia, Paolo Pampaloni, Giovanni Schiavon, Simone Sigismondi, and Domenico Solimini. The potential of multifrequency polarimetric sar in assessing agricultural and arboreous biomass. *IEEE Transactions on Geoscience and Remote Sensing*, 35(1):5–17, 1997. Cited page [62](#).
- Alessandro Ferretti, Claudio Prati, and Fabio Rocca. Nonlinear subsidence rate estimation using permanent scatterers in differential sar interferometry. *IEEE Transactions on Geoscience and Remote Sensing*, 38(5):2202–2212, 2000. Cited pages [51](#), [53](#), and [54](#).
- A Ferretti, C Prati, and F Rocca. Non-uniform motion monitoring using the permanent scatterers technique. *FRINGE'99: Advancing ERS SAR Interferometry from Applications towards Operations*, 2000a. Cited page [116](#).
- Alessandro Ferretti, Claudio Prati, and Fabio Rocca. Nonlinear subsidence rate estimation using permanent scatterers in differential sar interferometry. *IEEE Transactions on geoscience and remote sensing*, 38(5):2202–2212, 2000b. Cited pages [116](#), [121](#), and [122](#).
- Alessandro Ferretti, Claudio Prati, and Fabio Rocca. Permanent scatterers in sar interferometry. *IEEE Transactions on geoscience and remote sensing*, 39(1):8–20, 2001. Cited pages [27](#), [49](#), [116](#), [117](#), [121](#), and [126](#).

- Alessandro Ferretti, Claudio Prati, and Fabio Rocca. Process for radar measurements of the movement of city areas and landsliding zones, June 24 2003. US Patent 6,583,751. Cited page [116](#).
- Alessandro Ferretti, Fabrizio Novali, Francesco de Zan, Claudio Prati, and Fabio Rocca. Moving from ps to slowly decorrelating targets: A prospective view. In *7th European Conference on Synthetic Aperture Radar*, pages 1–3. VDE, 2008. Cited page [124](#).
- Alessandro Ferretti, Alfio Fumagalli, Fabrizio Novali, Claudio Prati, Fabio Rocca, and Alessio Rucci. A new algorithm for processing interferometric data-stacks: Squeesar. *IEEE Transactions on Geoscience and Remote Sensing*, 49(9):3460–3470, 2011. Cited pages [49](#), [52](#), [57](#), [116](#), [124](#), and [125](#).
- Rico Fischer, Nikolai Knapp, Friedrich Bohn, Herman H Shugart, and Andreas Huth. The relevance of forest structure for biomass and productivity in temperate forests: new perspectives for remote sensing. *Surveys in Geophysics*, pages 1–26, 2019. Cited page [86](#).
- Alexander G Fore, Bruce D Chapman, Brian P Hawkins, Scott Hensley, Cathleen E Jones, Thierry R Michel, and Ronald J Muellerschoen. Uavsar polarimetric calibration. *IEEE Transactions on Geoscience and Remote Sensing*, 53(6):3481–3491, 2015. Cited page [66](#).
- Gianfranco Fornaro and Francesco Serafino. Imaging of single and double scatterers in urban areas via sar tomography. *IEEE Transactions on Geoscience and Remote Sensing*, 44(12):3497–3505, 2006. Cited pages [35](#) and [50](#).
- Gianfranco Fornaro, Fabrizio Lombardini, and Francesco Serafino. Three-dimensional multipass sar focusing: Experiments with long-term spaceborne data. *IEEE Transactions on Geoscience and Remote Sensing*, 43(4):702–714, 2005. Cited page [87](#).
- Gianfranco Fornaro, Fabrizio Lombardini, and Francesco Serafino. Multidimensional imaging with ers data. In *Fringe 2005 Workshop*, volume 610, 2006. Cited page [50](#).
- Giorgio Franceschetti and Riccardo Lanari. *Synthetic aperture radar processing*. CRC press, 2018. Cited pages [20](#) and [34](#).

- Anthony Freeman. Fitting a two-component scattering model to polarimetric sar data from forests. *IEEE Transactions on Geoscience and Remote Sensing*, 45(8):2583–2592, 2007. Cited pages [21](#), [35](#), and [62](#).
- Othmar Frey and Erich Meier. Analyzing tomographic sar data of a forest with respect to frequency, polarization, and focusing technique. *IEEE Transactions on Geoscience and Remote Sensing*, 49(10):3648–3659, 2011. Cited page [86](#).
- Stephen Frolking, Michael W Palace, DB Clark, Jeffrey Q Chambers, HH Shugart, and George C Hurtt. Forest disturbance and recovery: A general review in the context of spaceborne remote sensing of impacts on aboveground biomass and canopy structure. *Journal of Geophysical Research: Biogeosciences*, 114(G2), 2009. Cited page [86](#).
- Andrew K Gabriel and Richard M Goldstein. Crossed orbit interferometry: theory and experimental results from sir-b. *International Journal of Remote Sensing*, 9(5):857–872, 1988. Cited pages [21](#) and [35](#).
- Andrew K Gabriel, Richard M Goldstein, and Howard A Zebker. Mapping small elevation changes over large areas: differential radar interferometry. *Journal of Geophysical Research: Solid Earth*, 94(B7):9183–9191, 1989. Cited pages [21](#), [35](#), and [118](#).
- Franck Garestier, Pascale C Dubois-Fernandez, Dominique Guyon, and Thuy Le Toan. Forest biophysical parameter estimation using l-and p-band polarimetric sar data. *IEEE Transactions on Geoscience and Remote Sensing*, 47(10):3379–3388, 2009. Cited page [86](#).
- Guido Gatti, Stefano Tebaldini, Mauro Mariotti d’Alessandro, and Fabio Rocca. Algae: A fast algebraic estimation of interferogram phase offsets in space-varying geometries. *IEEE Transactions on Geoscience and Remote Sensing*, 49(6):2343–2353, 2011. Cited pages [55](#) and [69](#).
- LV Gatti, M Gloor, JB Miller, CE Doughty, Y Malhi, LG Domingues, LS Basso, A Martinewski, CSC Correia, VF Borges, et al. Drought sensitivity of amazonian carbon balance revealed by atmospheric measurements. *Nature*, 506(7486):76, 2014. Cited page [86](#).

- Stephan Getzin, Kerstin Wiegand, and Ingo Schöning. Assessing biodiversity in forests using very high-resolution images and unmanned aerial vehicles. *Methods in ecology and evolution*, 3(2):397–404, 2012. Cited page [110](#).
- Dennis C Ghiglia and Mark D Pritt. *Two-dimensional phase unwrapping: theory, algorithms, and software*, volume 4. Wiley New York, 1998. Cited pages [49](#) and [120](#).
- Fulvio Gini, Fabrizio Lombardini, and Monica Montanari. Layover solution in multibaseline sar interferometry. *IEEE Transactions on Aerospace and Electronic Systems*, 38(4):1344–1356, 2002a. Cited page [72](#).
- Fulvio Gini, Fabrizio Lombardini, and Monica Montanari. Layover solution in multibaseline sar interferometry. *IEEE Transactions on Aerospace and Electronic Systems*, 38(4):1344–1356, 2002b. Cited pages [35](#), [87](#), and [94](#).
- Scott Goetz, Daniel Steinberg, Ralph Dubayah, and Bryan Blair. Laser remote sensing of canopy habitat heterogeneity as a predictor of bird species richness in an eastern temperate forest, usa. *Remote Sensing of Environment*, 108(3):254–263, 2007. Cited page [86](#).
- John Grace. Understanding and managing the global carbon cycle. *Journal of Ecology*, 92(2):189–202, 2004. Cited page [86](#).
- A Monti Guarnieri and C Prati. Ers-envisat combination for interferometry and super-resolution. In *ERSENVISAT Symposium (Gothenburg, Sweden)*, volume 1222, 2000. Cited pages [22](#) and [36](#).
- A Monti Guarnieri and Stefano Tebaldini. Hybrid cramér-rao bounds for crustal displacement field estimators in sar interferometry. *IEEE signal processing letters*, 14(12):1012–1015, 2007. Cited page [57](#).
- A Monti Guarnieri, P Guccione, P Pasquali, and YL Desnos. Multi-mode envisat asar interferometry: techniques and preliminary results. *IEE Proceedings-Radar, Sonar and Navigation*, 150(3):193–200, 2003. Cited pages [22](#) and [36](#).

- Andrea Monti Guarnieri and Stefano Tebaldini. On the exploitation of target statistics for sar interferometry applications. *IEEE Transactions on Geoscience and Remote Sensing*, 46(11):3436–3443, 2008. Cited pages [52](#) and [57](#).
- B Hakim. Hydrological and hydrochemical research on some mediterranean karsts lebanon, syria, and morocco. *Publications of the Lebanese University, Beirut Lebanon*, 6, 1985. Cited page [127](#).
- Forrest G Hall, Kathleen Bergen, James B Blair, Ralph Dubayah, Richard Houghton, George Hurtt, Josef Kelldorfer, Michael Lefsky, Jon Ranson, Sasan Saatchi, et al. Characterizing 3d vegetation structure from space: Mission requirements. *Remote Sensing of Environment*, 115(11):2753–2775, 2011. Cited page [86](#).
- RF Hanssen, PJG Teunissen, and P Joosten. Phase ambiguity resolution for stacked radar interferometric data. In *Proc KIS2001, international symposium on kinematic systems in geodesy, Geomatics and Navigation, Banff*, pages 317–320, 2001. Cited pages [49](#) and [120](#).
- Scott Hensley, Kevin Wheeler, Greg Sadowy, Cathleen Jones, Scott Shaffer, Howard Zebker, Tim Miller, Brandon Heavey, Ernie Chuang, Roger Chao, et al. The uavsar instrument: Description and first results. In *Radar Conference, 2008. RADAR'08. IEEE*, pages 1–6. IEEE, 2008. Cited page [66](#).
- Dinh Ho Tong Minh, Thuy Le Toan, Fabio Rocca, Stefano Tebaldini, Mauro Mariotti d'Alessandro, and Ludovic Villard. Relating p-band synthetic aperture radar tomography to tropical forest biomass. *IEEE Transactions on Geoscience and Remote Sensing*, 52(2):967–979, 2014. Cited pages [55](#) and [87](#).
- Dinh Ho Tong Minh, Thuy Le Toan, Stefano Tebaldini, Fabio Rocca, and Lorenzo Ianini. Assessment of the p-and l-band sar tomography for the characterization of tropical forests. In *2015 IEEE International Geoscience and Remote Sensing Symposium (IGARSS)*, pages 2931–2934. IEEE, 2015a. Cited pages [23](#), [37](#), [87](#), and [93](#).

- Dinh Ho Tong Minh, Le Van Trung, Thuy Toan, et al. Mapping ground subsidence phenomena in ho chi minh city through the radar interferometry technique using alos pal-sar data. *Remote Sensing*, 7(7):8543–8562, 2015b. Cited pages [27](#), [117](#), and [124](#).
- Dinh Ho Tong Minh, Thuy Le Toan, Fabio Rocca, Stefano Tebaldini, Ludovic Villard, Maxime Réjou-Méchain, Oliver L Phillips, Ted R Feldpausch, Pascale Dubois-Fernandez, Klaus Scipal, et al. Sar tomography for the retrieval of forest biomass and height: Cross-validation at two tropical forest sites in french guiana. *Remote Sensing of Environment*, 175:138–147, 2016. Cited pages [50](#), [63](#), [68](#), [87](#), and [94](#).
- Ho Tong Minh, D, T. Le Toan, F. Rocca, S. Tebaldini, L. Villard, M. Réjou-Méchain, and J. Chave. Sar tomography for the retrieval of forest biomass and height: Cross-validation at two tropical forest sites in french guiana. *Remote Sensing of Environment*, 175:138–147, 2017. Cited pages [63](#), [71](#), and [72](#).
- Ho Tong Minh, Dinh, T. Le Toan, F. Rocca, S. Tebaldini, M. M. d'Alessandro, and L. Villard. Relating p-band synthetic aperture radar tomography to tropical forest biomass. *IEEE Transactions on Geoscience and Remote Sensing*, 52(2):967–979, 2014. Cited pages [63](#), [69](#), [72](#), and [82](#).
- Ho Tong Minh, Dinh, Thuy Le Toan, Stefano Tebaldini, Fabio Rocca, and Lorenzo Iannini. Assessment of the p-and l-band sar tomography for the characterization of tropical forests. In *Geoscience and Remote Sensing Symposium (IGARSS), 2015 IEEE International*, pages 2931–2934. IEEE, 2015a. Cited pages [63](#) and [80](#).
- Ho Tong Minh, Dinh, Thuy Le Toan, Stefano Tebaldini, Fabio Rocca, and Lorenzo Iannini. Assessment of the p-and l-band sar tomography for the characterization of tropical forests. In *Geoscience and Remote Sensing Symposium (IGARSS), 2015 IEEE International*, pages 2931–2934. IEEE, 2015b. Cited page [63](#).
- Dirk H Hoekman, Martin AM Vissers, and Thanh N Tran. Unsupervised full-polarimetric sar data segmentation as a tool for classification of agricultural areas. *IEEE Journal of Selected Topics in Applied Earth Observations and Remote Sensing*, 4(2):402–411, 2011. Cited page [62](#).

- Andrew Hooper. A multi-temporal insar method incorporating both persistent scatterer and small baseline approaches. *Geophysical Research Letters*, 35(16), 2008. Cited page [122](#).
- Andrew Hooper and Howard A Zebker. Phase unwrapping in three dimensions with application to insar time series. *JOSA A*, 24(9):2737–2747, 2007. Cited page [122](#).
- Andrew Hooper, Howard Zebker, Paul Segall, and Bert Kampes. A new method for measuring deformation on volcanoes and other natural terrains using insar persistent scatterers. *Geophysical research letters*, 31(23), 2004. Cited pages [27](#), [49](#), [116](#), [117](#), and [121](#).
- Yue Huang, Laurent Ferro-Famil, and Andreas Reigber. Under-foliage object imaging using sar tomography and polarimetric spectral estimators. *IEEE transactions on geoscience and remote sensing*, 50(6):2213–2225, 2012. Cited page [87](#).
- Jordi Inglada, J-C Souyris, Caroline Henry, and Céline Tison. Incoherent sar polarimetric analysis over point targets. *IEEE Geoscience and Remote Sensing Letters*, 3(2):246–249, 2006. Cited pages [21](#) and [35](#).
- Hiroaki T Ishii, Shin-ichi Tanabe, and Tsutomu Hiura. Exploring the relationships among canopy structure, stand productivity, and biodiversity of temperate forest ecosystems. *Forest Science*, 50(3):342–355, 2004. Cited pages [29](#), [109](#), and [140](#).
- Bert M Kampes and Ramon F Hanssen. Ambiguity resolution for permanent scatterer interferometry. *IEEE Transactions on Geoscience and Remote Sensing*, 42(11):2446–2453, 2004. Cited pages [49](#) and [116](#).
- M Khawlie, M Awad, A Shaban, R Bou Kheir, and C Abdallah. Remote sensing for environmental protection of the eastern mediterranean rugged mountainous areas, lebanon. *ISPRS Journal of Photogrammetry and Remote Sensing*, 57(1-2):13–23, 2002. Cited page [127](#).
- Mohamad R Khawlie. Fault-controlled eastern mediterranean coast, lebanon: Geological contribution to coastal management. *Coastal management*, 23(1):41–55, 1995. Cited page [129](#).

- Herbert J Kramer. *Observation of the Earth and its Environment: Survey of Missions and Sensors*. Springer Science & Business Media, 2002. Cited page [62](#).
- Gerhard Krieger, Alberto Moreira, Manfred Zink, Irena Hajnsek, Sigurd Huber, Michelangelo Villano, Konstantinos Papathanassiou, Marwan Younis, P Lopez Dekker, Matteo Pardini, et al. Tandem-l: Main results of the phase a feasibility study. In *2016 IEEE International Geoscience and Remote Sensing Symposium (IGARSS)*, pages 2116–2119. IEEE, 2016. Cited page [87](#).
- Florian Kugler, Seung-Kuk Lee, Irena Hajnsek, and Konstantinos P Papathanassiou. Forest height estimation by means of pol-insar data inversion: The role of the vertical wavenumber. *IEEE Transactions on Geoscience and Remote Sensing*, 53(10):5294–5311, 2015. Cited page [63](#).
- Riccardo Lanari, Oscar Mora, Michele Manunta, Jordi J Mallorquí, Paolo Berardino, and Eugenio Sansosti. A small-baseline approach for investigating deformations on full-resolution differential sar interferograms. *IEEE Transactions on Geoscience and Remote Sensing*, 42(7):1377–1386, 2004. Cited pages [49](#), [121](#), and [124](#).
- Marco Lavalley, Brian Hawkins, and Scott Hensley. Tomographic imaging with uavsar: Current status and new results from the 2016 afrisar campaign. In *Geoscience and Remote Sensing Symposium (IGARSS), 2017 IEEE International*, pages 2485–2488. IEEE, 2017. Cited page [64](#).
- Thuy Le Toan, S Quegan, MWJ Davidson, Heiko Balzter, Philippe Paillou, K Papathanassiou, S Plummer, F Rocca, S Saatchi, H Shugart, et al. The biomass mission: Mapping global forest biomass to better understand the terrestrial carbon cycle. *Remote sensing of environment*, 115(11):2850–2860, 2011. Cited page [87](#).
- J Lee. Forest-savanna dynamics and the origins of marantaceae forest in central gabon. *African rain forest ecology and conservation: An interdisciplinary perspective*, page 165, 2001. Cited page [89](#).

- Michael A Lefsky, Warren B Cohen, Geoffrey G Parker, and David J Harding. Lidar remote sensing for ecosystem studies: Lidar, an emerging remote sensing technology that directly measures the three-dimensional distribution of plant canopies, can accurately estimate vegetation structural attributes and should be of particular interest to forest, landscape, and global ecologists. *AIBS Bulletin*, 52(1):19–30, 2002. Cited page [62](#).
- C Liu, PW Vachon, and GW Geling. Improved ship detection with airborne polarimetric sar data. *Canadian Journal of Remote Sensing*, 31(1):122–131, 2005. Cited page [62](#).
- Yi-Yun Liu, Yang Wang, Timothy R Walsh, Ling-Xian Yi, Rong Zhang, James Spencer, Yohei Doi, Guobao Tian, Baolei Dong, Xianhui Huang, et al. Emergence of plasmid-mediated colistin resistance mechanism mcr-1 in animals and human beings in china: a microbiological and molecular biological study. *The Lancet infectious diseases*, 16(2):161–168, 2016. Cited page [109](#).
- Penélope López-Quiroz, Marie-Pierre Doin, Florence Tupin, Pierre Briole, and Jean-Marie Nicolas. Time series analysis of mexico city subsidence constrained by radar interferometry. *Journal of Applied Geophysics*, 69(1):1–15, 2009. Cited page [116](#).
- Yunling Lou, Scott Hensley, Brian Hawkins, Cathleen Jones, Marco Lavallo, Thierry Michel, Delwyn Moller, Ron Muellerschoen, Naiara Pinto, Xiaoqing Wu, et al. Uavsar program: Recent upgrades to support vegetation structure studies and land ice topography mapping. In *Geoscience and Remote Sensing Symposium (IGARSS), 2017 IEEE International*, pages 5893–5895. IEEE, 2017. Cited page [61](#).
- Qingli Luo, Guoqing Zhou, and Daniele Perissin. Monitoring of subsidence along jingjin inter-city railway with high-resolution terrasars-x mt-insar analysis. *Remote Sensing*, 9(7):717, 2017. Cited page [116](#).
- Didier Massonnet and Kurt L Feigl. Radar interferometry and its application to changes in the earth’s surface. *Reviews of geophysics*, 36(4):441–500, 1998. Cited pages [118](#) and [120](#).

- Didier Massonnet and Freysteinn Sigmundsson. Remote sensing of volcano deformation by radar interferometry from various satellites. *Remote sensing of active volcanism*, pages 207–221, 2000. Cited page [47](#).
- Didier Massonnet, Marc Rossi, César Carmona, Frédéric Adragna, Gilles Peltzer, Kurt Feigl, and Thierry Rabaute. The displacement field of the landers earthquake mapped by radar interferometry. *Nature*, 364(6433):138, 1993. Cited page [47](#).
- Didier Massonnet, Helene Vadon, and C Carmona. Ers-1 internal clock drift measured by interferometry. *IEEE transactions on geoscience and remote sensing*, 33(2):401–408, 1995. Cited page [51](#).
- Franz Meyer, Bert Kampes, Richard Bamler, and Juergen Fischer. Methods for atmospheric correction in insar data. In *Fringe 2005 Workshop*, volume 610, 2006. Cited page [49](#).
- D Ho Tong Minh, Yen-Nhi Ngo, Nicolas Baghdadi, and Pierre Maurel. Tomosar platform: a new irstea service as demand for sar, interferometry, polarimetry and tomography. In *ESA Living Planet Symposium 2016; Proceedings of*, pages 1–8, 2016. Cited page [124](#).
- Oscar Mora, Jordi J Mallorqui, and Antoni Broquetas. Linear and nonlinear terrain deformation maps from a reduced set of interferometric sar images. *IEEE Transactions on Geoscience and Remote Sensing*, 41(10):2243–2253, 2003. Cited page [49](#).
- J Mundell, STEVEN J Taff, MA Kilgore, and SA Snyder. Using real estate records to assess forest land parcelization and development: A minnesota case study. *Landscape and Urban Planning*, 94(2):71–76, 2010. Cited pages [29](#), [109](#), and [140](#).
- Maxim Neumann, Laurent Ferro-Famil, and Andreas Reigber. Estimation of forest structure, ground, and canopy layer characteristics from multibaseline polarimetric interferometric sar data. *IEEE Transactions on Geoscience and Remote Sensing*, 48(3):1086–1104, 2010. Cited page [86](#).
- Batuhan Osmanoglu, Timothy H Dixon, Shimon Wdowinski, Enrique Cabral-Cano, and Yan Jiang. Mexico city subsidence observed with persistent scatterer insar. *International*

- Journal of Applied Earth Observation and Geoinformation*, 13(1):1–12, 2011. Cited page [115](#).
- Yude Pan, Richard A Birdsey, Jingyun Fang, Richard Houghton, Pekka E Kauppi, Werner A Kurz, Oliver L Phillips, Anatoly Shvidenko, Simon L Lewis, Josep G Canadell, et al. A large and persistent carbon sink in the world’s forests. *Science*, page 1201609, 2011. Cited page [61](#).
- Konstantinos P Papathanassiou and Shane R Cloude. Single-baseline polarimetric sar interferometry. *IEEE Transactions on Geoscience and Remote Sensing*, 39(11):2352–2363, 2001. Cited pages [21](#), [35](#), and [62](#).
- Matteo Pardini and K Papathanassiou. Sub-canopy topography estimation: Experiments with multibaseline sar data at l-band. In *2012 IEEE International Geoscience and Remote Sensing Symposium*, pages 4954–4957. IEEE, 2012. Cited page [86](#).
- Gilles Peltzer and Paul Rosen. Surface displacement of the 17 may 1993 eureka valley, california, earthquake observed by sar interferometry. *Science*, 268(5215):1333–1336, 1995. Cited page [47](#).
- Antonio Pepe and Riccardo Lanari. On the extension of the minimum cost flow algorithm for phase unwrapping of multitemporal differential sar interferograms. *IEEE Transactions on Geoscience and remote sensing*, 44(9):2374–2383, 2006. Cited page [49](#).
- Antonio Pepe, Leonardo Daniel Euillades, Michele Manunta, and Riccardo Lanari. New advances of the extended minimum cost flow phase unwrapping algorithm for sbas-dinsar analysis at full spatial resolution. *IEEE Transactions on Geoscience and Remote Sensing*, 49(10):4062–4079, 2011. Cited page [49](#).
- Daniele Perissin and Alessandro Ferretti. Urban-target recognition by means of repeated spaceborne sar images. *IEEE Transactions on Geoscience and Remote Sensing*, 45(12):4043–4058, 2007. Cited page [49](#).

- Daniele Perissin and Teng Wang. Repeat-pass sar interferometry with partially coherent targets. *IEEE Transactions on Geoscience and Remote Sensing*, 50(1):271–280, 2011. Cited pages [22](#) and [36](#).
- Emanuela Pichelli, Rossella Ferretti, Domenico Cimini, Giulia Panegrossi, Daniele Perissin, Nazzareno Pierdicca, Fabio Rocca, and Bjorn Rommen. Insar water vapor data assimilation into mesoscale model mm5: Technique and pilot study. *IEEE Journal of Selected Topics in Applied Earth Observations and Remote Sensing*, 8(8):3859–3875, 2015. Cited page [54](#).
- CLAUDIO Prati, Fabio Rocca, and AM Guarnieri. Effects of speckle and additive noise on the altimetric resolution of interferometric sar (isar) surveys. In *12th Canadian Symposium on Remote Sensing Geoscience and Remote Sensing Symposium*, volume 4, pages 2469–2472. IEEE, 1989. Cited pages [22](#) and [35](#).
- H Pretzsch, M Del Río, G Schütze, Ch Ammer, P Annighöfer, A Avdagic, I Barbeito, K Bielak, G Brazaitis, L Coll, et al. Mixing of scots pine (*pinus sylvestris* l.) and european beech (*fagus sylvatica* l.) enhances structural heterogeneity, and the effect increases with water availability. *Forest Ecology and Management*, 373:149–166, 2016. Cited pages [29](#), [109](#), and [140](#).
- Hans Pretzsch, Jochen Dieler, Rainer Matyssek, and Philip Wipfler. Tree and stand growth of mature norway spruce and european beech under long-term ozone fumigation. *Environmental Pollution*, 158(4):1061–1070, 2010. Cited pages [29](#), [109](#), and [140](#).
- Bernhard Rabus, Michael Eineder, Achim Roth, and Richard Bamler. The shuttle radar topography mission—a new class of digital elevation models acquired by spaceborne radar. *ISPRS journal of photogrammetry and remote sensing*, 57(4):241–262, 2003. Cited pages [22](#) and [36](#).
- A. Reigber, A. Moreira. First demonstration of airborne sar tomography using multibaseline l-band data. *IEEE Transactions on Geoscience and Remote Sensing*, 38(5):2142–2152, 2000. Cited pages [62](#) and [63](#).

- Andreas Reigber and Alberto Moreira. First demonstration of airborne sar tomography using multibaseline l-band data. *IEEE Transactions on Geoscience and Remote Sensing*, 38(5):2142–2152, 2000. Cited pages [48](#), [50](#), [86](#), and [87](#).
- Fabio Rocca. Synthetic aperture radar: A new application for wave equation techniques. *Stanford Exploration Project*, 56:167–189, 1987. Cited pages [20](#) and [34](#).
- Fabio Rocca. Modeling interferogram stacks. *IEEE Transactions on Geoscience and Remote Sensing*, 45(10):3289–3299, 2007. Cited page [124](#).
- E Rodriguez and JM Martin. Theory and design of interferometric synthetic aperture radars. In *IEE Proceedings F (Radar and Signal Processing)*, volume 139, pages 147–159. IET, 1992. Cited pages [21](#) and [35](#).
- Paul A Rosen, Scott Hensley, Ian R Joughin, Fuk K Li, Soren N Madsen, Ernesto Rodriguez, and Richard M Goldstein. Synthetic aperture radar interferometry. *Proceedings of the IEEE*, 88(3):333–382, 2000. Cited pages [21](#) and [34](#).
- Georges Sabagh. State of the art vii: The demography of the middle east. *Review of Middle East Studies*, 4(2):1–19, 1970. Cited page [129](#).
- Paul Sanlaville. *Etude géomorphologique de la région littorale du Liban*, volume 1. Université libanaise, 1977. Cited page [127](#).
- Stefan Sauer, Laurent Ferro-Famil, Andreas Reigber, and Eric Pottier. Multibaseline polinsar analysis of urban scenes for 3d modeling and physical feature retrieval at l-band. In *2007 IEEE International Geoscience and Remote Sensing Symposium*, pages 1098–1101. IEEE, 2007. Cited pages [35](#) and [87](#).
- Peter Schall, Martin M Gossner, Steffi Heinrichs, Markus Fischer, Steffen Boch, Daniel Prati, Kirsten Jung, Vanessa Baumgartner, Stefan Blaser, Stefan Böhm, et al. The impact of even-aged and uneven-aged forest management on regional biodiversity of multiple taxa in european beech forests. *Journal of Applied Ecology*, 55(1):267–278, 2018. Cited pages [29](#), [109](#), and [140](#).

- David A Schmidt and Roland Bürgmann. Time-dependent land uplift and subsidence in the santa clara valley, california, from a large interferometric synthetic aperture radar data set. *Journal of Geophysical Research: Solid Earth*, 108(B9), 2003. Cited page [116](#).
- CC Schmullius and DL Evans. Review article synthetic aperture radar (sar) frequency and polarization requirements for applications in ecology, geology, hydrology, and oceanography: A tabular status quo after sir-c/x-sar. *International Journal of Remote Sensing*, 18(13):2713–2722, 1997. Cited page [62](#).
- ESA Sentinel. User handbook, 2013. Cited page [44](#).
- HH Shugart, S Saatchi, and FG Hall. Importance of structure and its measurement in quantifying function of forest ecosystems. *Journal of Geophysical Research: Biogeosciences*, 115(G2), 2010. Cited pages [29](#), [109](#), and [140](#).
- Thomas A Spies. Forest structure: a key to the ecosystem. *Northwest science*, 72:34–36, 1998. Cited page [85](#).
- Petre Stoica, Randolph L Moses, et al. Spectral analysis of signals. 2005a. Cited page [72](#).
- Petre Stoica, Randolph L Moses, et al. Spectral analysis of signals. 2005b. Cited page [94](#).
- Atticus EL Stovall and Herman H Shugart. Improved biomass calibration and validation with terrestrial lidar: implications for future lidar and sar missions. *IEEE Journal of Selected Topics in Applied Earth Observations and Remote Sensing*, 11(10):3527–3537, 2018. Cited page [110](#).
- S Stramondo, M Saroli, C Tolomei, M Moro, F Doumaz, A Pesci, F Loddo, P Baldi, and E Boschi. Surface movements in bologna (po plain—italy) detected by multitemporal dinsar. *Remote Sensing of Environment*, 110(3):304–316, 2007. Cited page [116](#).
- S Stramondo, F Bozzano, F Marra, U Wegmuller, FR Cinti, M Moro, and M Saroli. Subsidence induced by urbanisation in the city of rome detected by advanced insar technique and geotechnical investigations. *Remote Sensing of Environment*, 112(6):3160–3172, 2008. Cited page [116](#).

- Junichi Takaku, Takeo Tadono, Ken Tsutsui, and Mayumi Ichikawa. Validation of "aw3d" global dsm generated fromalos prism. *ISPRS Annals of the Photogrammetry, Remote Sensing and Spatial Information Sciences*, 3:25, 2016. Cited page [130](#).
- S Tebaldini. Algebraic synthesis of forest scenarios from multibaseline polinsar data. *IEEE Transactions on Geoscience and Remote Sensing*, 47(12):4132–4142, 2009a. Cited pages [69](#) and [70](#).
- S. Tebaldini and F. Rocca. Multibaseline polarimetric sar tomography of a boreal forest at p-and l-bands. *IEEE Transactions on Geoscience and Remote Sensing*, 50.1:232–246., 2012a. Cited page [82](#).
- Stefano Tebaldini. Algebraic synthesis of forest scenarios from multibaseline polinsar data. *IEEE Transactions on Geoscience and Remote Sensing*, 47(12):4132–4142, 2009b. Cited pages [52](#), [54](#), [55](#), [56](#), and [87](#).
- Stefano Tebaldini and Andrea Monti Guarnieri. On the role of phase stability in sar multi-baseline applications. *IEEE Transactions on Geoscience and Remote Sensing*, 48(7):2953–2966, 2010. Cited pages [51](#) and [52](#).
- Stefano Tebaldini and Fabio Rocca. On the impact of propagation disturbances on sar tomography: Analysis and compensation. In *Radar Conference, 2009 IEEE*, pages 1–6. IEEE, 2009. Cited pages [52](#), [55](#), and [69](#).
- Stefano Tebaldini and Fabio Rocca. Multibaseline polarimetric sar tomography of a boreal forest at p-and l-bands. *IEEE Transactions on Geoscience and Remote Sensing*, 50(1):232–246, 2012b. Cited pages [55](#), [56](#), [69](#), [70](#), and [86](#).
- Stefano Tebaldini, Fabio Rocca, Mauro Mariotti d’Alessandro, and Laurent Ferro-Famil. Phase calibration of airborne tomographic sar data via phase center double localization. *IEEE Transactions on Geoscience and Remote Sensing*, 54(3):1775–1792, 2015. Cited pages [93](#), [94](#), and [95](#).
- Stefano Tebaldini, Fabio Rocca, Mauro Mariotti d’Alessandro, and Laurent Ferro-Famil. Phase calibration of airborne tomographic sar data via phase center double localization.

- IEEE Transactions on Geoscience and Remote Sensing*, 54(3):1775–1792, 2016. Cited pages [24](#), [38](#), [51](#), [52](#), [58](#), [68](#), and [71](#).
- Marivi Tello, Victor Cazcarra-Bes, Matteo Pardini, and Kostas Papathanassiou. Structural classification of forest by means of l-band tomographic sar. In *2015 IEEE International Geoscience and Remote Sensing Symposium (IGARSS)*, pages 5288–5291. IEEE, 2015. Cited page [96](#).
- Marivi Tello, Victor Cazcarra-Bes, Matteo Pardini, and Konstantinos Papathanassiou. Forest structure characterization from sar tomography at l-band. *IEEE Journal of Selected Topics in Applied Earth Observations and Remote Sensing*, (99):1–13, 2018. Cited pages [86](#) and [110](#).
- Roberto Tomás, G Herrera, Jose Delgado, Juan M Lopez-Sanchez, JJ Mallorquí, and J Mulas. A ground subsidence study based on dinsar data: Calibration of soil parameters and subsidence prediction in murcia city (spain). *Engineering geology*, 111(1-4):19–30, 2010. Cited page [116](#).
- Robert N Treuhaft and Paul R Siqueira. Vertical structure of vegetated land surfaces from interferometric and polarimetric radar. *Radio Science*, 35(1):141–177, 2000. Cited pages [21](#), [35](#), and [86](#).
- NE Tsendbazar, M Herold, S De Bruin, M Lesiv, S Fritz, R Van De Kerchove, M Buchhorn, M Duerauer, Z Szantoi, and J-F Pekel. Developing and applying a multi-purpose land cover validation dataset for africa. *Remote Sensing of Environment*, 219:298–309, 2018. Cited pages [1](#) and [64](#).
- Woody Turner, Sacha Spector, Ned Gardiner, Matthew Fladeland, Eleanor Sterling, and Marc Steininger. Remote sensing for biodiversity science and conservation. *Trends in ecology & evolution*, 18(6):306–314, 2003. Cited page [86](#).
- Freek J Van Leijen and Ramon F Hanssen. Persistent scatterer density improvement using adaptive deformation models. In *2007 IEEE International Geoscience and Remote Sensing Symposium*, pages 2102–2105. IEEE, 2007. Cited page [49](#).

- Valentine Wasik, Pascale C Dubois-Fernandez, Cédric Taillandier, and Sassan S Saatchi. The afrisar campaign: Tomographic analysis with phase-screen correction for p-band acquisitions. *IEEE Journal of Selected Topics in Applied Earth Observations and Remote Sensing*, 2018. Cited page [81](#).
- Martin Wermuth, A Hauschild, O Montenbruck, and A Jäggi. Terrasar-x rapid and precise orbit determination. In *21st International Symposium on Space Flight Dynamics*, volume 28. Citeseer, 2009. Cited pages [30](#), [133](#), and [141](#).
- Charles Werner, U Wegmuller, Tazio Strozzi, and Andreas Wiesmann. Interferometric point target analysis for deformation mapping. In *IGARSS 2003. 2003 IEEE International Geoscience and Remote Sensing Symposium. Proceedings (IEEE Cat. No. 03CH37477)*, volume 7, pages 4362–4364. IEEE, 2003. Cited page [49](#).
- Lee JT White. Forest-savanna dynamics and the origins of marantaceae forest in central gabon. *African rain forest ecology and conservation: An interdisciplinary perspective*, pages 165–182, 2001. Cited page [65](#).
- S Joseph Wright. Tropical forests in a changing environment. *Trends in ecology & evolution*, 20(10):553–560, 2005. Cited page [85](#).
- Chen Yu, Nigel T Penna, and Zhenhong Li. Generation of real-time mode high-resolution water vapor fields from gps observations. *Journal of Geophysical Research: Atmospheres*, 122(3):2008–2025, 2017. Cited pages [123](#) and [131](#).
- Chen Yu, Zhenhong Li, and Nigel T Penna. Interferometric synthetic aperture radar atmospheric correction using a gps-based iterative tropospheric decomposition model. *Remote Sensing of Environment*, 204:109–121, 2018a. Cited pages [123](#) and [131](#).
- Chen Yu, Zhenhong Li, Nigel T Penna, and Paola Crippa. Generic atmospheric correction model for interferometric synthetic aperture radar observations. *Journal of Geophysical Research: Solid Earth*, 123(10):9202–9222, 2018b. Cited pages [123](#) and [131](#).

- Howard A Zebker and Richard M Goldstein. Topographic mapping from interferometric synthetic aperture radar observations. *Journal of Geophysical Research: Solid Earth*, 91(B5):4993–4999, 1986. Cited pages [21](#) and [35](#).
- Howard A Zebker and Jakob J Van Zyl. Imaging radar polarimetry: A review. *Proceedings of the IEEE*, 79(11):1583–1606, 1991. Cited page [62](#).
- Howard A Zebker, Paul A Rosen, and Scott Hensley. Atmospheric effects in interferometric synthetic aperture radar surface deformation and topographic maps. *Journal of geophysical research: solid earth*, 102(B4):7547–7563, 1997. Cited pages [49](#) and [120](#).
- Alan D Ziegler, Lim Han She, Chatchai Tantasarin, Nick R Jachowski, and Robert Wasson. Floods, false hope, and the future. *Hydrological Processes*, 26(11):1748–1750, 2012. Cited page [115](#).

L-band UAVSAR tomographic imaging in dense forests: Gabon forests

Article

L-Band UAVSAR Tomographic Imaging in Dense Forests: Gabon Forests

Ibrahim El Moussawi ^{1,2,3,4,*}, Dinh Ho Tong Minh ¹, Nicolas Baghdadi ¹, Chadi Abdallah ²,
Jalal Jomaah ³, Olivier Strauss ⁴ and Marco Laval ⁵

¹ National Research Institute of Science and Technology for Environment and Agriculture (IRSTEA), University of Montpellier, Land Environment Remote Sensing and Spatial Information (TETIS), 34090 Montpellier, France; dinh.ho-tong-minh@irstea.fr (D.H.T.M.); nicolas.baghdadi@teledetection.fr (N.B.)

² National Center for Remote Sensing, National Council for Scientific Research (CNRS), Riad al Soloh, 1107 2260 Beirut, Lebanon; chadi@cnrs.edu.lb

³ Doctoral School of Sciences and Technologies, Lebanese University (LU), 1003 Beirut, Lebanon; jomaah@enserg.fr

⁴ Laboratory of Informatics, Robotics, and Microelectronics of Montpellier (LIRMM), University of Montpellier, 34392 Montpellier CEDEX 5, France; strauss@lirmm.fr

⁵ National Aeronautics and Space Administration (NASA), Jet Propulsion Laboratory (JPL), California Institute of Technology, Pasadena, CA 91109, USA; Marco.lavalle@jpl.nasa.gov

* Correspondence: ibrahim.el-moussawi@irstea.fr; Tel.: +33-467-548754

Received: 29 January 2019; Accepted: 20 February 2019; Published: 26 February 2019



Abstract: Developing and enhancing strategies to characterize actual forests structure is a timely challenge, particularly for tropical forests. P-band synthetic aperture radar (SAR) tomography (TomoSAR) has previously been demonstrated as a powerful tool for characterizing the 3-D vertical structure of tropical forests, and its capability and potential to retrieve tropical forest structure has been discussed and assessed. On the other hand, the abilities of L-band TomoSAR are still in the early stages of development. Here, we aim to provide a better understanding of L-band TomoSAR capabilities for retrieving the 3-D structure of tropical forests and estimating the top height in dense forests. We carried out tomographic analysis using L-band UAVSAR data from the AfriSAR campaign conducted over Gabon Lopé Park in February 2016. First, it was found that L-band TomoSAR was able to penetrate into and through the canopy down to the ground, and thus the canopy and ground layers were detected correctly. The resulting TomoSAR vertical profiles were validated with a digital terrain model and canopy height model extracted from small-footprint Lidar (SFL) data. Second, there was a strong correlation between the L-band Capon beam forming profile in HH and HV polarizations with Land Vegetation Ice Sensor (LVIS) Level 1B waveform Lidar over different kinds of forest in Gabon Lopé National Park. Finally, forest top height from the L-band data was estimated and validated with SFL data, resulting in a root mean square error of 3 m and coefficient of determination of 0.92. The results demonstrate that L-band TomoSAR is capable of characterizing 3-D structure of tropical forests.

Keywords: tomography SAR (TomoSAR); above-ground biomass (AGB); tropical forests; AfriSAR; UAVSAR; phase calibration

1. Introduction




Tropical forests have major impacts on Earth's ecosystem in terms of carbon storage, regulating water, and weather. Above-ground biomass (AGB) is the most important parameter related directly to the amount of carbon in the global ecosystem cycle [1]. Uncertainty in balancing the global carbon budget arises from a deficiency in AGB density estimation and carbon stocks in tropical forests. Indeed,

B

**Monitoring tropical forest structure
using SAR tomography at L- and
P-band**

Article

Monitoring Tropical Forest Structure Using SAR Tomography at L- and P-Band

Ibrahim El Moussawi ^{1,2,3,4}, Dinh Ho Tong Minh ¹ , Nicolas Baghdadi ¹ , Chadi Abdallah ^{2,*} , Jalal Jomaah ³, Olivier Strauss ⁴, Marco Lavallo ⁵ and Yen-Nhi Ngo ¹

¹ National Research Institute of Science and Technology for Environment and Agriculture (IRSTEA), University of Montpellier, Land Environment Remote Sensing and Spatial Information (TETIS), 34090 Montpellier, France

² National Center for Remote Sensing, National Council for Scientific Research (CNRS), Riad al Soloh, 1107 2260 Beirut, Lebanon

³ Doctoral School of Sciences and Technologies, Lebanese University (LU), 1003 Beirut, Lebanon

⁴ Laboratory of Informatics, Robotics, and Microelectronics of Montpellier (LIRMM), University of Montpellier, 34090 Montpellier, France

⁵ National Aeronautics and Space Administration (NASA), Jet Propulsion Laboratory (JPL), California Institute of Technology, Pasadena, CA 91125, USA

* Correspondence: chadi@cnrs.edu.lb; Tel.: +961-4-409-845

Received: 17 July 2019; Accepted: 16 August 2019; Published: 19 August 2019



Abstract: Our study aims to provide a comparison of the P- and L-band TomoSAR profiles, Land Vegetation and Ice Sensor (LVIS), and discrete return LiDAR to assess the ability for TomoSAR to monitor and estimate the tropical forest structure parameters for enhanced forest management and to support biomass missions. The comparison relies on the unique UAVSAR Jet propulsion Laboratory (JPL)/NASA L-band data, P-band data acquired by ONERA airborne system (SETHI), Small Footprint LiDAR (SFL), and NASA Land, Vegetation and Ice Sensor (LVIS) LiDAR datasets acquired in 2015 and 2016 in the frame of the AfriSAR campaign. Prior to multi-baseline data processing, a phase residual correction methodology based on phase calibration via phase center double localization has been implemented to improve the phase measurements and compensate for the phase perturbations, and disturbances originated from uncertainties in allocating flight trajectories. First, the vertical structure was estimated from L- and P-band corrected Tomography SAR data measurements, then compared with the canopy height model from SFL data. After that, the SAR and LiDAR three-dimensional (3D) datasets are compared and discussed at a qualitative basis at the region of interest. The L- and P-band's performance for canopy penetration was assessed to determine the underlying ground locations. Additionally, the 3D records for each configuration were compared with their ability to derive forest vertical structure. Finally, the vertical structure extracted from the 3D radar reflectivity from L- and P-band are compared with SFL data, resulting in a root mean square error of 3.02 m and 3.68 m, where the coefficient of determination shows a value of 0.95 and 0.93 for P- and L-band, respectively. The results demonstrate that TomoSAR holds promise for a scientific basis in forest management activities.

Keywords: tomography SAR; AfriSAR; TropiSAR; LiDAR LVIS

1. Introduction

Tropical Forests play a vital role in the global carbon cycle, and subsequently within the global climate [1]. Tropical forests are incredibly complicated, diverse, and frequently threatened. Indeed, there's a crucial demand to develop a new technology to help in surveying and revealing the dynamics of tropical forests. The dynamic processes like growth, regeneration, decay, and disturbance, strongly

C

**Comparison of multi temporal radar
interferometry techniques using
Sentinel-1: Lebanon case study**

Comparison of multi temporal radar interferometry techniques using Sentinel-1: Lebanon case study

Ibrahim El Moussawi ^{1,2,3,4*}, Dinh Ho Tong Minh ¹, Nicolas Baghdadi ¹, Chadi Abdallah ², Jalal Jomaah ³, Olivier Strauss ⁴, and Yen-Nhi Ngo ¹

¹ National Research Institute of Science and Technology for Environment and Agriculture (IRSTEA), University of Montpellier, Land Environment Remote Sensing and Spatial Information (TETIS), 34090 Montpellier, France; dinh.ho-tong-minh@irstea.fr (D.H.T.M.); nicolas.baghdadi@teledetection.fr (N.B.); yen-nhi.ngo@irstea.fr (Y.N)

² National Center for Remote Sensing, National Council for Scientific Research (CNRS), Riad al Soloh, 1107 2260 Beirut, Lebanon; chadi@cnrs.edu.lb (C.A.)

³ Doctoral School of Sciences and Technologies, Lebanese University (LU), 1003 Beirut, Lebanon; jomaah@enserg.fr (J.J.)

⁴ Laboratory of Informatics, Robotics, and Microelectronics of Montpellier (LIRMM), University of Montpellier, 34090 Montpellier, France; strauss@lirmm.fr (O.S.)

* Correspondence: ibrahim.el-moussawi@irstea.fr; Tel.: +33 467 54 87 54

Version October 8, 2019 submitted to Remote Sens.

Abstract: Multi-temporal Synthetic Aperture Radar (SAR) Interferometry (InSAR) is a widely used technique to measure ground subsidence and has already shown its ability to map such phenomena on a large spatial scale with millimetric accuracy from space. The aim of this paper is to provide a better understanding of the capabilities of C-band for estimating ground subsidence in Lebanon. Analysis is carried out on Sentinel-1 stack C-band from 2015 to 2019 acquired over Lebanon. The study demonstrates that the InSAR technique can be effective at detecting and estimating subsidence phenomena. The study provides strong support for the scientific potential of C-band SAR space-borne mission in Lebanon because it demonstrates the feasibility of ground subsidence estimates by C-band SAR.

Keywords: DInSAR; PSI; PS/DS; Sentinel-1; Stamps; Deformation velocity

1. Introduction

Land subsidence is a major hydro-geological hazard that affects our society [1–3]. Differential Interferometric Synthetic Aperture Radar (DInSAR) is a powerful technique used to monitor and measure Earth's surface deformations using SAR data. DInSAR exploits the phase information of at least two temporally separated SAR acquisitions acquired over the same area to form interferogram and measure the displacements and deformations occurred in the Earth's surface.



An advanced approach of DInSAR is the Permanent Scatterer Interferometry (PSI) technique [4–7], such that the interferometry analysis is done on Permanent scatterers (PS's) targets (like man-made structures, rocks, and other reflectors...), that have temporally stable phase and amplitude. PSI for the processing of multi-temporal SAR acquisitions is widely used to measure urban ground subsidence and has already shown its ability to map such phenomena on a large spatial scale with millimeters accuracy from space, associated with either ground subsidence [8–13], railway subsidence [14], or landslides [15], etc. The first PSI technique is proposed by [4,6]. Several contributions had followed PSI approach. The Small Baseline Subset technique (SBAS) [16] is a major approach that extensively used in land surface monitoring using

D

**Estimation of Rice Height and
Biomass Using Multitemporal SAR
Sentinel-1 for Camargue, Southern
France.**

Article

Estimation of Rice Height and Biomass Using Multitemporal SAR Sentinel-1 for Camargue, Southern France

Emile Ndikumana ¹, Dinh Ho Tong Minh ^{1,*}, Hai Thu Dang Nguyen ^{1,2}, Nicolas Baghdadi ¹, Dominique Courault ³, Laure Hossard ⁴ and Ibrahim El Moussawi ¹

¹ UMR TETIS, IRSTEA, University of Montpellier, 34093 Montpellier, France; emile.ndikumana@irstea.fr (E.N.); dangnguyenhaithu@gmail.com (H.T.D.N.); nicolas.baghdadi@irstea.fr (N.B.); ibrahim.el-moussawi@irstea.fr (I.E.M.)

² Department of Space and Aeronautics, University of Science and technology of Hanoi, Vietnam Academy of Science and Technology, 122100 Hanoi, Vietnam

³ UMR 1114 EMMAH, INRA, University of Avignon, 84914 Avignon, France; dominique.courault@inra.fr

⁴ UMR 0951 INNOVATION, INRA, University of Montpellier, 34060 Montpellier, France; laure.hossard@inra.fr

* Correspondence: dinh.ho-tong-minh@irstea.fr

Received: 12 July 2018; Accepted: 29 August 2018; Published: 1 September 2018





Abstract: The research and improvement of methods to be used for crop monitoring are currently major challenges, especially for radar images due to their speckle noise nature. The European Space Agency's (ESA) Sentinel-1 constellation provides synthetic aperture radar (SAR) images coverage with a 6-day revisit period at a high spatial resolution of pixel spacing of 20 m. Sentinel-1 data are considerably useful, as they provide valuable information of the vegetation cover. The objective of this work is to study the capabilities of multitemporal radar images for rice height and dry biomass retrievals using Sentinel-1 data. To do this, we train Sentinel-1 data against ground measurements with classical machine learning techniques (Multiple Linear Regression (MLR), Support Vector Regression (SVR) and Random Forest (RF)) to estimate rice height and dry biomass. The study is carried out on a multitemporal Sentinel-1 dataset acquired from May 2017 to September 2017 over the Camargue region, southern France. The ground in-situ measurements were made in the same period to collect rice height and dry biomass over 11 rice fields. The images were processed in order to produce a radar stack in C-band including dual-polarization VV (Vertical receive and Vertical transmit) and VH (Vertical receive and Horizontal transmit) data. We found that non-parametric methods (SVR and RF) had a better performance over the parametric MLR method for rice biophysical parameter retrievals. The accuracy of rice height estimation showed that rice height retrieval was strongly correlated to the in-situ rice height from dual-polarization, in which Random Forest yielded the best performance with correlation coefficient $R^2 = 0.92$ and the root mean square error (RMSE) 16% (7.9 cm). In addition, we demonstrated that the correlation of Sentinel-1 signal to the biomass was also very high in VH polarization with $R^2 = 0.9$ and RMSE = 18% (162 g·m⁻²) (with Random Forest method). Such results indicate that the highly qualified Sentinel-1 radar data could be well exploited for rice biomass and height retrieval and they could be used for operational tasks.

Keywords: rice dry biomass; rice height; Multiple Linear Regression; Support Vector Regression; Random Forest; Sentinel-1, TomoSAR platform; Camargue; southern France

E

**Measuring Ground Subsidence in Ha
Noi Through the Radar
Interferometry Technique Using
TerraSAR-X and Cosmos SkyMed
Data**

Measuring Ground Subsidence in Ha Noi Through the Radar Interferometry Technique Using TerraSAR-X and Cosmos SkyMed Data

Dinh Ho Tong Minh , Quoc Cuong Tran, Quy Nhan Pham, Tran Trung Dang, Duc Anh Nguyen, Ibrahim El-Moussawi , and Thuy Le Toan

Abstract—Multitemporal synthetic aperture radar (SAR) interferometry (InSAR) is a widely used technique to measure the ground subsidence and has already shown its ability to map such phenomena on a large spatial scale with millimetric accuracy from space. In Vietnam, to have independent SAR data for surface risk applications, a new X-band SAR mission (JV-LOTUSat) has been scheduled for launch for the 2019–2020 timeframe. However, Vietnam is located in tropical regions where their conditions are impacted by strong atmosphere. The aim of this article is to provide a better understanding of the capabilities of the X-band for estimating the ground subsidence under tropical atmospheric conditions. Analysis is carried out on two stacks, TerraSAR-X and Cosmos SkyMed X-band, from 2011 to 2014 in Ha Noi. We show that the results on the ground subsidence from InSAR processing can describe consistently the subsidence area based on ground measurements. This article demonstrates that the InSAR technique can be effective at detecting and estimating the subsidence phenomena even with the X-band and under conditions typical of tropical regions. The displacement results from TerraSAR-X and Cosmos SkyMed datasets are consistent, with a correlation coefficient (R^2) of 0.91 for the period during which their coverage overlaps. Groundwater overexploitation is one of the main causes of the ground subsidence in Ha Noi. This study provides strong support for the scientific potential of the X-band SAR space-borne mission in Vietnam and other tropical countries because it demonstrates the feasibility of the ground subsidence estimates by the X-band SAR, even in conditions impacted by strong atmosphere.

Index Terms—Atmospheric phase screen (APS), ground subsidence, groundwater, Ha Noi, JV-LOTUSat, multitemporal synthetic aperture radar interferometry (InSAR), permanent scatterers/distributed scatterers (PS/DS) processing, synthetic aperture radar (SAR), tropical region, X-band.

I. INTRODUCTION

URBAN subsidence is a major hazard affecting our society [1]–[3]. In Vietnam, risk of subsidence has become increasingly frequent, particularly, in Ha Noi and Ho Chi Minh City. Planning responses to ground subsidence requires knowledge about its spatial extent and how it has changed over time [4]. Multitemporal synthetic aperture radar (SAR) interferometry (InSAR) is a widely used technique to measure the urban ground subsidence and has already shown its ability to map such phenomena on a large spatial scale with millimetric accuracy from space, associated with either ground subsidence (e.g., [5]–[7]), railway subsidence (e.g., [8]), landslides (e.g., [9]), etc. However, Vietnam is outside the Copernicus data policy of the European Space Agency (ESA), which is dedicated to support studies in the European zone. Only very few ESA data, e.g., C-band ENVISAT ASAR, exist that are suitable for such applications, which typically require a stack of multitemporal SAR data [10]. This is the reason why many works [4], [11], [12] are based on L-band (~ 23.6 cm) data of the Japan Aerospace Exploration Agency ALOS PalSAR satellite. Recently, C-band Sentinel-1 systematically acquires data at the global scale in the terrain observation with progressive scan (TOPS) mode [13]. However, TOPS Sentinel-1A/1B phase is very sensitive to geometric errors [14]. In this context, a new X-band SAR mission (JV-LOTUSat) has been scheduled for launch by Vietnam for the 2019–2020 time frame. The new JV-LOTUSat satellite is a collaborative effort between the governments of Vietnam and Japan [15].

X-band SAR data are sensitive to small variations (e.g., [16]–[18]). High-quality data are gathered by the German Space Agency TerraSAR-X (TSX) satellite constellation and by the Italian constellation of small satellites for the Mediterranean basin Observation Cosmos SkyMed (CSK). Thanks to the high resolution (less than 3 m with TSX and CSK) and the short wavelength (~ 3.1 cm) of the X-band, it is possible to study the signal of single objects such as buildings and bridges [19].

Manuscript received April 25, 2018; revised November 14, 2018 and July 23, 2019; accepted August 12, 2019. This work was supported in part by the Vietnam National Science Project DTDL.2012-T/28; in part by the European Space Agency (ESA), the Centre National d' Etudes Spatiales/Terre, Ocean, Surfaces Continentales, Atmosphere (CNES/TOSCA); and in part by UMR TETIS, Institut national de Recherche en Sciences et Technologies pour l'Environnement et l'Agriculture (IRSTEA). (Corresponding author: Dinh Ho Tong Minh.)

D. Ho Tong Minh and I. El-Moussawi are with UMR TETIS, Institut national de Recherche en Sciences et Technologies pour l'Environnement et l'Agriculture (IRSTEA), University of Montpellier, 34000 Montpellier, France (e-mail: dinh.ho-tong-minh@irstea.fr; ibrahim.el-moussawi@irstea.fr).

Q. C. Tran and D. A. Nguyen are with the Institute of Geological Sciences, Vietnam Academy of Science and Technology, 100000 Ha Noi, Vietnam (e-mail: tqcuong@igs.vn; nguyenducanh237@gmail.com).

Q. N. Pham is with the Hanoi University of Natural Resources & Environment, 100000 Ha Noi, Vietnam (e-mail: pqnhan@hunre.edu.vn).

T. T. Dang is with the National Center for Water Resources Planning and Investigation, 100000 Ha Noi, Vietnam (e-mail: dtrung@gmail.com).

T. Le Toan is with the Centre d' Etudes Spatiales de la Biosphere (CESBIO), 31400 Toulouse, France (e-mail: Thuy.LeToan@cesbio.cnrs.fr).

Color versions of one or more of the figures in this article are available online at <http://ieeexplore.ieee.org>.

Digital Object Identifier 10.1109/JSTARS.2019.2937398